FABRICATION AND CHARACTERISATION OF Pt-Co ELECTROCATALYSTS FOR OXYGEN REDUCTION REACTION IN POLYMER ELECTROLYTE MEMBRANE FUEL CELLS

by

PALLAVI PHARKYA
B.E., Malaviya National Institute of Technology, Jaipur, India, 2002

A THESIS SUBMITTED IN PARTIAL FULFILLMENT OF THE REQUIREMENTS FOR THE DEGREE OF MASTER OF APPLIED SCIENCE

in

THE FACULTY OF GRADUATE STUDIES

(DEPARTMENT OF MATERIALS ENGINEERING)

We accept this thesis as conforming to the required standard

The University of British Columbia
July 2004

Library Authorization

In presenting this thesis in partial fulfillment of the requirements for an advanced degree at the University of British Columbia, I agree that the Library shall make it freely available for reference and study. I further agree that permission for extensive copying of this thesis for scholarly purposes may be granted by the head of my department or by his or her representatives. It is understood that copying or publication of this thesis for financial gain shall not be allowed without my written permission.

PALLAVI PHARKYA
Name of Author *(please print)*

22/07/2004
Date (dd/mm/yyyy)

Title of Thesis: Fabrication and characterization of Pt-Co electrocatalysts for oxygen reduction reaction in polymer electrolyte membrane fuel cells.

Degree: Master of Applied Science Year: 2004

Department of Materials Engineering
The University of British Columbia
Vancouver, BC Canada

Abstract

Electrocatalysts have tremendous impact on the performance of fuel cells as both cathodic and anodic reactions take place on the surfaces of the electrocatalysts. This work focuses on fabrication and characterization of novel Pt-Co electrocatalysts for oxygen reduction reaction in polymer electrolyte membrane fuel cells.

High-energy ball milling was used for the fabrication of electrocatalysts. Alloy systems with varied ball to powder ratio, milling time and amount of process control agent were fabricated to optimize ball-milling conditions. Process control agents used were carbon and stearic acid. Ball to powder ratios of 39:1 or 78:1 were used and milling time was varied from 10 minutes to 90 hours. The optimized ball-milling conditions were then used to fabricate PtCo and PtCo/C alloy electrocatalysts. The low surface area of the ball-milled catalysts was further improved by lixiviation process.

Microstructural characterization techniques, TEM and SEM, were used for the particle size determination and particle morphology, EDS was used to determine the bulk elemental composition of the electrocatalysts, XPS was performed to determine the oxidation state, surface elemental analysis and presence of oxidized species of the electrocatalysts. Electrochemical methods, namely, cyclic and potentiodynamic polarization were performed to obtain kinetic parameters, such as, exchange current density and Tafel slopes. These electrochemical kinetic parameters determine electrocatalytic activity of the catalysts. Performances of the fabricated electrocatalysts in this work were compared with commercial electrocatalysts from E-TEK.

Table of Contents

Abstract.....ii
Table of Contents.....iii
List of Figures.....v
List of Tables.....x
List of Equations.....xi
Symbols and Abbreviations.....xiii
Acknowledgements.....xv

Chapter 1-INTRODUCTION 1

Chapter 2-LITERATURE REVIEW 4
2.1 Polymer electrolyte membrane fuel cells 6
2.2 Principles of operation of polymer electrolyte membrane fuel cells 6
2.3 Electrocatalysis in polymer electrolyte membrane fuel cells 11
2.3.1 Mechanism of oxygen reduction reaction 12
2.4 Parameters affecting electrocatalysts performance 13
2.5 The electrocatalysts materials used to date 16
2.6 Method of fabrication 31
2.6.1 Nanocrystalline materials 31
2.6.2 Methods of preparation of nanostructured materials 31
2.6.3 Mechanical alloying – Mechanism 32
2.6.4 Planetary monomill 36
2.7 Working electrode used for electrochemical experiments 39
2.7.1 Glassy carbon electrodes 40
2.7.2 Method of manufacture and lab procedure for the usage of GCE 40

Chapter 3-EXPERIMENTAL DETAILS 42
3.1 Electrocatalysts materials 42
3.1.1 Materials used for electrocatalyst preparation 42
3.1.2 Commercial electrocatalysts 42
3.2 Fabrication technique 43
3.2.1 Set up of ball milling 43
3.2.2 Optimization of ball milling parameters 44
3.2.3 Optimization of temperature and pressure 45
3.2.4 Alloy systems prepared 47
3.3 Fabrication process for the electrocatalysts 48
3.3.1 Electrocatalysts prepared 48
3.3.2 Lixiviation process 49
3.4 Microstructural characterization 49
3.4.1 Scanning electron microscopy 49
3.4.2 Transmission electron microscopy 50
3.4.3 X-ray diffractometry 50
3.4.4 X-ray photoelectron spectroscopy 51
3.4.5 Surface area measurements by BET analysis 52

3.5 Electrochemical characterization 52
3.5.1 Apparatus 52
3.5.2 Electrode preparation 54
3.5.3 Electrolyte and temperature range used 55
3.5.4 Cyclic polarization 56
3.5.5 Potentiodynamic polarization 56

Chapter 4 - RESULTS AND DISCUSSION 59
4.1 Characterization of as-received materials 59
4.2 Optimization of ball milling parameters 61
4.2.1 Co, Co/SA, Co/C alloy systems 61
4.2.1.1 Particle size analysis 61
4.2.1.2 Phase identification and solid state reactions 65
4.2.1.3 Crystallite size and lattice parameter analysis 68
4.2.1.4 Microstrain analysis 69
4.2.2 Pt, Pt/C alloy systems 70
4.2.2.1 Particle size analysis 70
4.2.2.2 Phase identification and solid state reactions 71
4.2.2.3 Crystallite size and lattice parameters analysis 74
4.2.2.4 Microstrain analysis 75
4.2.3 Summary 75
4.3 PtCo and PtCo/C alloy electrocatalysts 76
4.3.1 Elemental composition analysis 76
4.3.2 Particle size analysis and particle dispersion 77
4.3.3 Phase identification and solid state reactions 80
4.3.4 Crystallite size and lattice parameter analysis 84
4.3.5 Surface oxide and surface elemental determination 86
4.3.6 Electrochemical behaviour of catalysts 93
Chapter 5- CONCLUSIONS AND RECOMMENDATIONS 110
Chapter 6- FUTURE WORK 115
REFERENCES 116
APPENDIX A 122
APPENDIX B 123

List of Figures

Figure 2.1 Schematic illustration of the cross-sectional area of polymer electrolyte membrane fuel cell 7

Figure 2.2 Reversible standard hydrogen potential for H_2/O_2 reactions as a function of temperature 9

Figure 2.3 Curve density-voltage curve of the low temperature H_2/O_2 fuel cells... 10

Figure 2.4 Relationship of platinum surface area to particle size based on the spherical geometry 14

Figure 2.5 Correlation of oxygen electrode performance of Pt and Pt alloy electrocatalysts with Pt-Pt bond distance and the d-orbital vacancy of Pt 15

Figure 2.6 Illustration showing uniformly distributed Pt particles on carbon support 19

Figure 2.7 Base voltammograms of the standard supported Pt catalysts compared to the supported Pt_3Co and PtCo catalyst in 0.1M $HClO_4$ (Ar saturated) at room temperature 22

Figure 2.8 Comparison of polarization data of CoTPP, Pt-Co and Pt electrocatalyst 23

Figure 2.9 Plot of potential vs. time of the CoTPP & Pt-Co alloy electrocatalyst 23

Figure 2.10 Cyclic voltammograms of (a) 20 wt% Pt on carbon black (E-TEK), (b) $Pt_{0.50}Ru_{0.50}$ ball milled alloy, (c) 20 wt% ball milled $Pt_{0.50}Ru_{0.50}$ milled a second time with XC-72R 25

Figure 2.11 Fuel cell polarization curves of (a) 20 wt% ball milled $Pt_{0.50}Ru_{0.50}$ alloy milled a second time with XC-72R, (b) 20 wt% Pt/XC-72R commercial catalyst (E-TEK) 25

Figure 2.12 Schematic showing ball motion inside the ball mill 32

Figure 2.13 Graph showing refinement of particle and grain sizes with milling 35

Figure 2.14 Pt-Co binary phase diagram 37

Figure 3.1 Planetary monomill "Pulversiette 6" for Fritsch 44

Figure 3.2 Temperature-pressure profile obtained from GTM (II) system 45

Figure 3.3 273A potentiostat from Princeton applied research laboratory attached with personal computer 53

Figure 3.4 Schematic representation of 273A potentiostat 53

Figure 3.5 Rotating disc electrode apparatus 54

Figure 3.6 A RDE0008 Glassy carbon electrode (Φ = 4mm) 55

Figure 4.1 SEM micrograph of Co-AR 59

Figure 4.2 SEM micrograph of Pt-AR 59

Figure 4.3 XRD diffractogram of Co-AR 60

Figure 4.4 XRD diffractogram of Pt-AR 60

Figure 4.5 SEM micrograph of Cobalt-AR 61

Figure 4.6 SEM micrograph of Co-10h-78 61

Figure 4.7 SEM micrograph of Co-40h-78 61

Figure 4.8 SEM micrograph of Co-40h-39 61

Figure 4.9 SEM micrograph of Co-10h-78-2%SA 62

Figure 4.10 SEM micrograph of Co-40h-78-2%SA 62

Figure 4.11 SEM micrograph of Co-90h-78-2%SA 62

Figure 4.12 SEM micrograph of Co-40h-78-20%SA 62

Figure 4.13 TEM micrograph of Co-90h-78-20%SA 62

Figure 4.14 SEM micrograph of Co-10h-78-20%C 62

Figure 4.15 TEM micrograph of Co-40h-78-20%C 63

Figure 4.16 TEM micrograph of Co-90h-78-20%C 63

Figure 4.17 TEM plot of particle size vs. milling time of Co-SA, Co-C systems 64

Figure 4.18 Diffraction pattern of Co-90h-20%SA-78 65

Figure 4.19 Diffraction pattern of Co-90h-20%C-78 65

Figure 4.20 Diffraction pattern of Co-90h-20%C-78 65

Figure 4.21 XRD diffractograms of Co-AR, Co-40h, Co-40h-78-20%SA, Co-40h-78-20%C 66

Figure 4.22 Plot showing microstrain vs. milling time obtained from XRD for Co alloy systems 69

Figure 4.23 SEM micrograph of Pt-AR 70

Figure 4.24 SEM micrograph of Pt-30min 70

Figure 4.25 TEM micrograph of Pt-40h 70

Figure 4.26 TEM micrograph of Pt-40h-20%C 70

Figure 4.27 Diffraction pattern of Pt-40h 71

Figure 4.28 Diffraction pattern of Pt-40h-20%C 71

Figure 4.29 XRD diffractograms of Pt-AR, Pt-30min-78, Pt-40h-78 72

Figure 4.30 XRD diffractograms of Pt-AR, Pt-30min-78-20%C, Pt-40h-78-20%C 73

Figure 4.31 XRD diffractograms of Pt-AR, Pt-40h-78, Pt-40h-78-20%C 73

Figure 4.32 TEM microgram of 40%PtCo-ETEK 78

Figure 4.33 TEM micrograms of 10%PtCo-ETEK 78

Figure 4.34 TEM micrograph of lixiviated catalyst 78

Figure 4.35 TEM micrograph of PtCo-45-1%C-5h 78

Figure 4.36 TEM micrograph of $Pt_{0.25}Co_{0.75}$-40h 78

Figure 4.37 TEM micrograph of $Pt_{0.25}Co_{0.75}$-40h-20%C-30min 78

Figure 4.38 Diffraction pattern of $Pt_{0.25}Co_{0.75}$-40h-20%C-30min 79

Figure 4.39 Diffraction pattern of 10%PtCo-ETEK 79

Figure 4.40 Diffraction pattern of 40%PtCo-ETEK 80

Figure 4.41 Diffraction pattern of lixiviated catalyst 80

Figure 4.42 XRD diffractograms of PtCo-40h, PtCo-40h-20%C-5min, PtCo-40h-20%C-30min 81

Figure 4.43 XRD diffractograms of PtCo-45h-1%C-5h, lixiviated catalyst, 10%PtCo-ETEK, 40%PtCo-ETEK 82

Figure 4.44 Broad scan of Pt-AR obtained by XPS analysis 86

Figure 4.45 Broad scan of 40%PtCo-ETEK obtained by XPS analysis 87

Figure 4.46 Broad scan of lixiviated catalyst obtained by XPS analysis 87

Figure 4.47 Broad scan of $Pt_{0.25}Co_{0.75}$-40h obtained from XPS analysis 88

Figure 4.48 Broad scan of PtCo-45-1%C-5h obtained by XPS analysis 88

Figure 4.49(a) Narrow scans of Pt 4f peaks obtained by XPS analysis 90

Figure 4.49(b) Narrow scans of Pt 4f peaks obtained by XPS analysis 91

Figure 4.50 Narrow scans of Co 2p peaks obtained by XPS analysis 91

Figure 4.51(a) Potentiodynamic scans of Pt-AR, 40%PtCo-ETEK, 10%PtCo-ETEK, lixiviated catalyst in 0.5MH_2SO_4 at 22°C 93

Figure 4.51(b) Potentiodynamic scans of $Pt_{0.25}Co_{0.75}$-40h,$Pt_{0.25}Co_{0.75}$-40h-20%C-30min, PtCo-45-1%C-5h in 0.5MH_2SO_4 at 22°C 94

Figure 4.52(a) Potentiodynamic scans of Pt-AR, 40%PtCo-ETEK, 10%PtCo-ETEK, lixiviated catalyst in 0.25M NaOH at 22°C 96

Figure 4.52(b) Potentiodynamic scans of $Pt_{0.25}Co_{0.75}$-40h, $Pt_{0.25}Co_{0.75}$-40h-20%C-30min, PtCo-45-1%C-5h in 0.25M NaOH at 22°C 97

Figure 4.53(a) Potentiodynamic test of Pt-AR, 40%PtCo-ETEK, 10%PtCo-ETEK, lixiviated catalyst in 0.5MH_2SO_4 at 50°C 98

Figure 4.53(b) Potentiodynamic scans of $Pt_{0.25}Co_{0.75}$-40h, $Pt_{0.25}Co_{0.75}$-40h-20%C-30min, PtCo-45-1%C-5h in 0.5MH_2SO_4 at 50°C 99

Figure 4.54(a) Potentiodynamic tests of Pt-AR, 40%PtCo-ETEK, 10%PtCo-ETEK, lixiviated catalyst in 0.25M NaOH at 50°C 100

Figure 4.54(b) Potentiodynamic scans of $Pt_{0.25}Co_{0.75}$-40h, $Pt_{0.25}Co_{0.75}$-40h-20%C-30min, PtCo-45-1%C-5h in 0.25M NaOH at 50°C 101

Figure 4.55(a) Cyclic voltammograms of Pt-AR, 40%PtCo-ETEK, 10%PtCo-ETEK, lixiviated catalyst in 0.5M H_2SO_4 at 22°C 104

Figure 4.55(b) Cyclic voltammograms of $Pt_{0.25}Co_{0.75}$-40h,$Pt_{0.25}Co_{0.75}$-40h-20%C-30min, PtCo-45-1%C-5h in 0.5M H_2SO_4 at 22°C 104

Figure 4.56(a) Cyclic voltammograms of Pt-AR, 40%PtCo-ETEK, 10%PtCo-ETEK, lixiviated catalyst in 0.25M NaOH at 22°C 105

Figure 4.56(b) Cyclic voltammograms of $Pt_{0.25}Co_{0.75}$-40h,$Pt_{0.25}Co_{0.75}$-40h-20%C-30min, PtCo-45-1%C-5h in 0.25M NaOH at 22°C 105

Figure 4.57(a) Cyclic voltammograms of Pt-AR, 40%PtCo-ETEK, 10%PtCo-ETEK, Lixiviated catalyst in 0.5M H_2SO_4 at 50°C 106

Figure 4.57(b) Cyclic voltammograms of $Pt_{0.25}Co_{0.75}$-40h,$Pt_{0.25}Co_{0.75}$-40h-20%C-30min, PtCo-45-1%C-5h in 0.5M H_2SO_4 at 50°C 107

Figure 4.58(a) Cyclic voltammograms of Pt-AR, 40%PtCo-ETEK, 10%PtCo-ETEK, lixiviated catalyst in 0.25M NaOH at 50°C 107

Figure 4.58(b) Cyclic voltammograms of $Pt_{0.25}Co_{0.75}$-40h,$Pt_{0.25}Co_{0.75}$-40h-20%C-30min, PtCo-45-1%C-5h in 0.25M NaOH at 50°C 108

Figure 5.1 Flow diagram of Mircon-Master® jet pulverizer from the Jet Pulverizer company 113

Figure 6.1 Membrane electrode assembly of commercial PtCo/C electrocatalyst 115

Figure 6.2 Membrane electrode assembly of commercial PtCo/C electrocatalyst 115

List of Tables

Table 1.1 Types of fuel cells, their electrolytes, working temperature and applications 5

Table 2.1 Table summarizing kinetic parameters of oxygen reduction reaction on various electrocatalysts in alkaline medium 27

Table 2.2 Table summarizing kinetic parameters of oxygen reduction reaction on various electrocatalysts in acidic medium 29

Table 3.1 Ball milling conditions for catalyst powder 46

Table 3.2 Table summarizing details of potentiodynamic polarization tests 57

Table 3.3 Table summarizing details of cyclic polarization tests 58

Table 4.1 Table showing lattice parameter, d-spacing and crystallite size of Co alloy system obtained from XRD 68

Table 4.2 Table showing lattice parameter, d-spacing and crystallite size of Pt alloy system obtained from XRD 74

Table 4.3 Bulk elemental analysis of alloy electrocatalysts and commercial E-TEK catalysts by EDS 76

Table 4.4 Elemental composition of the filtrate obtained from lixiviated sample (#4) by IPL analysis 77

Table 4.5 Particle size of PtCo electrocatalysts by TEM 79

Table 4.6 The lattice parameter, d-spacing and crystallite size of PtCo electrocatalysts obtained by XRD 84

Table 4.7 Surface area analysis by crystallite size 85

Table 4.8 Elemental composition of various catalysts obtained from XPS analysis 89

Table 4.9 Surface and bulk atomic ratios of Pt:Co obtained by XPS and EDS analysis respectively 92

Table 4.10 The i_o values in acidic and alkaline medias at 25°C and 50°C 102

Table A.1 Table showing properties of Pt,Co,C 122

Table B.1 Table showing relative density, crystallite size and surface area of the catalysts 123

List of Equations

Equation 2.1 Overall fuel cell reaction 4

Equation 2.2 Anodic reaction of PEMFC 8

Equation 2.3 Cathodic reaction of PEMFC 8

Equation 2.4 Butler-Volmer equation 9

Equation 2.5 ORR by direct four electron pathway in alkaline medium 12

Equation 2.6 ORR by direct four electron pathway in acidic medium 12

Equation 2.7 ORR by peroxide pathway in alkaline medium 12

Equation 2.8 ORR by peroxide pathway in acidic medium 12

Equation 2.9 Decomposition of peroxide reaction 13

Equation 2.10 Desorption reaction of chemisorbed oxygen 13

Equation 2.11 Formula for the calculation of surface area by particle size 13

Equation 3.1 Scherer's equation for calculation of crystallite size 51

Equation 3.2 Formula to calculate integral breadth method 51

Equation 3.3 Peak broadening by Aqua and Wagner method 51

Equation 4.1 Reaction showing ball milling of Co for 40h without addition of PCA 66

Equation 4.2 Reaction showing ball milling of Co with stearic acid for 40hrs 67

Equation 4.3 Reaction showing ball milling of Co with carbon for 40hrs 67

Equation 4.4 Reaction showing ball milling of Pt for 40hrs 71

Equation 4.5 Reaction showing ball milling of Pt with carbon for 0.5hrs & 40hrs 72

Equation 4.6 Reaction showing ball milling of 25a/o% Pt and 75a/0%Co for 40hrs 80

Equation 4.7 Reaction showing ball milling of $Pt_{0.25}Co_{0.75}$-40h with 20%C for 5min, 30min 80

Equation 4.8 Reaction showing ball milling of Pt and Co for 40h 76

Equation 4.9 Reaction showing balling milling of PtCo with 1%C for 5h 76

Equation 4.10 Reaction showing lixiviation of PtCo-C electrocatalyst 76

Equation 4.11 ORR in acidic medium 93

Equation 4.12 ORR in alkaline medium 96

Equation B.1 Formula for calculating surface area of the catalysts by crystal size 123

Equation B.2 Formula for calculating relative density of alloy 123

List of symbols and Acronyms

λ – Wavelength of the x-ray source, cm^2

θ - Bragg's angle, radians

β (X-ray diffraction technique) – Integral breadth

B - Peak width at half maximum intensity

β (Electrochemical techniques) - Tafel slope, millivolt/decade

D – Crystallite size

ρ – Density, g/cm^3

Δ – Difference between final and initial values

η – Activation overpotential, millivolts

i_0 – Exchange current density, amp/cm^2

γ – Specific surface energy

ε – Crystalline strain

ν – Frequency

h – Planks constant, joules-sec

A_p - Total area under peak

H_p - Peak height

BE – Binding energy, eV

RDE – Rotating disc electrode

RRDE – Rotating ring disc electrode

GTM – Gas temperature measurement

SCE – Saturated calomel electrode

NHE – Normal hydrogen electrode

SEM – Scanning electrode microscopy

EDS – Electron diffraction spectroscopy

TEM – Transmission electron microscopy

XRD – X-ray diffractometry

XPS – X-ray photoelectron spectroscopy

AFC – Alkaline fuel cell

PAFC – Phosphoric acid fuel cell

MCFC – Molten carbonate fuel cell

SOFC – Solid oxide fuel cell

PEMFC – Polymer electrolyte membrane fuel cell

SPEFC – Solid polymer electrolyte membrane fuel cell

DMFC –Direct methanol fuel cell

MEA – Membrane electrode assembly

ORR – Oxygen reduction reaction

BPR – Ball to powder ratio

PCA – Process control agent

GCE – Glassy carbon electrode

FCC – Face centered cubic structure

HCP – Hexagonal cubic packed structure

MA – Mechanical alloying

AR – As- received

ss - Solid solution

wt % - Weight percent

at.% - Atomic percentage

Acknowledgements

I would like to express my sincere thanks to Dr. Akram Alfantazi for giving me the opportunity to work with him on this research program. I am grateful to him for his understanding, support and patience during sometimes trying integration in Canada. Special thanks to Dr. Zoheir Farhat, NRC, for his technical support and guidance.

I would like to acknowledge Fuel Cell Innovation Center, National Research Council (NRC-CNRC), Canada and Natural Science and Engineering Research council of Canada (NSERC) for their financial support.

I would like to thank Ms. Mary Mager for her assistance in using SEM and TEM. Many thanks to Edith Czech for her help in the initial fabrication of alloy systems and microstructural characterization. Warm thanks to Edouard Asselin and Alain Tshilombo for their supports and technical discussions. I would also like to thank Andy Jung for his thoughtful technical suggestions.

Lastly, I express my sincere gratitude to my mother and father, my siblings, Priti and Amit, brother-in-law, Girish; and my friend Nitin for their constant love and support. I would not have been able to complete my Master's without their constant encouragement and faith in me. They all were my inspiration to move on. Lastly, I would like to thank God for giving me everything I have today. I dedicate this work to my parents.

Chapter One

Introduction

The alarming depletion of conventional fossil fuels has forced today's generation to look for alternate fuel sources. Fuel cells have emerged as a promising new technology due to their use of non-depleting, non- fossil and clean source reactants/fuels. Hue and cry, over the years, about the enormous environmental problems from conventional fuel sources has also been instrumental in the renaissance of fuel cells.

Among all types of fuel cells, the Polymer Electrolyte Membrane Fuel Cell (PEMFC) is considered one of the best alternative power sources for the terrestrial, stationary, and portable applications due to its simplicity, reliability and efficiency. Though the theoretical efficiency that can be achieved by this fuel cell is 100%, the attainable practical efficiency is only approximately 50%. The single most important factor for this loss in efficiency is the large overpotential occurring for the oxygen reduction reaction (ORR) of the PEMFC. One of the solutions to decrease this overpotential and increase the overall performance of a fuel cell is to increase its temperature of operation. However, the use of the Nafion membrane limits the temperature at which the PEMFC can be used. Thus, the single most redeeming solution to increase the rate of the ORR is the use of effective electrocatalysts. Platinum has been the most effective catalyst to date but its cost has accounted for the astronomical price of fuel cells, which is one of the major reasons barring its commercialization.

In the 1970s-80s, various metal macrocycles such as porphyrins were tested for their rate of oxygen reduction; they showed considerable activity but their chemical stability in acidic medium was very poor [Kiros,Y.,1996b; Tamizhmani,G.,1994; Lalande,G.,1997b]. Since then efforts have been concentrated in incorporating transition metals to carbon supported Pt to form

electrocatalysts, as transition metals exhibit both good stability and activity [Kiros,Y.,1996b; Lalande,G.,1997b].

Ball milling is a very prevalently used technique for fabrication of nano-structured materials [Wronski,Z.,S.,2001], but only since the last two decades, this technique has being extensively used for fabrication of electrocatalysts for fuel cells. This technique is being elaborately used by Lalande et al. [Denis,M.,C.,1999;Denis,M.,C.,2000;Gouerec,P.,2000; Lalande,G.,1997a;Lalande,G.,1999;Lalande,G.,2000;Schulz,R.,1998] for the fabrication of various Pt-M alloy electrocatalysts, where M = transition metals, for the hydrogen oxidation reaction. The effect of ball milling catalysts for ORR has of yet not been investigated.

Co is one of the best base metals for making a good catalyst. Being a transition metal, it fulfills the prerequisites of a good catalyst by having an optimum nearest neighboring distance and empty d orbitals. There are various groups [Kiros,Y.,1996(a-b);Gamburzev,S.,97; Mukerjee,S.,1995(a-b);Neto,A.,O.,1999;Neeraj,M.,2001;Paulus,O.,A.,2002;Shukla,A.,K.,2001] which have successfully pronounced higher electro-catalytic activity of Pt-Co for the ORR but the mode of fabrication was different than ball milling.

This thesis addresses the development of novel Pt-Co electrocatalysts for PEMFC. Ball milling was investigated as the method of fabrication to reduce the cost associated with production of the catalysts together with an effort to increase the rate of oxygen reduction.

Specific objectives of this project were:

1. Fabricate, PtCo, transition metal alloy electrocatalysts to reduce the high cost associated with catalysts in PEMFC by alloying Pt with a cheaper element and simultaneously improving the slow kinetics of the ORR in PEMFC.
2. Optimize the ball milling parameters, such as, milling time, ball to powder weight ratio (BPR), process control agents (PCA) to produce the maximum particle size refinement and increase surface area.
3. Develop a fundamental understanding of the effects of microstructural characteristics on the catalyst layer. Investigate the electrochemical behaviour of the electrocatalysts in both acidic and alkaline medium at room temperature and high temperature.

Methodology employed to meet the objectives:

1. Use of high-energy ball milling to fabricate PtCo alloy electrocatalysts.
2. Use of PCA and lixiviation process to improve surface area of the electrocatalysts.
3. Use of SEM find particle sizes, TEM to find particle sizes, powder dispersion and diffraction patterns, EDS to determine bulk elemental composition of the electro-catalysts, XRD to find crystallite sizes and phases formed, and XPS to detect the surface elemental composition and oxide species formation. Use of cyclic polarization and potentiodynamic polarization to investigate the electro- chemical behaviour of the electrocatalysts.

Chapter Two

Literature Review

A fuel cell is an electrochemical device that converts the chemical energy of the reactants to electricity and water. The concept of fuel cells was first detected by Sir William Grove, a Welsh judge and amateur scientist in 1839, when he discovered that by reversing the water electrolysis, electricity could be produced from oxygen and hydrogen. The overall fuel cell reaction can be summarized as [Laraminie, J., 2002]:

$$H_2 + 1/2O_2 = H_2O + \text{electricity} \quad \ldots\ldots\ldots\ldots\ldots\ldots\ldots\ldots\ldots\ldots 2.1$$

Fuel cells work on the same principal as batteries to generate electricity but unlike batteries, the reactants are supplied from an external source. Also, theoretically, a fuel cell operates as long as it is supplied with fuel and oxidants. Fuel cells are also more efficient than internal combustion engine, because they do not follow Carnot's law. Additionally, unlike the internal combustion engine, the efficiency of fuel cells is not strongly dependant on operating power. Thus, high power density and high efficiency are another advantage of this technology. Furthermore, the use of non-depleting, non- fossil and clean source reactants/fuels has made this a highly desirable technology. The growing interest in fuel cells is also due to its noiseless, pollution-less power generation. They typically require very low maintenance and are quite simple to fabricate. Apart from these advantages, fuel cells are also highly reliable and durable power generating sources. Fuel cell has high endurance and is unlikely to experience a catastrophic breakdown. This technology also has an ability to co-generate hot water and low temperature steam with electricity.

Though having numerous advantages, the drawbacks of this technology are that, fuel cells are highly cost ineffective (refer Appendix A), and though the theoretical efficiency achieved by a fuel cell could be 100%, the attainable efficiency is only approximately 50-60% [Kordesch, K.,1996; Larminie,J., 2002].

There are various kinds of fuel cells in the market. The working principal of all fuel cells is the same and they differ mainly on the basis of electrolyte used and working temperature. The electrolyte is the heart of all the fuel cells and hence fuel cells can broadly be classified into five categories on the basis of the electrolyte used. Table 1.1 summarizes the details of various kinds of fuel cells in use.

Table 1.1 *Types of fuel cells, their electrolytes, working temperatures and applications [Larminie,J.,2002]*

Type of Fuel Cell	Electrolyte	Working Temperature	Applications
Alkaline Fuel Cells (AFC)	KOH	90-100°C	Military space flights
Phosphoric Acid Fuel Cells (PAFC)	H_3PO_4	175-200°C	Electric utility & transportation
Molten Carbonate Fuel Cells (MCFC)	Li, Na, K_2CO_3	500-650°C	electric utility
Solid Oxide Fuel Cells (SOFC)	ZrO duped Yttrium	800-1000°C	Stationary power units
Polymer Electrolyte membrane Fuel Cells (PEMFC/PMFC)	Poly Perfluoro-Sulfonic acid	50-100°C	Electric utility, portable power transportation
Direct Methanol Fuel Cells (DMFC)	Poly Perfluoro-Sulfonic acid	50-100°C	Portable power transportation

2.1 Polymer Electrolyte Membrane Fuel Cells

Among the various types of fuel cells in use, the *'Polymer Electrolyte Membrane Fuel Cell'* is the most attractive fuel cell, because of its simplicity and efficiency. Polymer electrolyte membrane fuel cell (PEMFC) is also called *'Solid Polymer Fuel Cell'* (SPFC), and *'Polymer Electrolyte Fuel Cell'* (PEFC) due to its use of a solid polymer membrane as an electrolyte. Apart from the general advantages of a fuel cell, PEMFCs also have the advantages of low corrosion and fewer electrolyte management problems due to the use of the solid polymer electrolyte. Though the membrane puts a limit on working temperature, it also provides quick start up. Moreover, the PEMFC is able to withstand large pressure differentials. Due to its numerous advantages, PEMFCs, developed by General Electric, was the first type of fuel cell to find an application-power source for NASA's Gemini space flights in the 1960's. Now days, PEMFCs are used in a wide range of applications, from extraterrestrial to terrestrial systems extending to distributed power, heat production units and portable systems. The automobile industry is expected to be the major user of PEMFCs.

2.2 Principles of Operation of the Polymer Electrolyte Membrane Fuel Cell

This section briefly outlines the working principle and construction of a polymer electrolyte membrane fuel cell. It also discusses factors affecting efficiency of PEMFCs.

A schematic presentation of the cross-sectional area of a single PEMFC is shown in Fig 2.1. The main component of this fuel cell is a Membrane Electrode Assembly (MEA), which is essentially made up of a membrane, catalyst layers and gas diffusion layers.

The electrolyte membrane, generally 50-175μm thick, is made of 'Nafion', which consist of 'perfluorocarbon sulphonic acid ionomer'[Gottesfeld,S.,1998]. These polymer membranes

have long-term chemical stability under both reductive and oxidative environments. These membranes also act as gas separators and allow only protons to cross over.

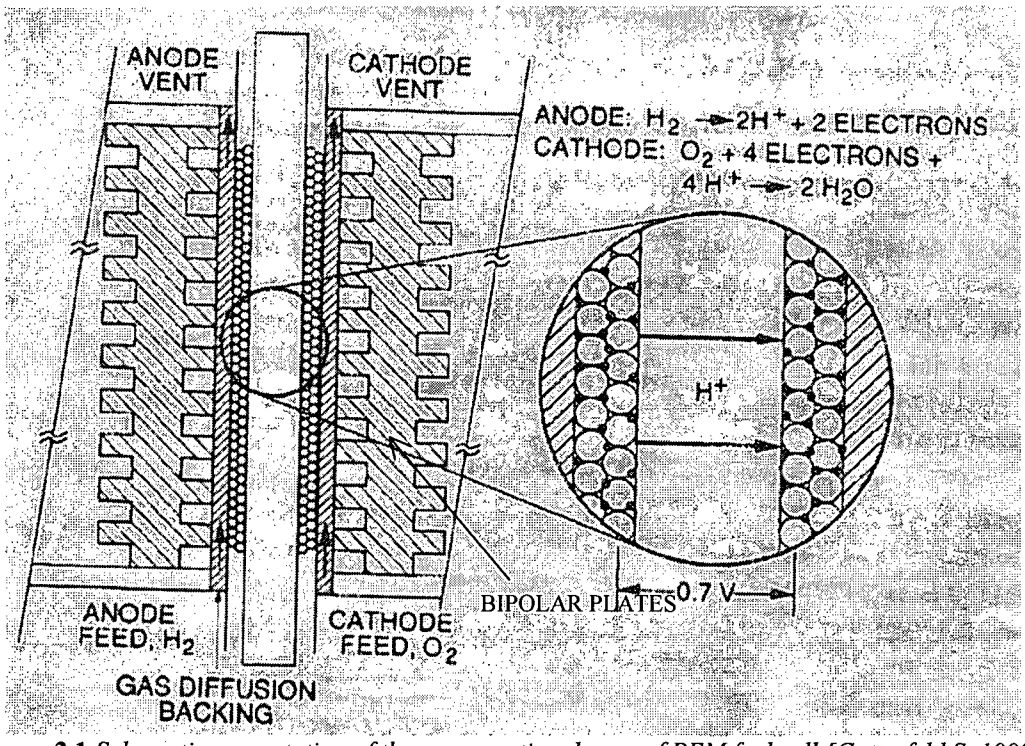

Figure 2.1 *Schematic presentation of the cross-sectional area of PEM fuel cell [Gottesfeld,S.,1998]*

Immediately adjacent to the membranes are the electrodes on each side, which consist of a 5-50μm thick [Gottesfeld,S.,1998] film of dispersed catalysts. The electrode where oxidation of hydrogen takes place is called 'anode' whereas the electrode at which reduction of oxygen takes place is 'cathode'. Each of these electrodes/catalyst layers is in immediate contact with the backing layer. Backing layers are made up of hydrophobized porous carbon paper or carbon cloth. These provide electrical contact between electrodes and bipolar plates and ensure uniform diffusion of gas to the catalyst layers on the respective sides of the MEA. Backing layers also provide passage to water formed from the reaction and thus help remove excess water from the cell. These layers are typically 100-300μm [Gottesfeld,S.,1998]. On the outer side of the unit

cell are the current collector plates having machined flow channels, these are also called bipolar plates. Bipolar plates separate the reactant gases, connect the cell electrically and provide mechanical support [Costamagma,P.,2001; Gottesfeld,S.,1998;Steele,B.,C.,H.,2001;Vloemn, L.,J.,M.,J., 1993;Wilson,M.,S.,1992; Wronski,Z.,S.,2001].

The electrochemical reactions taking place at the two electrocatalysts are given by the following equations:

Anodic reaction

$$H_2 = 2H^+ + 2e- \qquad E^\circ = 0.0V \ldots\ldots\ldots\ldots\ldots\ldots\ldots\ldots 2.2$$

Cathodic Reaction

$$1/2O_2 + 2H^+ + 2e^- = H_2O \qquad E^\circ = 1.229V \ldots\ldots\ldots\ldots\ldots\ldots\ldots\ldots 2.3$$

The overall reaction generating electricity is given by equation 2.1. The reversible standard potential of this overall fuel cell reaction calculated by Gibbs free energy of formation is found to be 1.23V [Bockris,J.,O.,M.,1969].

Temperature and pressure have strong influence on the electrode potential of the fuel cell reactions. There is a steep decline in electrode potential with increasing temperature [Kinoshita,K.,1992]. This is due to the lower theoretical efficiency of energy conversion devices such as fuel cells at higher temperature. But potential increases with increase in pressure. This is because the limiting current density increases with an increase in the solubility of the oxygen and solubility increases with increase in pressure [Kinoshita,K.,1992]. Figure 2.2 shows the trend of reversible standard potential for H_2/O_2 reaction (equation 2.1) as a function of temperature [Kinoshita,K.,1992].

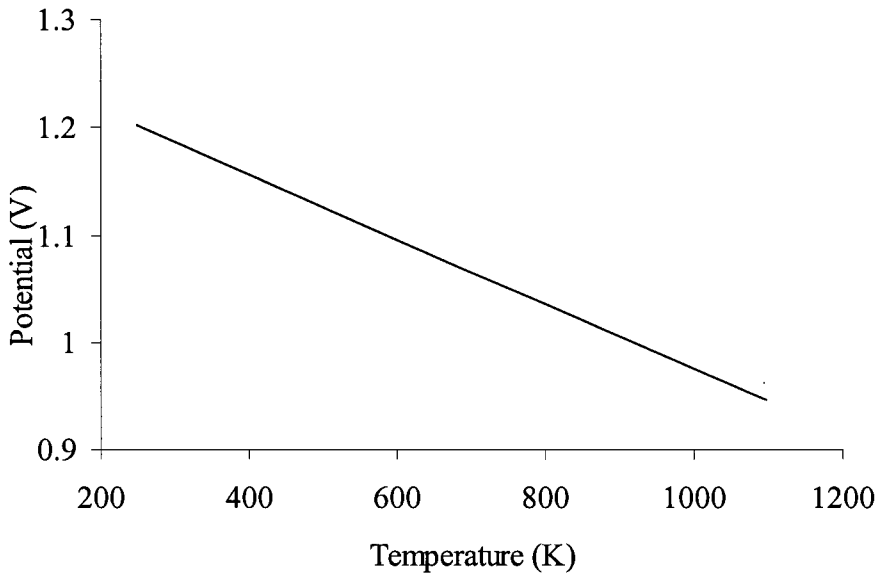

Figure 2.2 *Reversible standard potential for H_2/O_2 reaction as a function of temperature [redrawn, taken Kinoshita,K.,1992]*

Also, the standard electrode potential deviates from the equilibrium value when electrical work is performed by the cell. This deviation from the equilibrium value is the called overpotential. Figure 2.3 shows the current-voltage curve, also known as 'Polarization /Performance' curve of the PEM fuel cell. This curve depicts various overpotentials occurring at a given potential. These overpotentials are comprised of mass-transport overpotential (concentration losses), a reaction overpotential (activation losses) and a resistance overpotential (ohmic losses).

For a redox reaction at one electrode, the current density, i, at a given overpotential (η), is calculated by the Butler-Volmer equation [Bockris,J.,O.,M.,1969]:

$$i = i_o [\exp(\alpha_A nF\eta/RT) - \exp(-\alpha_C nF\eta/RT)] \quad \text{.....2.4}$$

Where, i_o is the exchange current density, α_A and α_C are the transfer coefficient for the anodic and cathodic reactions, n is the no. of electrons taking part in the reaction, F is faraday's

constant (96485 coulomb/mol), R is the gas constant (8.314 $Jmol^{-1}$ K^{-1}), T is the temperature (K).

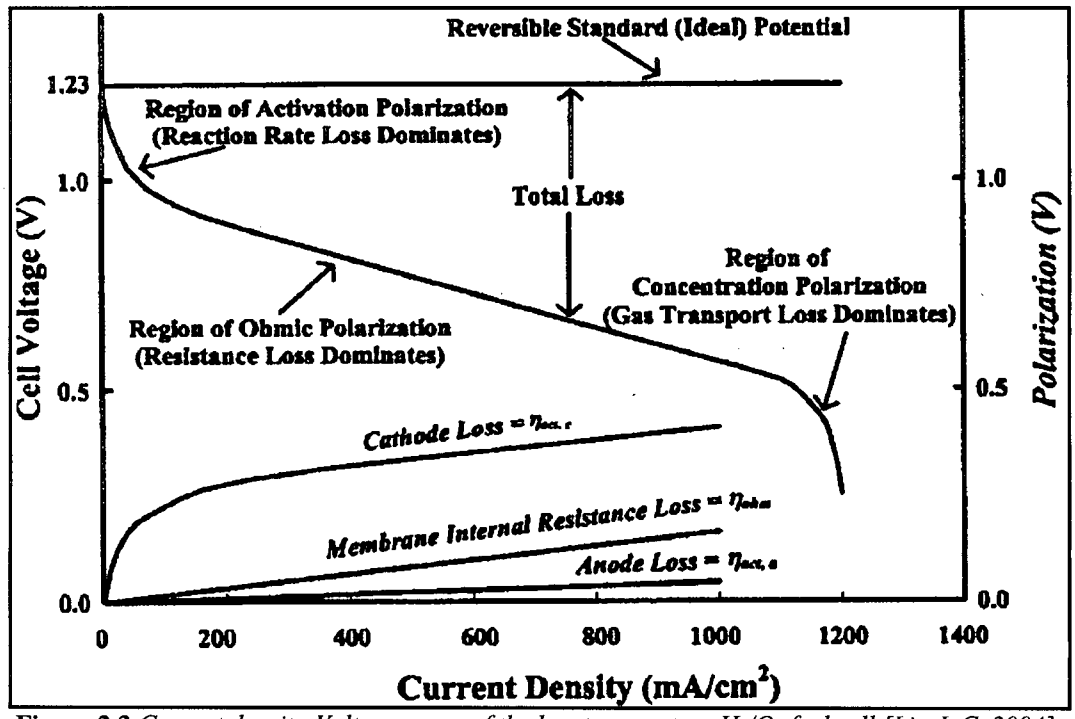

Figure 2.3 *Current density-Voltage curve of the low temperature H_2/O_2 fuel cell [Lin,J.,C.,2004]*

This exchange current density, i_0 and Tafel slope, β are the kinetic parameters which determine the performance of a fuel cell. This equation holds true only when the charge transfer dominates the reaction at small values of η and i [Carrette,L.,2000;Bockris,J.,O.,M.,1969; Greef, R.,1985;Kinoshita,K.,1992;Kordesch,K., 1996; Larminie,J.,2002; Lin,J.,C., 2004].

These overpotentials, which are one of the major reasons for the low performance of a fuel cell, can be decreased by increasing the temperature [Kinoshita,K.,1992]. The increase in temperature decreases the internal resistance of the cell and also overcomes the mass transport limitations caused by diffusion of reactants and improves the movement of protons from the

anode to the cathode. Thus, increase in temperature of operation enhances the performance of PEMFC.

2.3 Electrocatalysis in Polymer Electrolyte Membrane Fuel Cells

The term *'electrocatalysis'* is commonly applied to the systems where the oxidation or reduction requires a strong interaction of the reactant, intermediates, or the product with the electrode surface. The main motive of the electrocatalysis is to seek to provide alternative, lower energy of activation pathways and hence permit the sluggish reaction to occur at high current density close to equilibrium [Greef,R.,1985].

Electrocatalysis of PEMFCs is a simple phenomenon where protons are transported from the anode to the cathode through the electrolyte and electrons are carried to the cathode over an electrical circuit. On the cathode, oxygen reacts with protons and electrons forming water and producing heat. The overall electrode process in a PEMFC is summarized by the equations 2.2 and 2.3 in section 2.2. Among the two reactions, the ORR is slower and more complex than hydrogen oxidation because of the following reasons [Costamagna,P.,2000]:

(i) the strong O-O bond and the formation of highly stable M-O or M-OH species, where M =metals like Pt, Co etc,

(ii) the possible formation of a partially oxidized species(H_2O_2) and

(iii) difficulty in determination of rate determining step for this reaction .

2.3.1. Mechanism of Oxygen Reduction Reaction:

The oxygen reduction reaction can proceed by two overall pathways in aqueous electrolytes:

1. Direct four electron pathway:

   a) In an alkaline electrolyte

   $O_2 + 2H_2O + 4e^- = 4OH^-$ $E^\circ = 0.401V$.....2.5

   b) In an acidic electrolyte

   $O_2 + 4H^+ + 4e^- = 2H_2O$ $E^\circ = 1.229V$.....2.6

The direct, four-electron mechanism takes place only on highly active catalysts at small current densities or at high temperatures. It should be noted that all the potentials are with respect to Normal hydrogen electrode (NHE).

2. Peroxide pathway:

   a) In an alkaline electrolyte

   $O_2 + H_2O + 2e^- = HOO^- + OH^-$ $E^\circ = 0.065V$ 2.7

   $HOO^- + H_2O + 2e^- = 3OH^-$ $E^\circ = 0.867V$ (peroxide reduction), or,

   $2HOO^- = 2OH^- + O_2$ (peroxide decomposition)

   b) In an acid electrolyte

   $O_2 + 2H^+ + 2e^- = HOOH$ $E^\circ = 0.670V$ 2.8

   $HOOH + 2H^+ + 2e^- = 2H_2O$ $E^\circ = 1.77V$, or,

   $2HOOH = 2H_2O + O_2$

The direct four electron pathway is preferable as it does not involve peroxide species in solution and the charge efficiency (faradaic efficiency) of the reaction is greater. From equations 2.7 and 2.8 oxygen reacts to hydrogen peroxide with retention of the O-O bond. The decomposition of the peroxide occurs catalytically with the formation of chemisorbed oxygen.

$$M\text{-}O + H_2O + 2e^- = M + 2OH^-, \text{ or} \quad \ldots\ldots 2.9$$

$$M\text{-}O + 2H^+ + 2e^- = M + H_2O$$

This energy of the M-O bond is a measure for the observed voltage loss/overpotential. The chemisorbed oxygen can be desorbed according to the following equation:

$$2M\text{-}O = 2M + O_2 \quad \ldots\ldots 2.10$$

and can once more react with H_2O or H^+ [Kinoshita, K.,1992;Carrette,L.,2000; Kordesch , K.,1996].

2.4 Parameters Affecting Electrocatalyst Performance

Electrocatalytic activities are controlled by the intrinsic chemical activities of the surface. The fundamental requirement for a good performance of an electrocatalyst is availability of maximum number of sites along with high intrinsic activities of sites for the reaction, good electrical conductivity, good interaction with ionomers and reactant gas access [Friedrich,K.,A.,2002]. Apart from these, the various parameters affecting performance of an electrocatalyst are:

a) <u>Particle Size:</u> Since catalysis is surface phenomena, it is expected to be improved by decreasing catalyst particle size and thus increasing surface area. The relationship between particle size and surface area can be calculated by the relationship [Min,M.,K.,2001]:

$$S=6/(\rho * d) \quad \ldots\ldots 2.11$$

Where, S is surface area, ρ is metal density and d is particle diameter (assuming that particles are spherical in shape). Figure 2.4 shows that an increase in Pt particle size from 2 to 4nm causes the Pt surface area to drop by half [Larminie,J.,2002;Suryanarayana, C.,2001]. Watanabe et al. [Watanabe,M.,1994] also supported the fact that the intercrystalline distance of

the metal on the carbon support is fundamental to the ORR and showed that smaller particle sizes are better for reactivity.

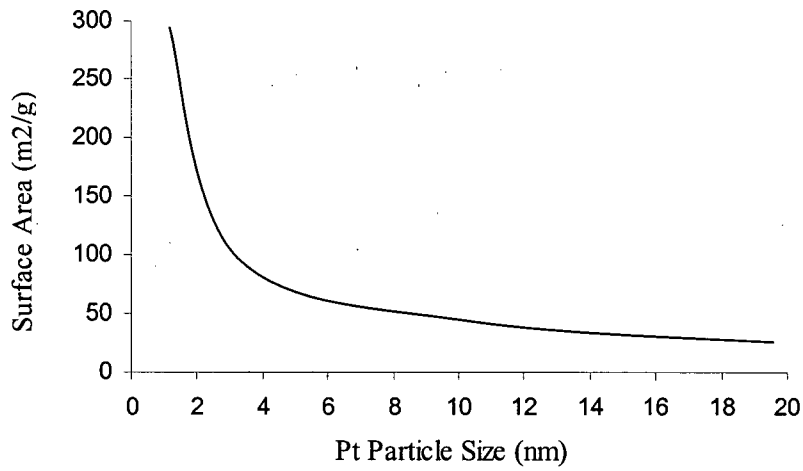

Figure 2.4 *Relationship of Pt surface area to particle size based on the spherical geometry [redrawn, taken Larminie,J.,2002]*

But over the years, numerous models derived by experimental results deviate from the above trend. Beard and Ross [Beard,B.,C.,1990] showed in their results that activity was best at a certain particle size (~5nm) and particles smaller than this size exhibited lower reactivities. This was specifically proved with the Pt-Co alloy system in their work. This theory was disputed by Kyong and workers [Kyong,T.,K.,1993] who observed with the Pt-Fe system that specific activity was independent of the particle size.

However, the Ross et al. [Beard,B.,C.,1990] model is supported by many researchers. Supporting Ross's interpretation, Mukerjee and co-workers [Mukerjee,S.,1995(a-b)], said that smaller particles might increase surface area, but this doesn't necessarily increase the number of active sites and thus catalytic performance. They suggested that as the particle sizes increases, the number of Pt atoms on (100) crystal facets increases with respect to those edges and corners

and thus the ORR becomes facile because there are more Pt (100) sites available. Ross et al. [Beard,B.,C.,1990] in their work had shown that the Pt (100) surface is more catalytically active than the Pt (111) plane for the ORR. They also suggested that as the particle size increases the d-band vacancy decreases and this in turn suggests that the adsorption strength of adsorbed oxygen species decreases. So, the reduction of intermetallics containing oxygen on a Pt surface occurs at a much faster rate [Mukerjee,S.,1995(a);Galeotti,M.,1996].

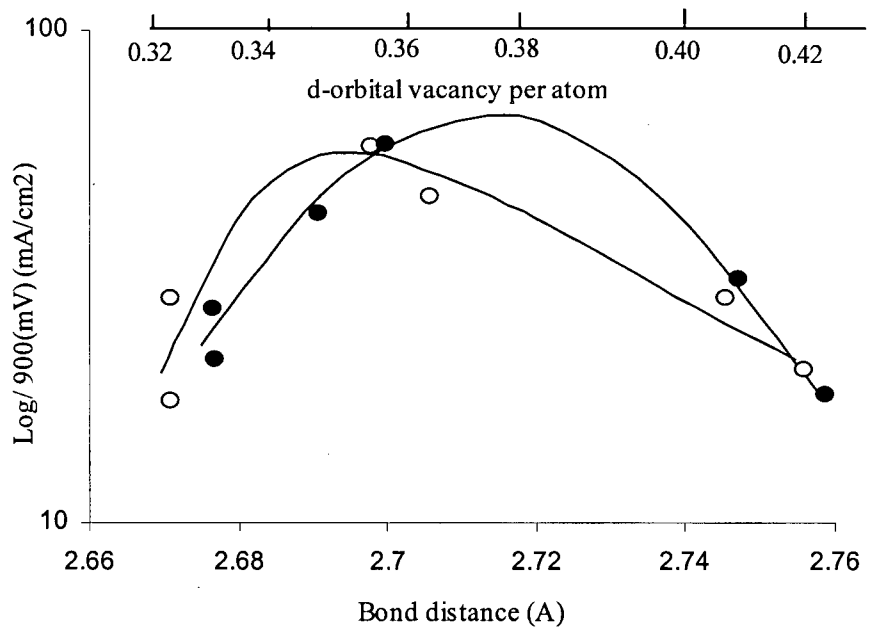

Figure 2.5 *Correlation of oxygen electrode performance of Pt & Pt alloy electrocatalyst with Pt-Pt bond distance (o) and the d-orbital vacancy of Pt(•) [redrawn, taken Mukerjee,S.,1995a]*

b) <u>d-d particle distance:</u> The catalytic activity varies even with the same surface area (same particle size) depending on the transition element used in the alloying process. Jalan and Taylor [Jalan,V.,1983] claimed that the Pt-Pt nearest neighboring distance was the main factor for enhanced ORR activity by many transition metal electrocatalysts such as Cr, V, Ti, W, Co, Ni and other metals like Ag, Al, Si, C. They reported increased specific activity with decreased Pt-

Pt distances in all cases. Figure 2.5 depicts that oxygen reduction activity of Pt and Pt alloy electrocatalysts follow a parabolic trend with d-d particle distance and empty d-orbitals.

c) Effect of heat treatment: Catalytic properties are also affected by heat treatment, such as annealing. It has been reported that as the powder is subjected to a higher heat treatment temperature, the particle size of the catalyst increases and thereby the dispersion is reduced indicating an increase in degree of alloying as heat treatment temperature increases [Min.,K.,M.,2001]. Cold working of particles also have significant effect on the electrocatalytic activity. The amount of cold work also changes surface activities (e.g. work hardened surfaces are more anodic than annealed surfaces). Heat treatment also affects Pt-Pt nearest neighboring distance [Wronski,Z.,S.,2001].

d) Thermal and chemical stability of nonstructural electrocatalysts: Pretreatment of catalyst such as heating under hydrogen or air, or, the electrochemical activation of the electrodes can also improve performance for the oxygen reduction. It is generally expected that the smaller the structure (active site) the more likely it is to move, aggregate, be poisoned, decompose, or change its shape, composition or morphology upon exposure to thermal and/or chemical cycling. Hence, thermal and chemical stability of the electrocatalyst also affects activity [Wronski,Z.,S.,2001] .

2.5 The Electrocatalyst Materials Used to date

Apart from the definition presented in an earlier section, '*electrocatalysis*' may also be defined as the acceleration of an electrode reaction by a substance that is not consumed in the overall reaction. Such a substance is called an *'electrocatalyst'* [Kordesch,K.,1996]. For PEMFCs, Pt and Pt alloys are the best electrocatalysts for both hydrogen and oxygen reduction

reaction. The reason is that no other electrocatalyst has approached the specific activity exhibited by Pt (or platinum alloys) in PEMFCs; firstly because of the demanding process of oxygen electroreduction and secondly, due to relatively adverse interfacial kinetics conditions of PEMFCs. Furthermore, alternative electrocatalysts developed have limited chemical stability in the acidic environment of the PEMFC as compared to Pt and Pt alloy catalysts [Gottesfeld,S.,1998].

As mentioned earlier, the Gemini space program developed by General Electric was the first to employ PEMFC technology for its operation. Electrocatalysts used in this space vehicle were unsupported Pt and Pd 'blacks' powders. The electrode loading used in this program was kept very high (> 30 mg/cm^2) to achieve reasonable cathode performance [Hoogers,G.,2003]. Such high loading and cost could only be supported in space applications (refer Appendix A). This Pt loading has to be brought down to produce cost-effective electrodes for commercial terrestrial applications.

This instigated interest in finding non-noble catalysts for the ORR. Literature shows that Ru-based chalcogenides, pyrolysed Fe and Co macrocycles[†], and metal carbides all show significant oxygen reduction. Base metals, e.g. Fe, Co, macrocyclic compounds (e.g. porphyrins, phthalocyanines, tetraazannulenes) [Kiros,Y.,1996b;Mizuhata,M.,1997;Tamizhmani,G.,1994] have long been known to possess the ability to electro-reduce oxygen.

Carbon supported Co-based systems [Neto,O.,1999; Beard, B.,C.,1990] in particular have

[†]Marcocycles are functional molecular architectures having well-defined mechanical and chemical properties. Pthalocyanines, porphyrins are all chelating systems having definite macrocycles. Porphyrin is a structure derived from porphine by replacing some of the hydrogen atoms around the outside with other groups of atoms. Porphine is a chelating agent in which a metal ion forms bonds with nitrogen atoms. A chelating agent is a substance whose molecules can form several bonds to a single metal ion. hese act as catalysts for many biological and chemical reactions [http://scifun.chem.wisc.edu/chemweek/Chelates/Chelates.html]

shown excellent performance and durability and were extensively used in metal-air battery systems. However, in acid, although both Fe- and Co- based system [Kiros,Y.,1996a; Watanabe,M.,1994] show oxygen reduction activity, overall performance and durability are poor. Attempts to improve these properties led to heat-treating M-organic macrocycles (M = Ni, Fe and Co) at high temperature (ca 600°C) [Cote.,R.,1997]. This did improve catalyst performance but corrosion and degradation were still issues as before, though of course, less severe. Ru-based catalysts were investigated after the discovery by Alonso-Vante and Tributsch [Vante,N.,A.,1997], that chevrel-phase Ru–Mo chalcogenides (sulfides and selenides) had significant oxygen reduction activity in acid electrolyte. In the 1990s, studies on ruthenium-oxide pyrochlore (Pb_2Ru_{2-x} Pb_xO_{7-x}) and on pyrolyzed Fe acetate adsorbed on 3,4,9,10-perylenetetracarboxylic dianhydride showed reasonable activities for the ORR in acidic media, but electrocatalytic activities of these materials were also less than that of Pt [Costamagna,P.,1998]. More recent work has shown that a carbon-supported Ru-Mo oxyselenide had similar mass activity for oxygen reduction to a carbon supported Ru catalyst but was a poorer catalyst for oxygen reduction when compared to Pt (by >100mV at 60°C) [Neto,A.,O.,2002]. This all showed that less expensive catalyst do show oxygen reduction activity under PEMFC conditions but are definitely inferior to Pt in terms of intrinsic activity.

This led to the introduction of supported Pt catalysts electrodes [Apple,A.,J.,T.,1987;Gottesfeld,S.,1998;Larminie,J.,2002]. In supported catalysts, Pt is highly divided and spread out on larger particles of finely divided supporting material, such as carbon.

This support not only increases surface area by huge proportions but also provide structural, conductive and durable support for the active metal particles. Figure 2.6 below shows Pt-electrocatalyst particles supported on a carbon particle.

Using a support particle for electrocatalysts, Los Alamos National Laboratory reported higher performance with a 10- fold size reduction in Pt loading from about 4mg/cm^2 to about 0.4mg/cm^2 with the use of carbon [Costamagna,P.,1998], whereas other researchers reported satisfactory performance with loading as low as 0.1mg/cm^2 and 0.05mg/cm^2 Pt [Kumar,G.,S.,1995] .

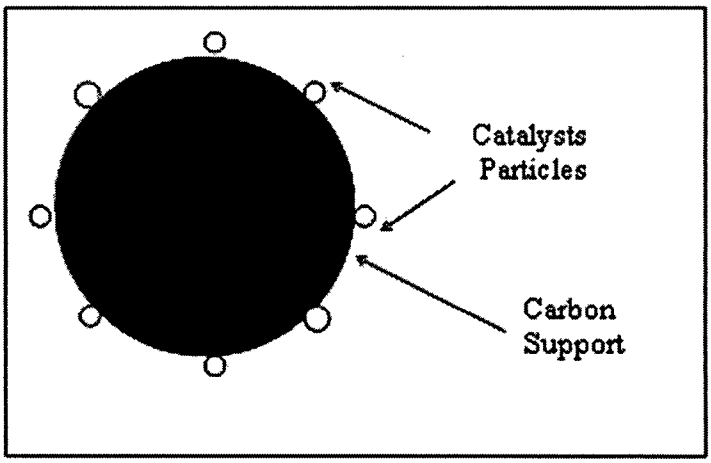

Figure 2.6 *Uniformly distributed Platinum catalyst particles on carbon support [redrawn, taken Laramine,J.,2002]*

In the past two decades, efforts have been made to further reduce the Pt content in the supported Pt catalysts by alloying Pt with 'other metals' than using Pt alone. These other metals are generally 'transition metals'. Transition metals are mainly chosen for making electrocatalysts because of the presence of empty d orbitals, their oxidation states and their electronic structures [Kordesch,K.,1996;Gottesfeld,S.,1998]. Transition metals generally used as electrocatalysts are Ag [Couturier,G.,1987], Ti [Couturier,G.,1987], Cr [Lalande,G.,1997], Mo[Neto,A.,O.,2002] Fe [Toda,T.,1999;Kyong,T.,K.,1993],Co[Kiros,Y.,1996(a-b); Neergat,M.,2001;Paulus,U.,A.,20002; Shulkla,A.,K.,2001;Toda,T.,1999], Ta [Couturier, G.,1987], Ni [Neergat,M.,2001;Paulus,U.,A., 20002; Shulkla,A.,K.,2001].

In one of the earliest attempts to use a transition metal as a suitable non-expensive catalyst for the ORR, Couturier et al. used Ag as an electrocatalyst [Couturier,G.,1987]. Ag was considered a suitable candidate because it has good peroxide decomposing properties in alkaline media; but its stability in alkaline media was an issue. Pt-Au alloy was also used as electrocatalysts in the space shuttle fuel cell [Couturier,G.,1987] but the cost demoralized further research on this electrocatalyst alloy system.

Srinivasan et al. [Mukerjee,K.,1995(a-b)] reported much cheaper Cr as one of the most promising transition metals for the ORR electrocatalyst. They attributed the performance to the parabolic dependence of electrocatalytic activity to both the Pt-Pt interatomic distance and the d-band vacancy. Luczak et al. [Luczak,F.,J.,1984;Luczak,F.,J.,1987] also claimed better activity for Pt-Cr or Pt-Co-Cr alloy catalysts than Pt. Though Couturier et al. [Couturier, G.,1987], who tested Pt-Cr, Pt-Ta, Pt-Cr-Ta alloy electrocatalysts for ORR agreed that Pt-Cr showed better catalytic activity due to optimum interatomic spacing, they pointed out that in long hours of operation, Cr leaches out in the solution (acidic) causing degradation in the performance. They reported better electrocatalytic activity for Pt-Cr-Ta than Pt-Cr electrocatalyst. The higher activity of Pt-Cr-Ta was attributed to the corrosion resistant behavior of Ta. Significant electrocatalytic activity for O_2 reduction was also reported with Pt-Cr /C [Lalande,G.,1997b] and Pt-Ir/C [Cote,R.,1997] catalysts prepared by the sol-gel method.

Min et al. [Min,K.,M.,2001] reported higher specific activity for Pt-Ni electrocatalysts among carbon based Pt-M (where M= Co, Cr, Ni) alloy electrocatalysts prepared by the incipient wetness method. The activity of all these Pt-M electrocatalysts was reported higher than Pt alone catalysts. They attributed this higher activity to the reduced Pt-Pt neighboring distance due to alloying of catalysts, reiterating the fact as others [Min,K.,M.,2001;Kiros,Y.,1996a] that the

ORR on platinum's surface is a structure sensitive reaction. While, Shukla et al. [Neergat,M.,2001; Shukla,A,K.,2001] reported higher oxygen reduction activity for binary Pt-Co/C than Pt-Ni/C, Pt-Cr/C and Pt-Co-Ni/C, Pt-Co-Cr/C ternary alloy electrocatalysts prepared by chemical method. Paulus et al. [Paulus,U.,A.,2002] on the other hand reported significant activities for both Pt-Co/C and Pt-Ni/C electrocatalysts from E-TEK. Figure 2.7 compares the activity of 20 wt% PtCo/C electrocatalysts in the ratio of 3:1 and 1:1 with the same wt% Pt/C in the acidic medium. Significant activity is seen for the Pt_3Co/C (ca. 2-3) and small activity enhancement for PtCo/C (ca. 1.5) in comparison of Pt/C catalysts. There is a 50mV increase in the oxide potential with the use of PtCo(Ni) catalysts. They speculated the reason for this shift of 50mV in the oxidation potential of the Pt surface atoms with the addition of Ni or Co as being a result of the fact that

> "..... if Ni (Co) atoms are stable in the surface under ORR conditions, they are probably 'oxidized' and have one or more ligands attached throughout the ORR potential. These OH ligands attached give rise to an effect on OH formation on neighboring Pt atoms analogous to the common-ion effect in solution chemistry, i.e., the presence of OH species on the surface repels like species from forming nearby and thus exhibit higher activity for ORR"

They also tested PtNi/C in the same ratio but found that as the nickel content in the PtNi/C alloy increased, it became unstable at oxygen electrode potentials and gave higher peroxide yield. They reported that 3:1 Pt-Co(Ni)/C catalysts (Fig. 2.7; only PtCo/C voltammogram has been shown due to its direct significance with this project) showed the same H_{upd} (hydrogen under potential deposition) region and typically the same adsorption and desorption features as Pt/C catalyst in the potential regions between 50 and 300mV. 1:1 PtCo/C catalyst did not show any of these features. They also reported lower Tafel slopes for the Pt catalysts in 0.1M $HClO_4$ than carbon supported Pt in 0.05M H_2SO_4 or a singe crystal Pt electrode in the same solution. They attributed this difference to the variation in the electrolyte used and to the influence of anion adsorption [Paulus,U.,A., 2002].

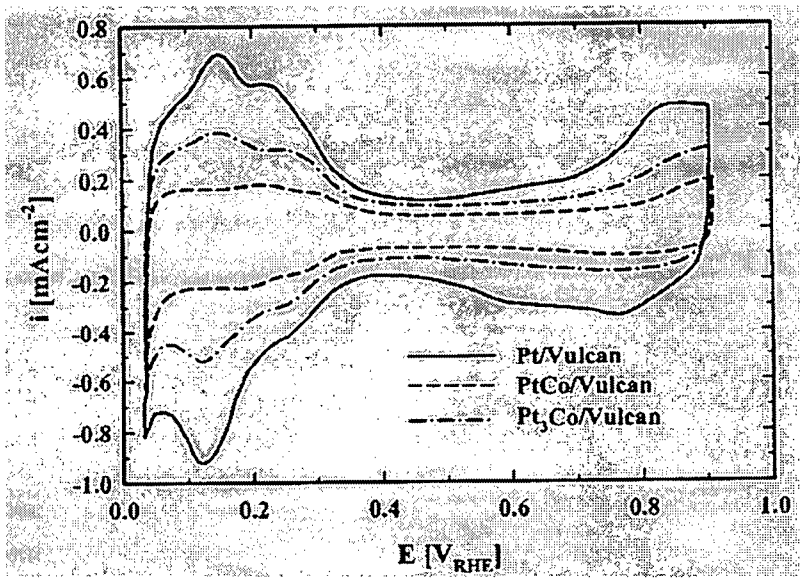

Figure 2.7 *Base voltammograms of the standard supported Pt catalysts compared to the supported Pt_3Co and PtCo catalyst in 0.1M $HClO_4$ (Ar saturated) at room temperature , rpm=900, scan rate=50mV/s [Paulus,,U.,A., 2002].*

Toda et al.[Toda, T.,1999] also reported significant activity, ca. 10 times more , for sputtered Pt-Ni, Pt-Co and Pt-Cr than Pt film prepared from the same method. Paulus et al. suggested that the reason of this increase may be because transition metals corrodes from the surface region due to elaborate pretreatment of sputtering leaving only Pt skin [Paulus,U.,A.,2002]. Gamburzev et al. [Gamburzev,S.,1997] reported that the activity of ternary Pt-Co-Cr supported alloy catalysts was superior to Pt/C catalysts. They attributed this to the geometrical and electrical factors. Kiros et al. [Kiros,Y., 1996b] prepared supported PtCo and CoTPP (Cobalt Tetraphenylporphyrin) catalysts by an impregnation method. They interestingly found that CoTPP showed better performance than PtCo electrocatalysts and that in turn showed better performance than Pt alone catalyst. Figures 2.8 and 2.9 show the polarization curves and potential time curves of the same respectively. They, unlike Couturier et al. [Couturier,G.,1987], referred this activity to a roughening effect arising from dissolution of Co together with a smaller neighboring distance of Pt with the transition metals.

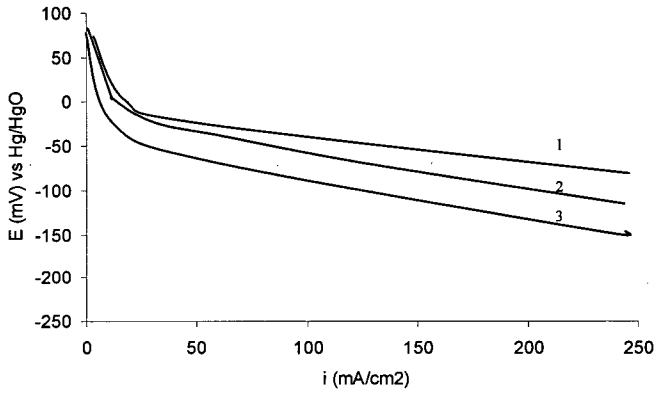

Figure2.8 *Comparison of polarization data of 1) CoTPP 2) Pt-Co and 3) Pt [redrawn, taken Kiros,Y 1996b]*

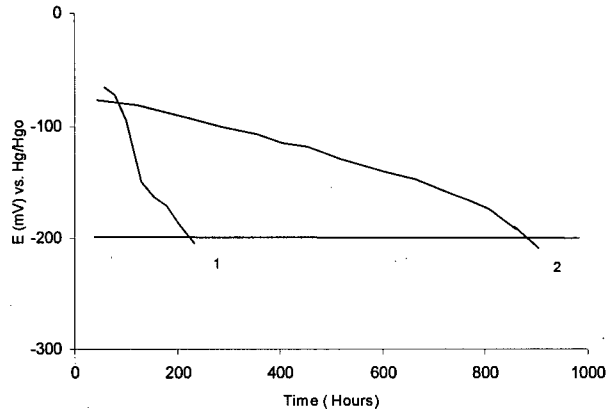

Figure 2.9 *Potential vs. time of the (1)CoTPP, (2)Pt-Co catalyzed electrodes[redrawn, Kiros,Y., 1996b]*

Though CoTPP had better activity than PtCo alloy electrocatalysts, it showed higher decay rates [Kiros,Y.,1996b]. Kiros et al. in another work [Kiros,Y.,1996a] examined the electrocatalytic properties of heat-treated Co, Pt and Pt-Co alloy electrocatalysts in alkaline medium. Higher activity was reported at 900°C (than 700°C) due to decreased lattice parameters, indicating a higher degree of alloying at higher temperature. Unlike others, they reported that 'unalloyed cobalt' contributed to the total performance improvement of the oxygen reduction reaction. This is highly likely due the heat treatment effect.

While all the above results report a higher catalytic activity for the ORR on Pt alloy catalysts than on Pt alone catalysts; Beard & Ross [Beard,B.,C.,1990] and Glass coworkers [Glass,J.,T., 1987] did not find an increased mass activity for Pt-Co or Pt-Cr as compared to Pt [Paulus,U.,A.,2002] and Paganin et al. [Paganin,V.,A.,1997] reported poor activity of Pt-M (where M = V, Co, Cr) compared with pure platinum having the same loading.

Ball milling is a prominent method for catalyst fabrication but it has been mostly used to synthesis the Pt based transition metal alloy for the hydrogen oxidation reaction and there is no evidence of using ball milling for the fabrication of electrocatalysts for ORR.

Sun et al. [Sun,L.,1997] used ball milling to prepare a Cu-Al alloy. It was found that the activity of the balled milled Cu-Al was much higher than vacuum induction melted Cu-Al and rapidly quenched Cu-Al alloy with the same atomic ratios. Since then various electrocatalysts like Pt-Ru [Lalande,G.,1997a;Denis,M.,C.,1999; Denis,M.,C.,2000] and Pt-Mo [Denis.,M., C., 2000] have been prepared for catalysis of the hydrogen oxidation reaction by the ball milling technique. Figures 2.10 and 2.11 show cyclic voltammograms and fuel cell polarization curves of 20 wt% PtRu (1:1) ball milled, 20 wt% PtRu (1:1) ball milled with XC-72 carbon, and 20 wt% Pt/C (E-TEK) electrocatalysts.

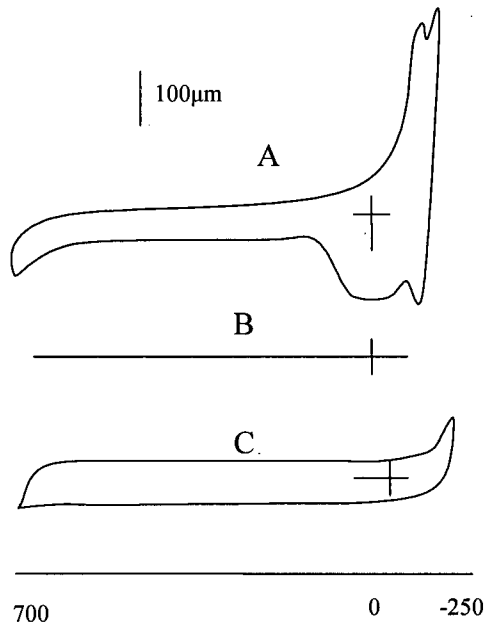

Figure 2.10 *Cyclic Voltammograms of (a) 20 wt% Pt on Caron Black (E-TEK), (b) $Pt_{0.50}Ru_{0.50}$ Ball milled alloy, (c) 20 wt% ball milled $Pt_{0.50}Ru_{0.50}$ milled a second time with XC-72R [redrawn, Lalande, G.,1997a]*

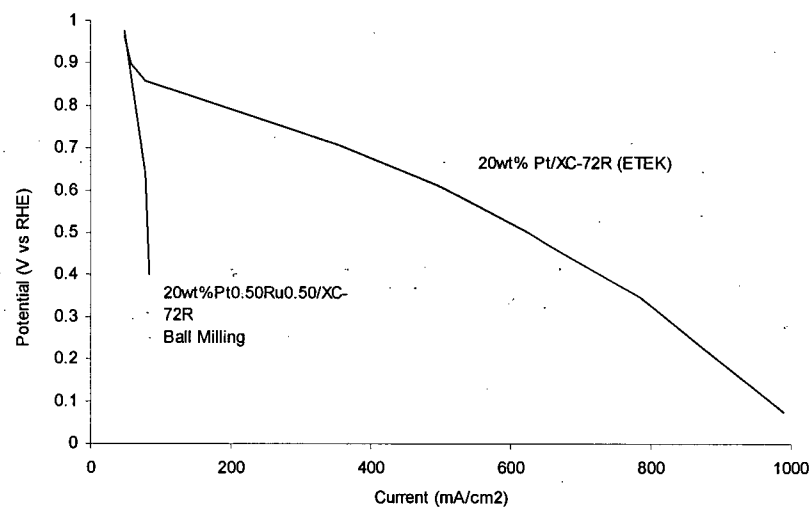

Figure 2.11 *Fuel Cell polarization curves of a 20 wt% ball milled $Pt_{0.50}Ru_{0.50}$ alloy, milled a second time with XC-72R. The 20 wt% Pt/XC-72R commercial catalyst (E-TEK) [redrawn, Lalande G., 1997a]*

Figure 2.10a shows the cyclic voltammogram of 20 wt% Pt on XC-72 carbon from E-TEK. The H_2 evolution/ adsorption and H^+ reduction peaks are clearly visible between 0 to –0.25V. Figure 2.10b is the voltammogram of ball milled $Pt_{0.50}Ru_{0.50}$ for 20hrs. This voltammogram is featureless with very little capacitive response and does not display any peak for voltages more cathodic than 0V. The authors suggest this lack of activity to a very small specific area of this material. Figure 2.10c shows slight improvement in the catalytic behaviour when milled with surface agent. Lalande et al. [Lalande,G.,1997a] suggested that this low activity of PtRu ball milled with carbon as surface agent might be because there were large size PtRu particles present even after ball milling with surface agents. Another possible reason suggested was that the active sites for H_2 oxidation were more or less obliterated by the carbon black covering them.

Figure 2.11 shows polarization curves of 20 wt% $Pt_{0.50}Ru_{0.50}$/C ball milled for 40hrs and 20 wt% Pt/C (E-TEK) tested in the fuel cell assembly. 20 wt% $Pt_{0.50}Ru_{0.50}$/C show very little current density as compared to commercial E-TEK catalysts suggesting that ball milling did not produce enough surface area inspite of the addition of surface agent [Lalande,G.,1997a]. Electrocatalysts fabricated by the ball-milled method are discussed in detail in section 2.7.

The above literature review shows significant variation in the activities obtained with the same alloy electrocatalysts. Tables 1.2 and 1.3 give the Tafel slopes and exchange current densities of the various electrocatalysts discussed with the method of fabrications and detailed description of the environment they were tested in.

Table 2.1 *Table summarizing kinetic parameters of oxygen reduction reaction on various electrocatalyst in alkaline medium*

Catalysts	Tafel Plot mV/dec	io (A/cm^2)	Conditions of testing			Fabrication Method	References
			Electrolyte	Temp.	Testing Mode		
Co/C	62	$0.316*10^{6\dagger}$	6.0M KOH	80°C	Gas Diffusion Elec. 3- electrode argmnt.	Chemical Synthesis followed by heat treatment at 700°C	Kiros,Y., 1996b
Co/C	59	$0.293*10^{6\dagger}$	6.0M KOH	80°C	Gas Diffusion Elec. 3- electrode argmnt.	Chemical Synthesis followed by heat treatment at 900°C	Kiros,Y., 1996b
Pt/C	58	$1.212*10^{6\dagger}$	6.0M KOH	80°C	Gas Diffusion Elec. 3- electrode argmnt.	Chemical Synthesis followed by heat treatment at 700°C	Kiros,Y., 1996b
Pt/C	59	$1.308*10^{6\dagger}$	6.0M KOH	80°C	Gas Diffusion Elec. 3- electrode argmnt.	Chemical Synthesis followed by heat treatment at 900°C	Kiros,Y., 1996b
Bulk Pt	106 119 120	$3.42*10^{-4}$ $8.54*10^{-4}$ $9.10*10^{-4}$	1.0M KOH	25°C 55°C 70°C	3- electrode argmnt	Sputtering	Couturier,G.,1987
Sputtered Pt	88 110 110	$8.69*10^{-5}$ $3.40*10^{-4}$ $3.40*10^{-4}$	1.0M KOH	25°C 55°C 70°C	3- electrode argmnt	Sputtering	Couturier,G.,1987
Pt/C (ETEK)	60	$8.2*10^{-7}$	1.0M NaOH	25°C	Pt(ETEK)+ Vulcan C +Teflon= Ink 3 electrode argmnt.	Commercial Catalysts	Perez,J., 1998
Pt Black	49	$2.2*10^{-13}$	30%KOH	-40°C	-	-	Kinoshita, K.,1992
Pt	150	$7*10^{-6}$	0.1M KOH	25°C	-	-	Kinoshita, K.,1992
Pt	53	$1*10^{-10}$	0.1 NaOH	25°C	-	-	Kinoshita, K.,1992
Pt	242 204	$4.17*10^{-4}$ $8.20*10^{-5}$	1.0M KOH	25°C 55°C	3 electrode argmnt.		Couturier,G.,1987

Table 2.1 *Table summarizing kinetic parameters of oxygen reduction reaction on various electrocatalyst in alkaline medium*, continued

Pt-Co /C(1:3)	59	$1.468*10^{6\dagger}$	6.0M KOH	80°C	Gas Diffusion Elec. 3- electrode argmnt.	Chemical Synthesis followed by heat treatment at 700°C	Kiros,Y., 1996b
Pt-Co/C (1:3)	61	$4.137*10^{6\dagger}$	6.0M KOH	80°C	Gas Diffusion Elec. 3- electrode argmnt.	Chemical Synthesis followed by heat treatment at 900°C	Kiros,Y., 1996b
Pt-Co/C (100:0)	50	$1.02*10^{-7}$	1.0M NaOH	25°C	Gas Diffusion Elec. 3- electrode argmnt	Chemical Synthesis followed by heat treatment at 1000°C	Neto.A.,O.,1999
Pt-Co/C (70:30)	49	$4.08*10^{-8}$	1.0M NaOH	25°C	Gas Diffusion Elec. 3- electrode argmnt	Chemical Synthesis followed by heat treatment at 1000°C	Neto.A.,O.,1999
Pt-Co/C (60:40)	49	$3.06*10^{-8}$	1.0M NaOH	25°C	Gas Diffusion Elec. 3- electrode argmnt	Chemical Synthesis followed by heat treatment at 1000°C	Neto.A.,O.,1999
Pt-Co/C (40:60)	48	$2.55*10^{-8}$	1.0M NaOH	25°C	Gas Diffusion Elec. 3- electrode argmnt	Chemical Synthesis followed by heat treatment at 1000°C	Neto.A.,O.,1999
Pt-Co/C (30:70)	46	$1.53*10^{-8}$	1.0M NaOH	25°C	Gas Diffusion Elec. 3- electrode argmnt	Chemical Synthesis followed by heat treatment at 1000°C	Neto.A.,O.,1999
Pt-Co/C (0:100)	40	$1.30*10^{-8}$	1.0M NaOH	25°C	Gas Diffusion Elec. 3- electrode argmnt.	Chemical Synthesis followed by heat treatment at 1000°C	Neto.A.,O.,1999
Pt-Cr	141 172	$4.17*10^{-6}$ $4.14*10^{-5}$	1.0M KOH	25°C 55°C	3- electrode argmnt.	Sputtering	Couturier,G.,1987
Pt-Ta	206 199	$3.52*10^{-5}$ $7.66*10^{-5}$	1.0M KOH	25°C 55°C	3- electrode argmnt.	Sputtering	Couturier,G.,1987
Pt-Cr-Ta	304 -	$2.88*10^{-4}$ -	1.0M KOH	25°C 55°C	3- electrode argmnt.	Sputtering	Couturier,G.,1987

† The value of the exchange current density looks erroneous but these are the results reported in the literature.

Table 2.2 *Table summarizing kinetic parameters of oxygen reduction reaction on various electrocatalyst in acidic medium*

Catalysts	Tafel Plot mV/dec	io (A/cm^2)	Conditions of testing			Fabrication Method	References
			Electrolyte	Temp.	Testing Mode		
Pt/C (ETEK)	60	$5.0*10^{-9}$	0.5M H_2SO_4	25°C	Pt(ETEK)+ Vulcan C +Teflon= Ink 3-electrode argmnt.	Commercial Catalysts	Perez, J.,1998
Pt Black	65	$4*10^{-10}$	20% H_2S0_4	70°C	-	-	Kinoshinta,K.,1992
Pt	145	$3*10^{-6}$	0.5M H_2SO_4	25°C	-	-	Kinoshita, K., 1992
Pt	65	$1*10^{-9}$	1.0N H_2SO_4	25°C	-	-	Kinoshita, K.,1992
Pt-Co/C (90:10)	58	$2.04*10^{-11}$	0.5M H_2SO_4	25°C	Gas Diffusion Elec. 3- electrode argmnt	Chemical Synthesis followed by heat treatment at 1000°C	Neto.A.,O.,1999
Pt-Co/C (70:30)	56	$5.1*10^{-13}$	0.5M H_2SO_4	25°C	Gas Diffusion Elec. 3- electrode argmnt	Chemical Synthesis followed by heat treatment at 1000°C	Neto,A.,O.,1999
PtCo/C (20wt% Metal on C)	65	$5.87*10^{1}$	-	95°C	MEA	Commercial Johnson Mattey Catalysts	Mukerjee, S.,1995 (a-b)

These differences in the activities and kinetic parameters can be attributed to the different methods employed for the fabrication of the electrocatalysts. Manufacturing methods have a great effect on particle size and surface area and hence, on the performance of the catalysts. Also, it should be kept in mind that some of the catalysts were tested in full MEA and complete fuel cell set up while others were evaluated in a conventional three-electrode electrochemical cell with aqueous electrolytes. Another important factor influencing the performance of the electrocatalysts tested in the 3-electrode arrangement is the amount of nafion content used to make the electrode sample. Furthermore, electrolyte used, types of gas sparged and variation in room temperatures and other environmental factors may also be the reasons for these discrepancies. This emphasizes that the results reported in the literature and the ones produced in this thesis are not directly comparable.

2.6 Method of Fabrication

This section addresses reasons for using nanocrystalline materials as electrocatalysts, various methods of fabrication of nanocrystalline electrocatalysts cited in the literature to date, justification of using mechanical alloying as the method of fabrication of electrocatalysts in this work, its mechanism and factors affecting its performance. It also illustrates references of previous use of ball milling for electrocatalysts fabrication by other authors.

2.6.1 Nanocrystalline materials

Nanocrystalline materials are polycrystalline, having an ultra-fine grain size in the order of 1-100nm [Wronski,Z.,S.,2001]. Because of the extremely small size of the grains, a large fraction of the atoms in these materials is located in the grain boundaries and thus the material exhibits enhanced combinations of physical, mechanical, and magnetic properties. Nanoparticles also have high surface area and all these properties capitalize great interest in nanostructured materials [Schulz,R.,1999; Surayanarayana,C.,2001;Wronski,Z.,S.,2001]

2.6.2 Methods of preparation of nanostructured materials

Nanocrystalline materials can be synthesized by a number of techniques like vapor phase, e.g., inert gas condensation [Rhun,V.,L., 2002], liquid phase, e.g., electro- deposition, rapid solidification [Perez,J.,1998;Mukerjee,S.,1993;Lalande,G.,1995;Lai,E.,K.,W.,1997], ion exchange [Wilson,M.,S.,1995], impregnation [Mizuhata,M.,1995;Kiros,Y.,1996b;Faubert,G., 1998], sol-gel synthesis [Cote.,R.,1997], solid state, e.g., mechanical attrition/ball milling [Lalande,G.,2000;Pharkya,P.,2003;Pharkya,P.,2004,Schulz,R.,1998], and incipient wetness method [Min, M.,K., 2000].

2.6.3 Mechanical Alloying - Mechanism

In this work, mechanical alloying is chosen as the method of fabrication because of the many advantages associated with this technique. Mechanical alloying (MA) is a solid-state process, in which a mixture of powder(s) is converted into an alloy by facilitating a series of high-energy collisions. In MA, powder charge is placed in a container, known as a bowl along with a suitable grinding media under inert or other controlled atmosphere. The materials are primarily crushed by the high-energy impact of grinding balls and frictional impact between balls and wall of the grinding bowl [Wang,W.,2000]. Figure 2.12 shows the schematic depicting the ball motion inside a ball mill. It consists of inducing a solid-state reaction between the components of a powder mixture by repeated mechanical deformations. This mechanical deformation is evident by the presence of a variety of crystal defects, such as dislocations, vacancies, stacking faults and increased number of grain boundaries that

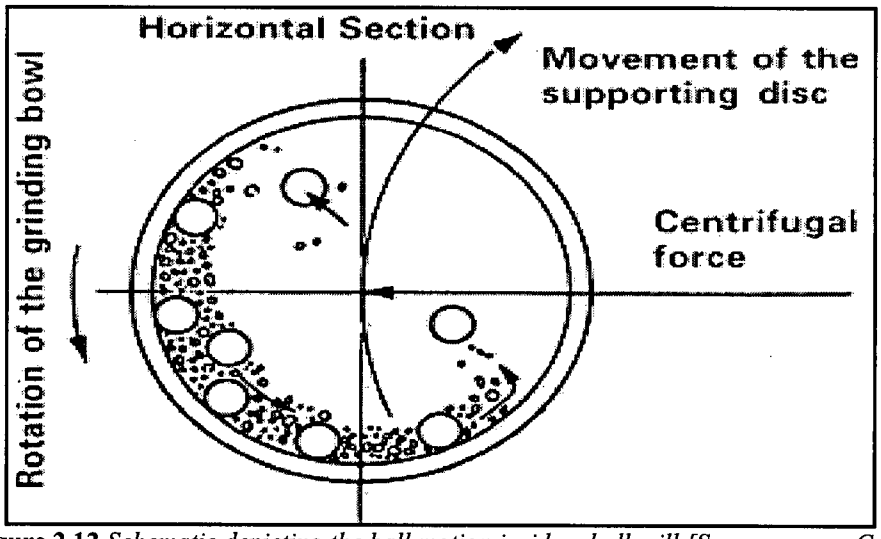

Figure 2.12 *Schematic depicting the ball motion inside a ball mill [Suryanarayna,C.,2001]*

increase interatomic diffusion, thereby allowing the solid-state reaction to proceed. Also, strain is induced in the lattice during milling that results in the crystal breaking into smaller particles [Suranarayan,C.,2001].

Mechanical alloying is a complex process and hence involves optimization of a number of variables to achieve a desired product phase and/or microstructure. Some of the important parameters that have an effect on the final constitutions of the powder are the material of the milling container, material and size of the grinding medium, milling speed, milling time, milling atmosphere, temperature and pressure of milling and ball to powder weight ratio. Some of the more important factors have been explained in detail below:

1. Milling container: The material used for making the milling container is of vital importance as some materials may be incorporated into the powder due to the impact of the grinding medium on the inner walls of the container. This may contaminate the powder or alter its chemistry. The material used for making the grinding balls are therefore chosen of high density and high abrasion resistance.

2.Grinding Medium: The density of the materials of the grinding medium should be high enough so that the balls create enough impact on the powder. The material of the grinding vessel (vial) and grinding medium (balls) should be made of the same material to avoid cross contamination. The size of the grinding medium also has an effect on the efficiency. Larger size and high density of the grinding medium are more beneficial as they provide greater impact to the powder particles. The raw material used for the mechanical alloying should be of smaller size than the grinding balls. This is because the powder particle size decreases exponentially with time and reaches a small value of a few microns only after a few minutes of milling [Suryanarayan,C.,2001].

3.Ball-to-powder weight ratio: The ratio of the weight of the balls to the powder (BPR) also called charge ratio (CR) [Surayanarayan,C.,2001], is an important variable in the milling process. It has a significant effect on the size of the particles obtained and the time required to achieve a particular phase in the powder being milled. The higher the BPR, the shorter is the time required. At a high BPR, because of an increase in the weight proportion of the balls, the number of collisions per unit time increases and consequently more energy is transferred to the powder particles.

4. Milling Speed: It is generally believed that a faster milling speed leads to higher energy input that produces smaller particle size in lesser milling time. But there is a critical speed above which balls are pinned down to the walls of the vial and don't exert any forces [Suryanarayan,C.,2001]. Therefore, this milling speed should be just below the critical speed so that balls fall down from the maximum height to produce the maximum collision energy. Another limitation to the maximum speed is that at high speed the temperature of the vial may increase to higher values. This may be advantageous in cases where diffusion is required to promote homogenization and alloying in the powders. But, this increase in temperature may be a disadvantage because this may accelerates the transformation process and results in the decomposition of supersaturated solid solutions or other metastable phases formed during milling. Additionally, there is also high possibly of contamination of powder at high temperatures. It has been reported that during nanocrystalline formation at higher milling speeds, increased rate of dynamical recrystallization increases the average crystal size and decreases the internal strain [Kuhrt,C.,1993].

5.Milling atmosphere: The major effect of the milling atmosphere is on the contamination of the powder. Therefore, the powders must be milled in an inert medium. Inert gases like Argon/ Helium have been found to prevent oxidation and contamination of the powder.

6.Temperature rise during milling: The temperature rise during milling is also an important issue in ball milling. Temperature during milling depends in kinetic energy of the balls and on the exothermic processes occurring during milling. An increase in temperature leads to higher mobility of atoms which cause the recovery and recrystallization processes to take place[Kuhrt,C.,1993]. Therefore, care should be taken to keep the temperature and pressure inside the milling container to an optimum level. Figure 2.13 shows the trend in particle refinement with different parameters like ball to powder ratio and milling time.

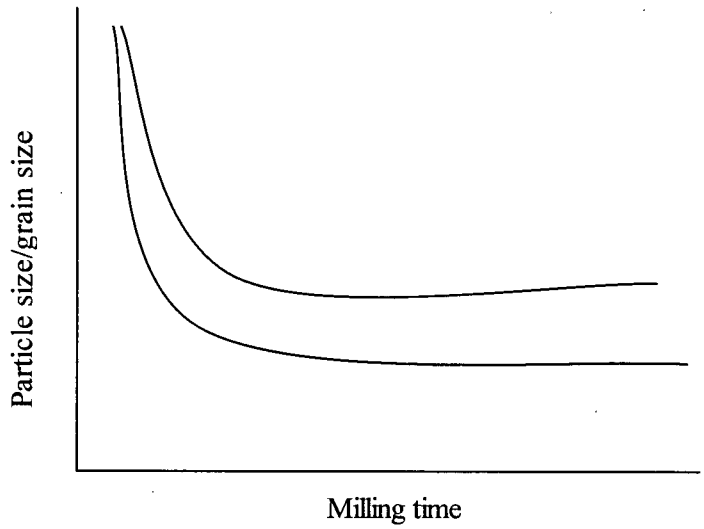

Figure 2.13 *Refinement of particle and grain sizes with milling time. Rate of refinement increases with higher milling energy, ball:powder ratio and low temperature[redrawn, taken Suryanarayana,C.,2001]*

2.6.4 Planetary Mill

In this study planetary ball mill called "Pulverisette 6" was used for the fabrication of electrocatalysts. This mill owes its name to the planet–like movement of its vial. This ball mill is suitable for research purposes in laboratory as it is small and mills the small quantity of powder in short time. The motion of a planetary mill involves rotation of the bowl about two separate parallel vertical axes, analogous to the rotation of the earth about the central axis of itself and about the sun. It consists of one sun disc and one or more planetary bowls. The sun disc rotates in one direction about its center while the bowls rotate in the opposite direction about their own axes. The centrifugal forces created by the rotations of the bowl around its own axis and of the rotating disc are applied onto balls and the powder mixture in the bowl. The impact is intensified when the balls collide with one another. The impact energy of the milling balls can be changed by altering the rotational speed of the sun disc. The advantage of this type of ball mill is not only that high energy can be obtained but also high impact frequency, which shortens the duration of the MA process [Suryanarayana,C., 2001;Wang.W.,2000]

Ivanov and co-workers were the first to explore mechanical alloying to obtain magnesium alloys for hydrogen storage [Ivanov,E.,1992]. Since then, a number of alloys have been prepared by this technique. Lately, the Dodelet group [Denis,M.,C.,1999,Denis,M.,C., 2000.,Lalande,G.,1997, Lalande,G.,1999, Lalande,G.,2000] has extensively incorporated the use of ball milling for the fabrication of electrocatalysts for hydrogen oxidation reaction in PEMFC.

The advantage of using MA is that it can fabricate materials not only in the same particle size range (2nm) [Schulz,R.,1998] as produced by other methods such as the ion-exchange method (2nm) [Mizuhata,M.,1995] or sol-gel synthesis (2-25nm) [Cote,R., 1997] but also renders irrelevant the immiscibility problem inherent to liquid processing in this system

[Wronski,Z.,S.,2001]. This is because mechanical alloying is a solid state processing technique and therefore limitations imposed by the phase diagram do not apply. It is also capable of producing metastable phases including supersaturated solid solutions, crystalline, quazi-crystalline, amorphous, and disordered intermetallic compounds [Surayanararan,C,2001]. Figure 2.14 shows the phase diagram of the PtCo binary alloy system, which shows the presence of ordered CoPt and $CoPt_3$ phases. CoPt has a tetragonal structure while $CoPt_3$ has a cubic structure [ASM handbook,ed.,Baker,H.]

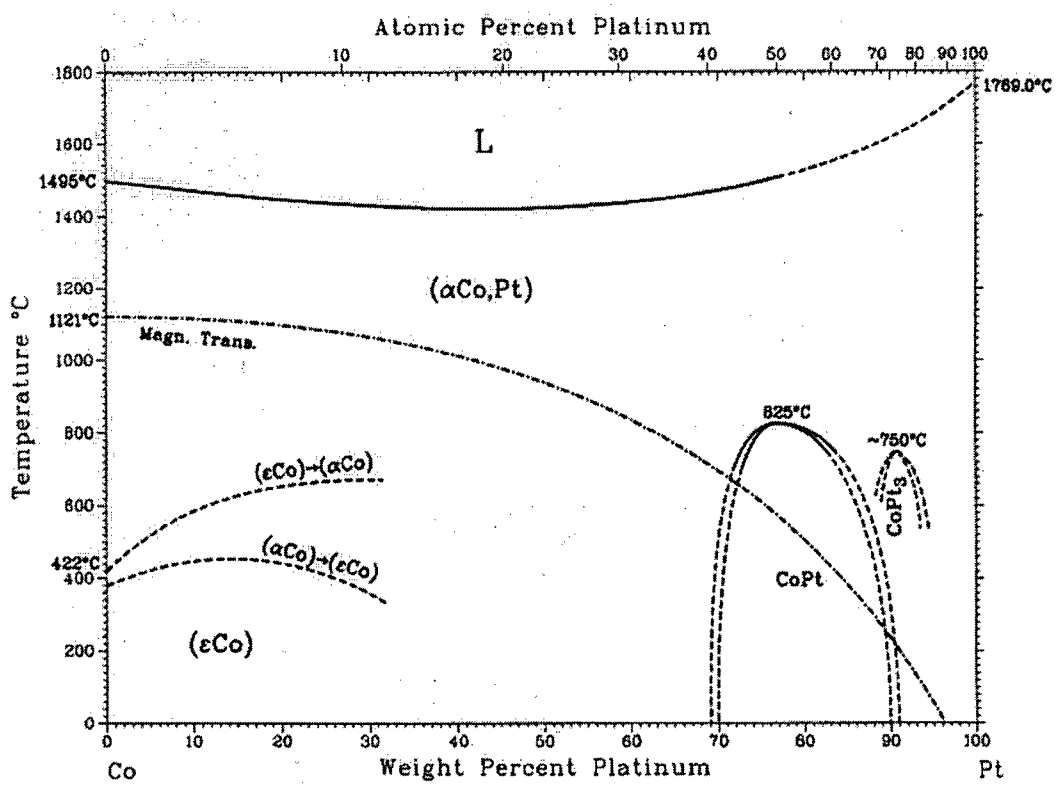

Figure 2.14 *Pt Co Binary Phase diagram [ASM handbook,ed.,Baker,H.]*

The other advantage to MA, when compared to other processes such as gas condensation and sputtering methods, is its ability to produce bulk quantities of material in the solid state at room temperature using simple equipment at commercially viable cost [Denis, M.,C.,2000; Suryanarayna,C.,2001; Wronski, Z.,S.,2001].

Although, this technique is capable of producing supersaturated solid solution in a wide range of compositions, the specific surface area of these materials is usually less than $1m^2/g$ [Schulz,R.,1998] due to cold welding of particles during milling process, which in turn, greatly affects the electrocatalytic performance of electrodes. This problem can be overcome by adding PCA. Dodelet et al. [Lalande,G.,1999, Denis, M.,C.,199] have extensively demonstrated that milling a second metal with the original powder can increase the porosity of the powder and hence overcome the limitation of low surface area [Denis,M.,C.,1999;Denis.,M.,C.,2000]. This second metal is called PCA. PCAs act as surface-active agents, adsorbing on particulate surfaces and interfering with cold welding by lowering the surface tension of the solid material. Usually, PCAs are organic compounds like stearic acid, hexane, oxalic acid, methanol, ethanol, acetone, heptane octane, toluene, etc [Suryanarayan,C.,.2001]. The majority of these compounds decompose, and are incorporated in the powder particles during milling, resulting in the formation of carbides and oxides, which uniformly disperse in the matrix [Denis,M.,C.,2000]. Therefore, PCA should be chosen such that it does not negatively affect the final activity of the electrocatalysts. The nature and quantity of the PCA used and the type of powder milled also determine the final size, shape, and purity of the powder particles. Use of a large quantity of PCA normally reduces the particle size by 2-3 orders of magnitude. Also, it has been reported that an increase of the PCA leads to an exponential decrease of the powder size for a given milling duration [Surayanarayan,C.,2001]. Denis et al. showed that PCAs could also play the

role of dispersive agent [Denis, M.,C.,2000]. The various dispersive agents used were Al [Denis,M.,C.,1998;Denis,M.,C.,2000; Gouerec,P.,2000;Schulz,R.,1998], MgH_2 [Gouerec,P., 2000; Lalande,G.,2000], Mg [Denis,M.,C.,1998]. Various PCAs used were NaF or MgH_2 [Denis, M.,C.,2000;Gouerec, P., 2000]. A number of authors have also suggested the use of lixiviation process [Denis,M.,C.,1998;Lalande,G.,2000;Schulz, R., 1998] to enhance the surface area of powder by many folds.

Various binary catalysts fabricated by ball milling, which were used for the anodic reaction in PEM fuel cells include Pt-Sn [Lalande,G.,1999], Pt- Mo [Gouerec,P., 2000], Pt-Ru [Lalande,G.,1997;Lalande,G.,1999]. Lalande et al. [Lalande,G.,2000] also reported the use of this technique to mill Pt powder with tungsten and molybdenum oxide [WO_2, WO_3, MoO_2 or MoO_3] to synthesize nanocomposites for the anode electrocatalyst of PEMFCs. As mentioned before, this technique still has to prove itself for the fabrication of high surface area catalysts for the ORR. This work is one such attempt to widen the perspectives of this technique for fabrication of the ORR electrocatalysts.

2.7 Working electrode used for electrochemical experiments

The choice of working electrode has a special significance in testing highly substrate sensitive electrochemical measurements. Solid electrodes based on carbon are widely used in electrochemistry because of the wide potential range over which they could be used, low background current, low cost, chemical inertness, and suitability for various sensing and detection applications [Wang,J.,1994].

In this project, a glassy carbon electrode was used as the base for supporting powder material for electrochemical testing. This section discusses glassy carbon electrodes and normal pyrolytic carbon, their methods of fabrication, and reasons for differences in performances.

2.7.1 Glassy-Carbon Electrodes

Glassy (or vitreous) carbon has been very popular for making solid electrodes because of its excellent mechanical and electrical properties, wide potential range, chemical inertness (solvent resistance), and relatively reproducible performance [www.epsilon-web.net].

Glassy carbon is different from pyrolytic carbon. Glassy carbon is an amorphous form of carbon that is chemically quite inert, whereas pyrolytic graphite has a more ordered structure with distinct, basal and edge planes. These edge planes are considerably more conducting than the basal plane, which makes pyrolytic graphite an inferior choice for making solid electrodes. Apart from this, durability of glassy carbon electrode is more than pyrolytic graphite electrode as pyrolytic graphite electrode abrades very quickly [www.epsilon-web.net].

2.7.2 Method of manufacture and lab procedure for the usage of GCE

Glassy carbon electrode (GCE) is prepared by means of a carefully controlled-heating program of a remodeled polymeric (penol-formaldehyde) resin body in an inert atmosphere. The carbonization process proceeds very slowly over the 300-1200°C temperature range to ensure the elimination of oxygen, nitrogen, and hydrogen. The structure of glassy carbon involves thin, tangled ribbons of cross-linked, graphite like sheets. Because of its high density and small pore size, no impregnating procedure is required [Wang, J.,1994]. However, surface pretreatment sites are usually employed to create active and reproducible glassy-carbon electrodes. Such pretreatment is usually achieved by polishing (to shiny mirror-like appearance)

with successively smaller alumina particles (down to 0.05μm). The electrode should then be rinsed with deionized water before use. Additional activation steps, such as electrochemical, chemical, heat or laser treatments have also been used to enhance the performance. Superior electron-transfer capability of this electrode can be achieved by removal of surface contaminants and exposure of fresh carbon edges. [Wang, J.,1994]

CHAPTER THREE

Experimental Details

This chapter describes the materials used for electrocatalysts fabrication, the technique used for fabrication and its setup, electrocatalysts fabrication process, various microstructural and electrochemical techniques used for the characterization of the electrocatalysts.

3.1 Materials

This section describes the materials that were used for the fabrication of Pt and Co alloy systems, PtCo and PtCo/C alloy electrocatalysts and the commercial catalysts purchased from E-TEK.

3.1.1 Materials used for electrocatalyst preparation

Electrocatalysts were made from Pt powder (99.9 + % purity, -325 mesh) and Co powder (99.5 % purity and –325 mesh) purchased from Alfa Aesar. Pt was used as noble metal and Co was used as non-noble/base metal. Vulcan XC-72R carbon black from Cabot® and stearic acid ($C_{18}H_{36}O_2$) from Mallinckrodt were used as the surface agents.

3.1.2 Commercial electrocatalysts used

Commercial catalysts used were 40% PtCo/C and 10% PtCo/C. The atomic percentages of both Pt and Co were in the ratio of 1:1. Both the catalysts were purchased from E-TEK. The carbon used for support material was Vulcan XC-72R.

3.2 Fabrication Technique

This section describes the ball milling setup, optimization of ball milling parameters like ball to powder ratio (BPR), surface agents and milling time. It also describes various alloy systems used for the optimization of the above-mentioned parameters.

3.2.1 Setup of Ball Milling

Milling was performed with a Planetary Mono Mill, "Pulverisette 6" from Fritsch. The mill can be seen in Figure 3.1. The milling was performed in 500ml grinding vial using 50 balls of 10mm diameter. Both the grinding crucible and the grinding media were made up of tungsten carbide (WC). This material was chosen for the crucible and the balls because it is highly abrasion resistant which minimizes contamination of catalyst powder and secondly, because of its high density which provides high impact energy during milling.

A Gas Pressure and Measurement (GTM) II system was attached to the ball mill to monitor in-situ temperature and pressure effects during the process. The lid and the grinding vial were hermetically sealed with a Viton O-ring. The maximum speed of the ball milling was 600rpm. Milling and cooling cycles could be set as per the desired conditions.

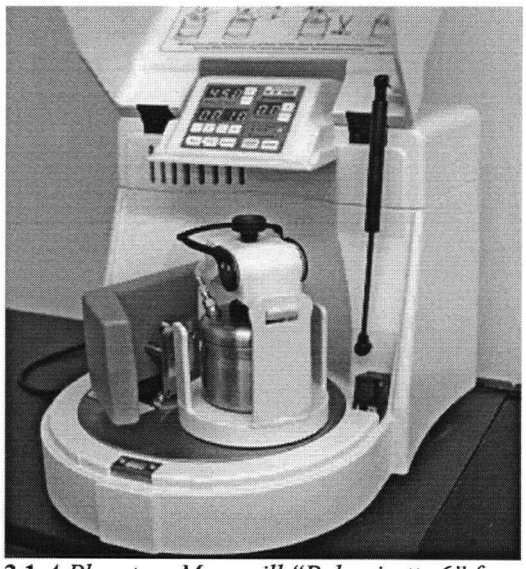

Figure 3.1 *A Planetary Monomill "Pulverisette 6" from Fritsch*

3.2.2 Optimization of Ball Milling Parameters

A number of alloy systems were prepared using different percentages of noble metal (Pt), base/non-noble metal (Co) and surface agents (carbon and stearic acid) to establish optimum ball milling parameters for fabrication of the electrocatalysts.

Amounts of stearic acid used were 2 wt.% and 20 wt.% and that of carbon XC-72R were 1 at.% and 20 at.%. All powder handling was performed in a glove box with Argon gas to minimize oxidation of the powder during milling. Argon gas was supplied into the tungsten carbide crucible through a lid after the vial was hermetically sealed with a Viton O-ring. BPR of 39:1 and 78:1 were used to prepare the alloy samples. High ratios were selected in order to achieve significant particle size refinement [Sun,L.,1997]. The rotation of the ball mill vial alternated between clockwise and counter-clock wise direction after each cycle. Though the maximum speed up to which mill could rotate was 600 rpm, milling speed of 450 rpm was used

for all experiments to avoid excessive heating of the vial. The milling/cooling cycles of 40/20, 30/30 or 20/40 min varied to keep the temperature in the desired range.

3.2.3 Optimization of Temperature and Pressure

Temperature and pressure in the vial increases with increase in ball-milling time. This has a direct effect on the particle size as particle size increases with increase in temperature due to sintering. The GTM (II) system was attached to the ball mill to monitor the sudden changes in temperature and pressure that are results of solid-state reactions. Figure 3.2 gives a temperature-pressure profile obtained by the GTM (II) system during 10hrs of ball milling for a milling/cooling cycle of 20/40min.

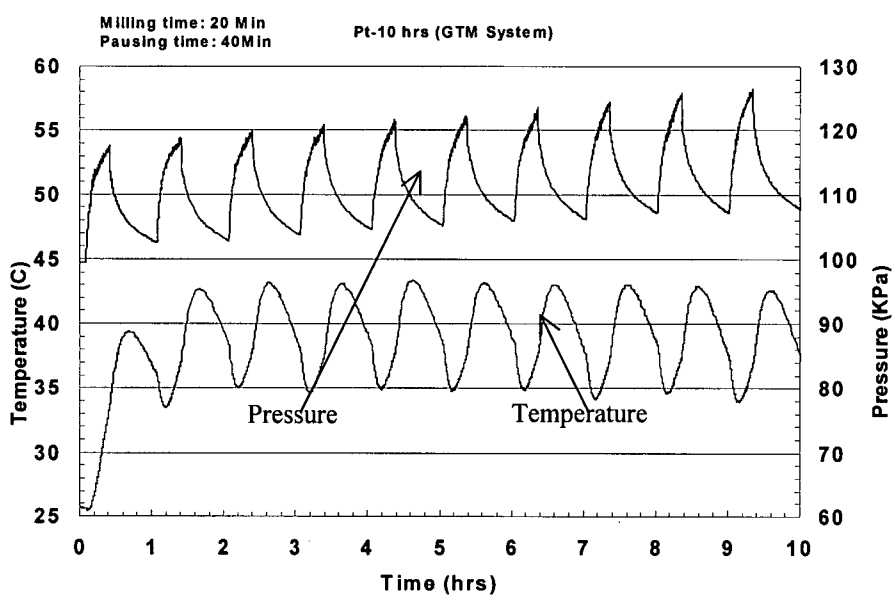

Figure 3.2 *A temperature-pressure profile obtained from GTM (II) system*

As shown, the pressure increases only slightly from 118 to 126kPa after 10hrs of milling, whereas the temperature in the vial was maintained constant and below 45°C due to selected cooling time between milling cycles

Table 3.1 lists the experimental conditions under which Co and Pt alloy systems were prepared for optimization of the ball milling parameters. For each sample a small amount of powder was taken out for characterization at time intervals of 5min, 30min, 10hrs, 40hrs and 90hrs.

Table 3.1 *Ball milling parameters for alloy systems*

Powder	Process control agent (PCA)	Wt.% PCA	BPR	Milling time (hrs)	Milling/Cooling time (min)	Atm.
Co	-	-	78:1,39:1	0.5,10,24,40	20/40	Argon
Co	$C_{18}H_{36}O_2$	2	78:1,39:1	10,40,70,90	20/40	Argon
Co	$C_{18}H_{36}O_2$	20	78:1	40,90	40/20	Argon
Co	Carbon XC-72R	20	78:1	0.5,10,40,90	20/40	Argon
Co	Carbon XC-72R and $C_{18}H_{36}O_2$	20	78:1	0.08,0.5,10, 40,90	30/30	Argon
Pt	-	-	78:1	0.5,10,40	30/30	Argon
Pt	Carbon XC-72R	20	78:1	0.5,10,40	20/40	Argon

3.2.4 Alloy Systems Prepared

A number of alloy systems were prepared with the conditions mentioned in Table 3.1. The nomenclature used for the various alloy systems fabricated is explained here:

- Co-10h-78: Cobalt milled for 10 hours with BPR of 78:1
- Co-40h-78: Cobalt milled for 40 hours with BPR of 78:1
- Co-40h-39: Cobalt milled for 40 hours with BPR of 39:1
- Co-90h-78: Cobalt milled for 90 hours with BPR of 78:1
- Co-10h-78-2%SA: Cobalt milled for 10 hours with BPR of 78:1 and 2 wt.% stearic acid as PCA
- Co-40h-78-2%SA: Cobalt milled for 40 hours with BPR of 78:1 and 2 wt.% stearic acid as PCA
- Co-90h-78-2%SA: Cobalt milled for 90 hours with BPR of 78:1 and 2 wt.% stearic acid as PCA
- Co-10h-78-20%SA: Cobalt milled for 10 hours with BPR of 78:1 and 20 wt.% stearic acid as PCA
- Co-40h-78-20%SA: Cobalt milled for 40 hours with BPR of 78:1 and 20 wt.% stearic acid as PCA
- Co-90h-78-20%SA: Cobalt milled for 90 hours with BPR of 78:1 and 20 wt.% stearic acid as PCA
- Co-10h-78-20%C: Cobalt milled for 10 hours with BPR of 78:1 and 20 wt.% carbon as PCA
- Co-40h-78-20%C: Cobalt milled for 40 hours with BPR of 78:1 and 20 wt.% carbon as PCA

- Co-90h-78-20%C: Cobalt milled for 90 hours with BPR of 78:1 and 20 wt.% carbon as PCA
- Pt-30min-78: Platinum milled for 30 min with BPR of 78:1
- Pt-10h-78: Platinum milled for 10 hours with BPR of 78:1
- Pt-40h-78: Platinum milled for 40 hours with BPR of 78:1
- Pt-40h-78-20%C: Platinum milled for 40 hours with BPR of 78:1 and 20 wt.% carbon as PCA

3.3 Fabrication Process for the electrocatalysts

Once the optimum ball milling parameters were established, the different electrocatalysts were prepared using different percentages of Pt, Co and C. This section details the procedure used for fabrication of the electrocatalysts.

3.3.1 Electrocatalysts Prepared

Four sets of electrocatalysts, $Pt_{0.25}$:$Co_{0.75}$-40h, $Pt_{0.25}$:$Co_{0.75}$-40h-20%C-30min, Pt:Co-45h-%C-5h* and $Pt_{0.75}Co_{0.25}$-45h-5h-1%C-lixiviated were prepared. All ratios are in atomic percent; the reason for no atomic percent in the * alloy electrocatalyst is explained below in the lixiviation section. The nomenclature used for the electrocatalysts fabricated is explained here:

(a) $Pt_{0.25}$:$Co_{0.75}$-40h: Pt and Co powders were mixed in the at. ratio of 1:3 and milled for 40hrs,

(b) $Pt_{0.25}$:$Co_{0.75}$-40h-20%C-30min: Pt and Co were taken in the atomic ratios of 1:3, ball milled for 40hrs and to this milled mixture 20% carbon (20% of the weight of the Pt and Co taken together) was added as surface agent and the whole mixture was milled for 30min,

(c) Pt:Co-45h-1%C-5h: Firstly, Pt-AR and Co-AR powders were ball milled for 5hrs separately, these milled powders were mixed together approximately in the atomic ratio of 1:15 and ball-

milled for 40hrs, then C, in the amount of 1% of the weight of the Pt and Co powders, was added to this milled mixture and milled for another 5hrs,

(d) $Pt_{0.75}Co_{0.25}$-45h-1%C-5hrs-lixiviated: Pt:Co-45h-1%C-5h alloy electrocatalyst was lixiviated according to the method explained in the lixiviation section (section 3.3.2). These fabricated electrocatalysts were then compared with 10% Pt-Co/C (50:50 at.%) and 40% Pt-Co/C (50:50 at.%) commercial E-TEK electrocatalysts.

3.3.2 Lixiviation Process

One of the electrocatalysts (Pt:Co-45h-1%C-5h) was lixiviated to further improve the surface area. Lixiviation is a process by which the electrocatalyst is mixed in an acidic medium such that it leaches some of the non-noble/base metal resulting in porous surfaces. This results in increase in surface area of the electrocatalyst. It was due to this reason the percentage of Co in this electrocatalysts was kept high.

The electrocatalyst (Pt:Co-45h-1%C-5h) was mixed with 20μl of distilled water and 30μl of 1M Hydrochloric acid from Fishers. The whole suspension was then ultrasonically agitated for 12hrs. This suspension was filtered using Fishers filter paper P2. The whole suspension was washed with deionized water for several times to remove any Cl^- or H^+ formed during the lixiviation reaction. The filtered suspension was then dried at 110°C for 12hrs.

3.4 Microstructural Characterization

This section describes the various microstructural techniques used for the physical characterization of the electrocatalysts.

3.4.1 Scanning Electron Microscopy (SEM)

Particle morphology and bulk elemental composition were analyzed using a Hitachi S-3500N scanning electron microscope equipped with energy dispersive x-ray spectroscopy (EDS).

The use of EDS analysis for bulk analysis has been reported in the literature [Couturier,G.,1987]. The working distance for EDS measurements was 15mm. The powder samples were placed on the carbon tape to make them conductive. The carbon tapes were then stuck on metal stubs to remove any extra charging during testing.

3.4.2 Transmission Electron Microscopy (TEM)

Particle sizes and diffraction patterns of the electrocatalysts were determined from Hitachi 800- S Transition electron microscope operated at 200KeV/20mA. TEM specimens were prepared by making suspension of electrocatalysts powder in ethanol by ultrasonically agitating for 1 minute. 2-3 drops of this suspension were dropped onto clean copper holy grids of 3.05mm diameter, and were subsequently, dried in air for 10-15 minutes. The indexing of diffraction pattern was done with the diffraction equation [Hunter,E.,E.,1993]

$$rd=L\lambda$$

where, L is camera constant, λ is the wavelength of x-ray source used, d is interplanar spacing and r is radius of a ring.

3.4.3 X-Ray Diffractometry (XRD)

Lattice parameters, crystallite size and phase identification were determined from X-ray diffractograms. X-ray diffraction (XRD) patterns were recorded with a Siemens D-5000 diffractometer using CuK_{α} radiation (λ=1.54056A°). The operating conditions of 40KeV/30mA were used. The diffraction patterns were recorded at an angular speed of 1.2°(2θ)/min with a step of 0.04°(2θ). Data accumulation and processing was performed using Diffrac^{plus} software from Bruker analytical x-ray systems. Phase identifications were performed with the help of PDF database and EVA V4.0 software.

Determination of Crystallite sizes and Microstrains

The broadening of the peak is usually the result of the presence of fine crystallites and microstrains. Crystallite sizes were determined from peak width at half height using the line-broadening technique and Scherer's equation. The peaks were at first corrected by subtracting the background noise as well as the $K\alpha_2$ line by employing the Rachinger correction method. The Scherer's equation is given by [Klug,H.,P.,1954],

$$D = \frac{0.9\lambda}{B\cos\theta} \quad \text{.....3.1}$$

Where, D is the crystallite size, λ is the wavelength of the x-ray used, B is the peak width at half maximum intensity, and θ is the Bragg angle. The integral breath method was used to analyze the broadening of the corrected profiles. The integral breath β is defined as

$$\beta = A_P / H_P \quad \text{.....3.2}$$

Where, A_P is the total area under the peak and H_P is the peak height. The total area under the peak was calculated using the Trapezoidal rule method. The amount of instrumental broadening was determined by using barium fluoride (BaF_2) as a standard. The separation of the instrumental broadening and the microstrain contribution to peak broadening was determined by using the Aqua and Wagner method [Farhat,Z.,2001]:

$$\beta^*_{specimen} = \beta^*_{total} - ((\beta^*_{instrumental})^2 / \beta^*_{total}) \quad \text{.....3.3}$$

where, $\beta^*_{total} = \beta\cos\theta_{K\alpha 1} / \lambda_{K\alpha 1}$ and $\beta_{instrumental} = \beta_{standard\ specimen}$

$$(\beta^*_{specimen})^2 = (1/D)^2 + (2\varepsilon d^*)^2 \quad \text{and } d^* = 2\sin\theta / \lambda$$

where, ε is the crystalline strain;

3.4.4 X-Ray Photoelectron Spectroscopy (XPS)

The presence of oxide layer and surface elemental composition were determined using X-ray photon electron spectroscopy. XPS was performed using a Leybold Max200 spectrometer.

The X-ray source was MgKα (hv=1253.6eV) and the operating conditions were 15KeV/20mA. The binding energy (BE) scale of the spectrometer was calibrated using a Au4f (84.0eV, BE) substrate. Survey scans were measured using pass energy of 192eV and narrow scans were measured with pass energy of 48eV. The experimental data were curve fitted with Gaussian peaks after subtracting a linear background. For gaussian peaks a slightly different full width at half maximum was used for different chemical states.

3.4.5 Surface area Measurements by BET analysis

Surface area measurements were performed on few catalysts by Quantachrome Autosorb automated gas sorption system and Micromeritics ASAP 2010. The ball-milled powders were characterized after heating and outgasing of the surface by using multi-point BET, and Nitrogen or Krypton as adsorbate gas [Denis,M.,C.,2000;Lalande,G.,2000; Kiros,Y.,1996a].

3.5 Electrochemical Measurements

This section illustrates electrochemical-testing apparatus, the two techniques namely, cyclic and potentiodynamic polarization, and various parameters used for it.

3.5.1 Apparatus

Electrochemical tests were performed with the help of a 273A Potentiostat by using Ecorr 352 software provided by Princeton Applied Research. Electrochemical measurements were analyzed using CorrView2 software. Figure 3.3 shows the 273A Potentiostat attached with personal computer and Figure 3.4 gives the schematic diagrams of the same. Figure 3.5 shows the rotating disc electrode apparatus. The Electrochemical cell used was K0064 jacketed cell with RDE0010 top. An RDE0008 glassy carbon electrode of 0.1254 cm^2 surface area was used as working electrode. It can be seen in Figure 3.6. Two thin platinum foils of $2cm^2$ surface area were used as counter electrodes. A K0077 saturated calomel electrode (SCE) placed in a K0065

reference electrode bridge tube with Vycor® frit was used as the reference electrode. The gases sparging was done with the aid of RDE0019 purge tube.

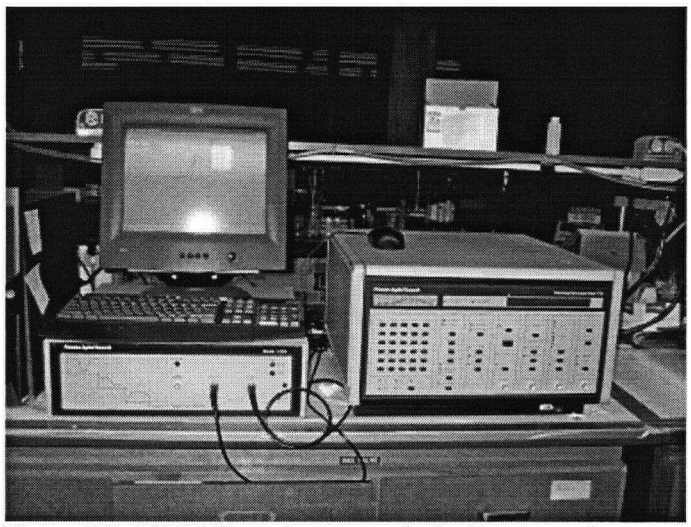

Figure 3.3 *A 273A Potentiostat attached with personal computer*

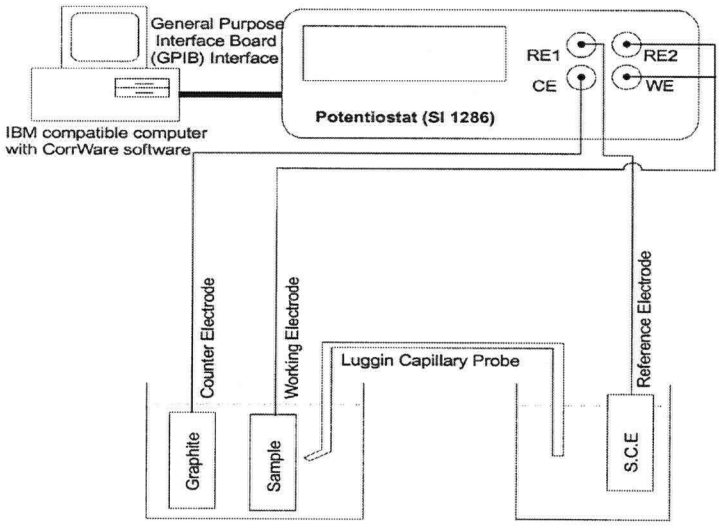

Figure 3.4 *The schematic of Potentiostat 273A potentiostat*

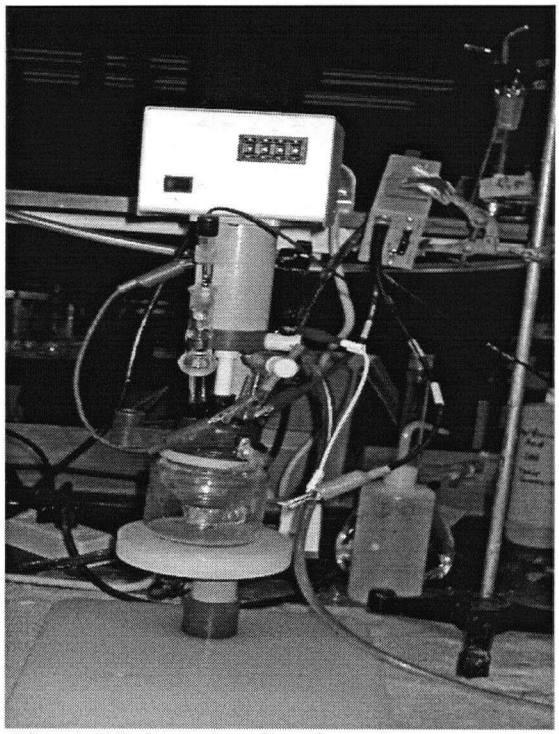

Figure 3.5 *A rotating disc electrode apparatus*

For high temperature testing, hot water was circulated around water-jacketed electrochemical cell with a pump from Cole Parmer company. The temperature of water was kept 3-5°C higher than required temperature to compensate for differential cooling.

3.5.2 Electrode Preparation

Polishing

The glassy carbon electrode was polished before every test to remove any oxide layer or electrochemical species formed on its surface. The electrode was polished with 1micron alumina paste for 5 minutes and then fine polished to 0.5micron. The electrode was then ultrasonically cleaned for 15 minutes with acetone and distilled water to remove alumina particles.

Sample Preparation

Samples for the potentiodynamic/cyclic potentiometry tests were prepared using 10 mg of catalyst mixed with 6μl of 5 wt% solution of recast Nafion (Aldrich) and 6μl of ethyl alcohol. 6μl of this suspension was then pipetted and spread onto a glassy carbon electrode (4mm diameter). The suspension was allowed to dry for 10-15 minutes in air and then dried with hot air for a minute. The amount of the catalysts mixed for sample preparation varied depending on the particle size of the powder. The bigger particles had lesser dispersion in Nafion and so more quantities were used to fully cover the GCE surface.

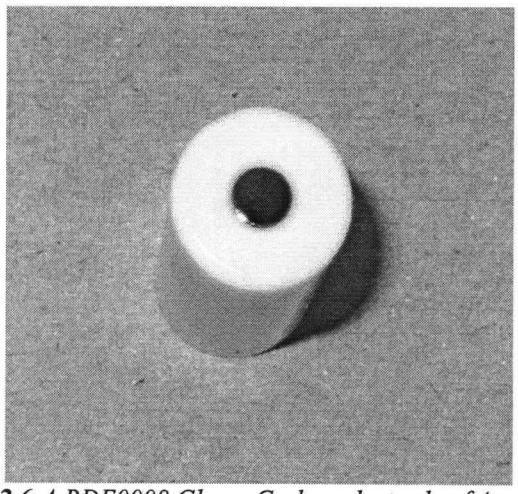

Figure 3.6 *A RDE0008 Glassy Carbon electrode of 4mm diameter*

3.5.3 Electrolyte and Temperature Range used

Electrochemical measurements were done both in acidic and alkaline medium. Acidic electrolyte was prepared using reagent grade sulfuric acid (0.5M H_2SO_4) with pH of 0.50. Alkaline electrolyte was prepared using reagent grade sodium hydroxide (0.25M NaOH) with pH of 13. The cell was saturated with oxygen for 45 minutes before the experiment and then continuously sparged during the experiment. All tests were conducted at room temperature

(22± 2°C) and higher temperature of 50±2°C to study the effect of temperature on the activity of the electrocatalysts.

3.5.4 Cyclic Polarization

Cyclic polarization was done to determine the oxidation/reduction peak and the relative current density of the catalysts. Cyclic polarization curves were obtained with the scan rate of 10mV/s. Cyclic polarization curves were recorded after running the three cycles at the scan rate of 100mV/s to give the initial redox behaviour and to stabilize the catalysts [Couturier,G.,1987]. The final scans at the scan rate of 10mV/s were recorded once the catalyst reached pseudo-steady state. The curves were recorded in the potential range of –0.2 to 1.0 to -0.2V vs. SCE in acidic medium and –0.6 to 1.0 to –0.6 vs. SCE in the alkaline medium. Potential were then converted to NHE for the ease in comparing with data in the literature.

3.5.5 Potentiodynamic Polarization

Exchange current density and Tafel slopes of the catalysts were determined using potentiodynamic polarization. Potentiodynamic measurements were recorded with the scan rate of 1mV/s. The curves were recorded in the potential range of 1.0 to -0.2V vs. SCE in the acidic medium and 1.0 to –0.6 vs. SCE in the alkaline medium. The CorrView2 software was used to obtain exchange current densities and Tafel slopes of the electrocatalysts

Tables 3.2 and 3.3 list the experimental conditions used in the above-mentioned tests.

Table 3.2 *Table summarizing details of Potentiodynamic Polarization tests*

S.No.	Samples	Electrolyte	Potential Range (V)	Scan Rate (mV/s)	Reference Electrode	Gas Purged	Temperature (°C) T ± 2
1.	Pt-AR	0.5M H_2SO_4 0.25M NaOH	1.0 to -0.2V 1.0 to -0.6V	1mV/s	SCE	Oxygen	22,50
2.	$Pt_{0.25}Co_{0.75}$-40h	0.5M H_2SO_4 0.25M NaOH	1.0 to -0.2V 1.0 to -0.6V	1mV/s	SCE	Oxygen	22,50
3.	$Pt_{0.25}Co_{0.75}$-40h-20%C-30min	0.5M H_2SO_4 0.25M NaOH	1.0 to -0.2V 1.0 to -0.6V	1mV/s	SCE	Oxygen	22,50
4.	PtCo-45h-1%C-5h	0.5M H_2SO_4 0.25M NaOH	1.0 to -0.2V 1.0 to -0.6V	1mV/s	SCE	Oxygen	22,50
5.	Lixiviated catalyst	0.5M H_2SO_4 0.25M NaOH	1.0 to -0.2V 1.0 to -0.6V	1mV/s	SCE	Oxygen	22,50
6.	10%PtCo-ETEK (1:1 a/o)	0.5M H_2SO_4 0.25M NaOH	1.0 to -0.2V 1.0 to -0.6V	1mV/s	SCE	Oxygen	22,50
7.	40%PtCo-ETEK (1:1 a/o)	0.5M H_2SO_4 0.25M NaOH	1.0 to -0.2V 1.0 to -0.6V	1mV/s	SCE	Oxygen	22,50

Table 3.3 *Table summarizing details of Cyclic Polarization tests*

S.No.	Samples	Electrolyte	Potential Range (V)	Scan Rate (mV/s)	Reference Electrode	Gas Purged	Temperature (°C) T ± 2
1.	Pt-AR	0.5M H_2SO_4 0.25M NaOH	-0.2 to 1.0 to -0.2V -0.6 to 1.0 to -0.6V	10mV/s	SCE	Oxygen	22,50
2.	$Pt_{0.25}Co_{0.75}$-40h	0.5M H_2SO_4 0.25M NaOH	-0.2 to 1.0 to -0.2V -0.6 to 1.0 to -0.6V	10mV/s	SCE	Oxygen	22,50
3.	$Pt_{0.25}Co_{0.75}$-40h-20%C-30min	0.5MH_2SO_4 0.25M NaOH	-0.2 to 1.0 to -0.2V -0.6 to 1.0 to -0.6V	10mV/s	SCE	Oxygen	22,50
4.	PtCo-45h-1%C-5h	0.5M H_2SO_4 0.25M NaOH	-0.2 to 1.0 to -0.2V -0.6 to 1.0 to -0.6V	10mV/s	SCE	Oxygen	22,50
5.	Lixiviated catalyst	0.5M H_2SO_4 0.25M NaOH	-0.2 to 1.0 to -0.2V -0.6 to 1.0 to -0.6V	10mV/s	SCE	Oxygen	22,50
6.	10%PtCo-ETEK (1:1 a/o)	0.5M H_2SO_4 0.25M NaOH	-0.2 to 1.0 to -0.2V -0.6 to 1.0 to -0.6V	10mV/s	SCE	Oxygen	22,50
7.	40%PtCo-ETEK (1:1 a/o)	0.5M H_2SO_4 0.25M NaOH	-0.2 to 1.0 to -0.2V -0.6 to 1.0 to -0.6V	10mV/s	SCE	Oxygen	22,50

Chapter Four

Results and Discussion

4.1 Characterization of As-Received Materials

The section below presents microstructural characterization of as-received materials, platinum and cobalt, done to analyze particle size, crystallite size, lattice parameters and various phases present.

Figures 4.1 and 4.2 give the scanning electron micrographs of as-received platinum (Pt-AR) and cobalt (Co-AR) purchased from Alfa Aesar respectively.

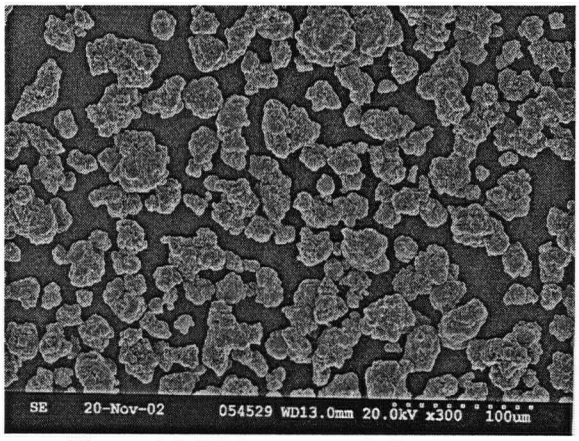

Figure 4.1 *SEM micrograph Co-AR*

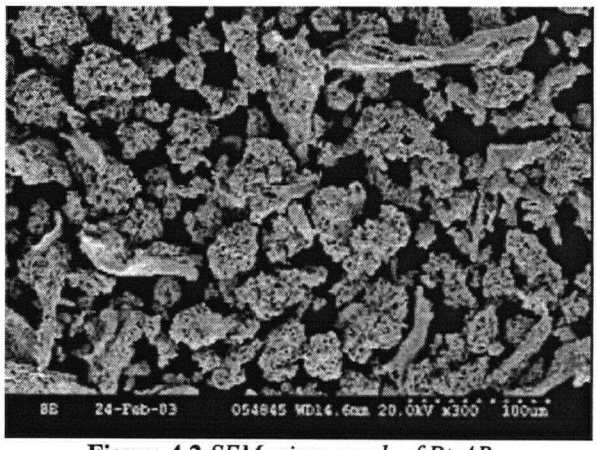

Figure 4.2 *SEM micrograph of Pt-AR*

The average particle sizes of Pt-AR and Co-AR were found to be 45μm and 40μm respectively. Figure 4.3 shows an XRD diffractogram of Co-AR. The XRD diffractogram of cobalt shows the presence of characteristic face centered cubic structure (FCC) at $2\theta = 44.21^{\circ}$ and hexagonal packed structure (HCP) at $2\theta = 47.56^{\circ}$. The PDF database indicates a peak at $2\theta = 44.21^{\circ}$ to be Co (111) and peaks at $2\theta = 47.56^{\circ}$ to be Co (101) respectively. The XRD diffractogram of Pt-AR (Figure 4.4) shows the presence of two characteristic peaks, Pt (111) at $2\theta = 39.72^{\circ}$ and Pt (200) at $2\theta = 46.24^{\circ}$. Platinum was found to have a single FCC.

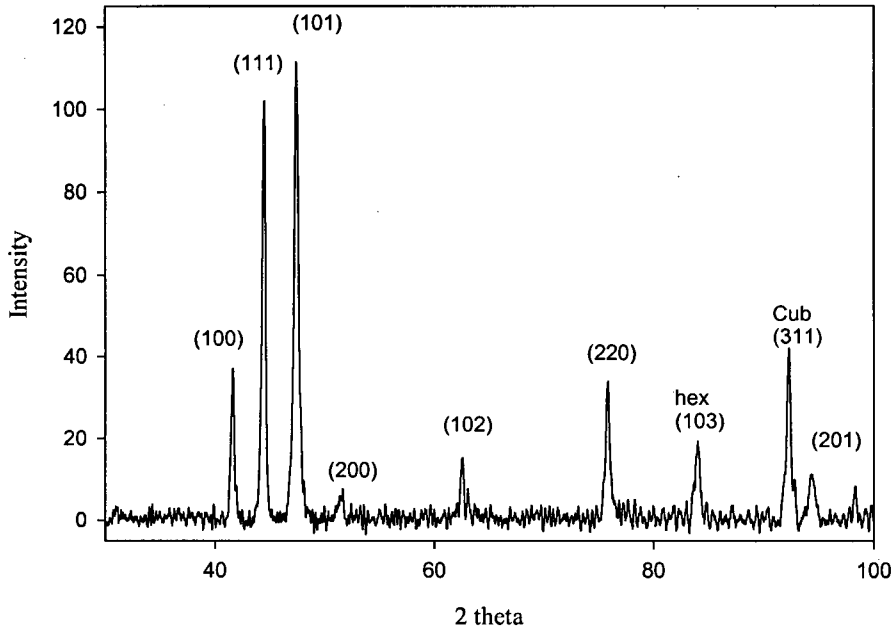

Figure 4.3 *XRD diffractogram of Co-AR*

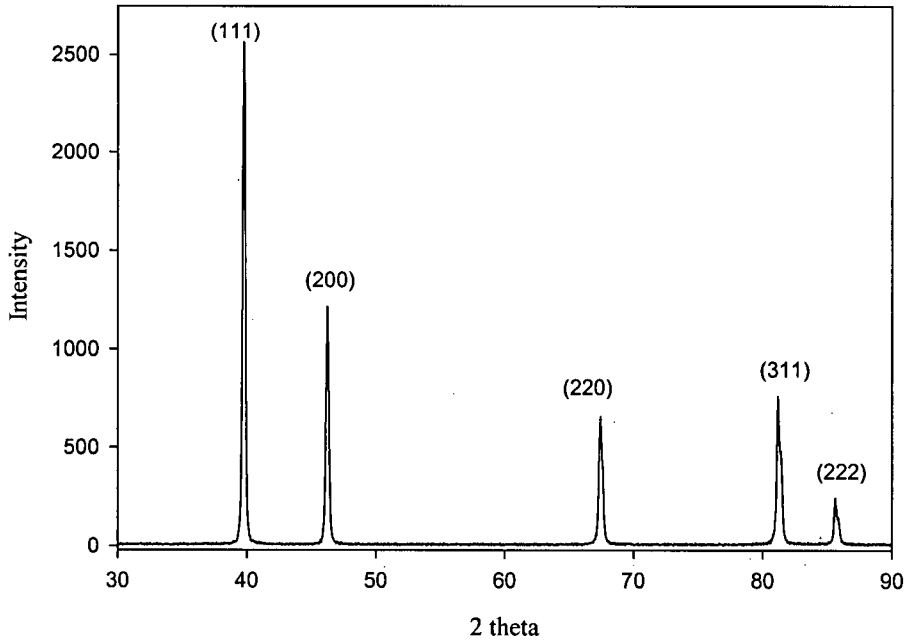

Figure 4.4 *XRD diffractogram of Pt-AR*

4.2 Optimization of ball milling parameters

Various cobalt and platinum systems were fabricated using high-energy ball milling by varying the ball milling parameters such as ball to powder weight ratio (BPR), process control agent (PCA) and milling time. The details of these systems are mentioned in Chapter 3. This section presents microstructural analysis of these systems done to determine the optimum ball milling parameters.

4.2.1 Co, Co-SA, Co-C based systems

4.2.1.1 Particle Size Analysis

Figures 4.5-4.16 show SEM and TEM micrographs of Co, Co/SA, Co/C alloy systems.

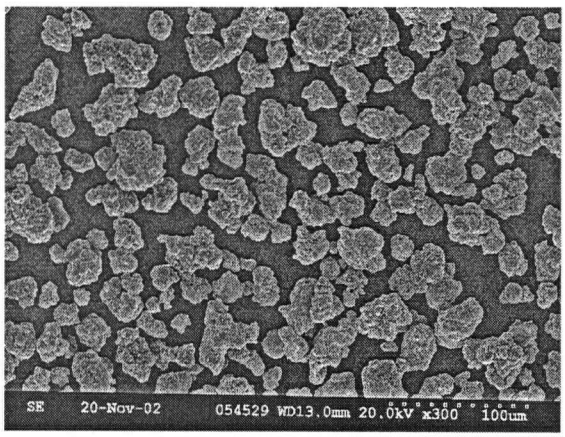

Figure 4.5 *SEM micrograph of Co-AR*

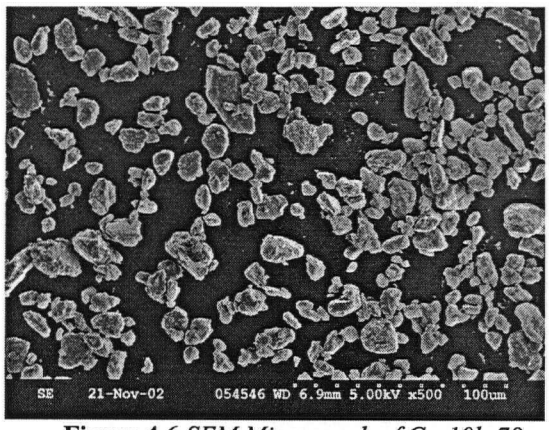

Figure 4.6 *SEM Micrograph of Co-10h-78*

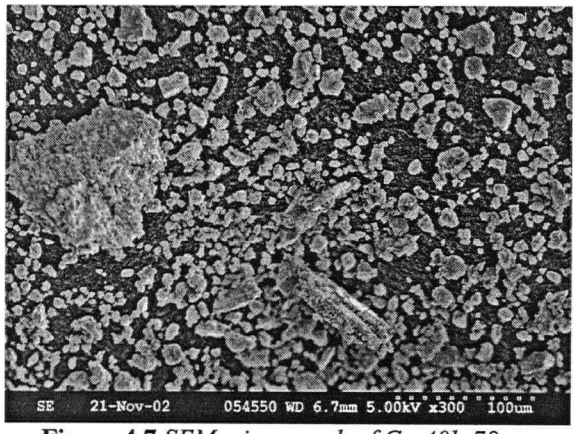

Figure 4.7 *SEM micrograph of Co-40h-78*

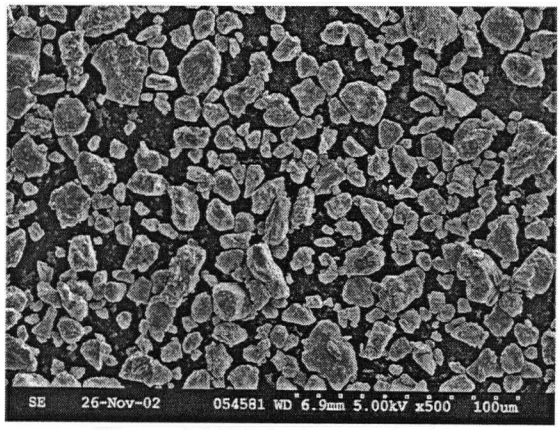

Figure 4.8 *SEM micrograph of Co-40h-39*

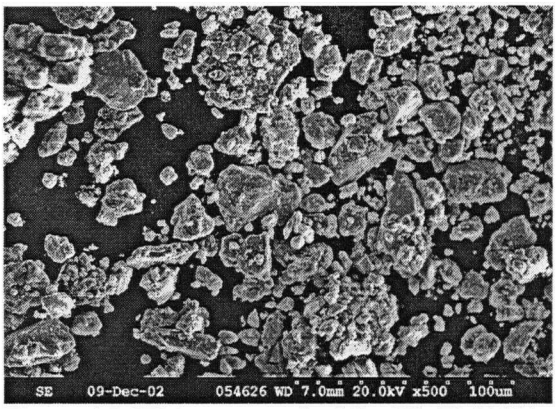

Figure 4.9 *SEM micrograph of Co-10h-78-2%SA*

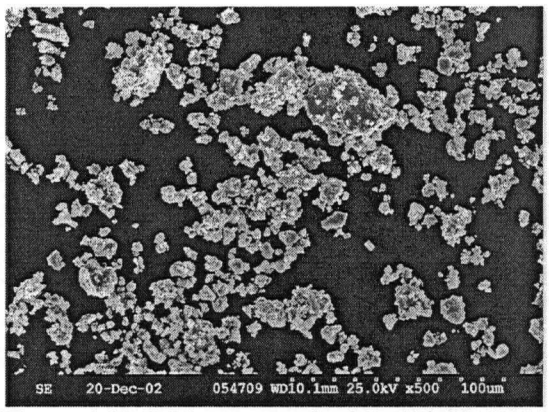

Figure 4.10 *SEM micrograph of Co-40h-78-2%SA*

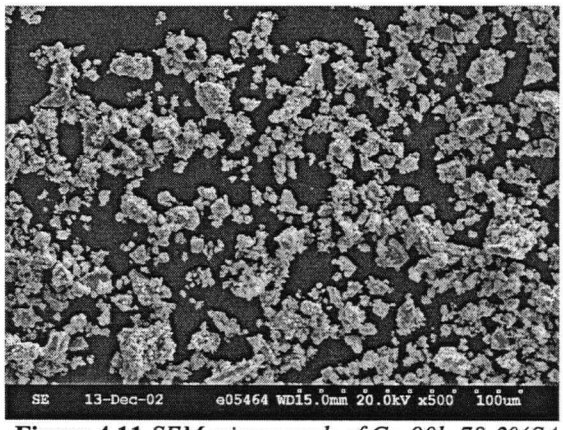

Figure 4.11 *SEM micrograph of Co-90h-78-2%SA*

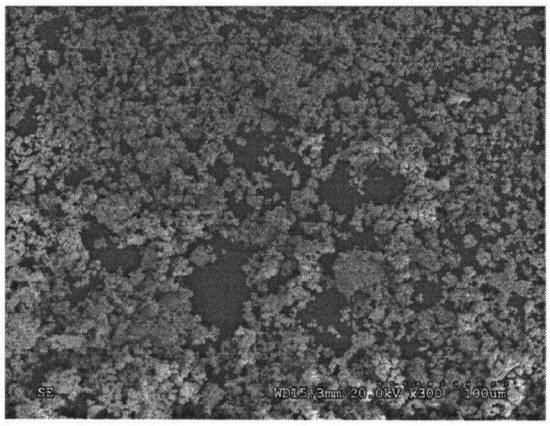

Figure 4.12 *SEM micrograph of Co-40h-78-20%SA*

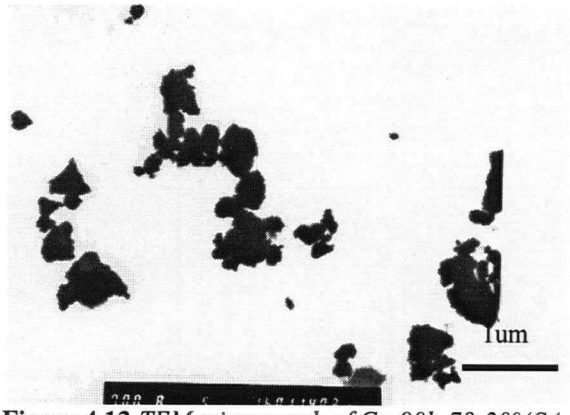

Figure 4.13 *TEM micrograph of Co-90h-78-20%SA*

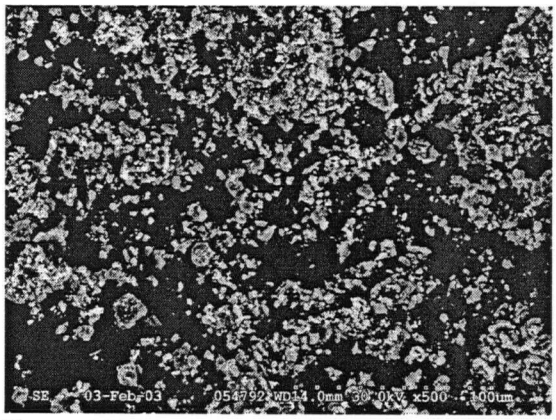

Figure 4.14 *SEM micrograph of Co-10h-78-20%C*

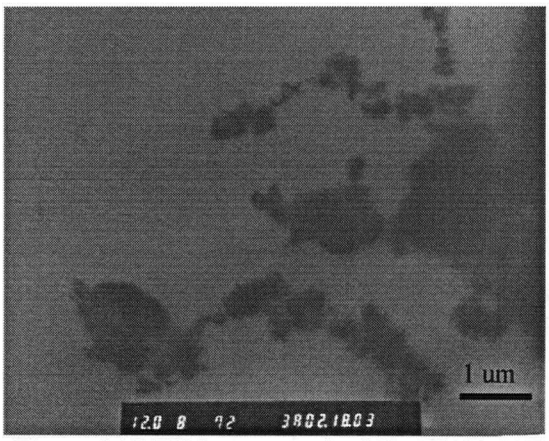

Figure 4.15 *TEM micrograph of Co-40h-78-20%C*

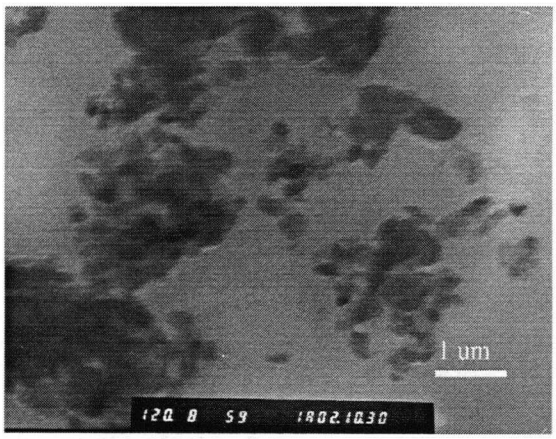

Figure 4.16 *TEM Micrograph of Co-90h-78-20%C*

The above figures show a decreasing trend in particle size with increasing milling time. The figures also show a finer particle size with the same milling time for mixtures of cobalt and PCA than for cobalt alone (Figures 4.7, 4.10, 4.12, 4.15). It is also clearly visible from the figures that carbon produces better particle refinement and dispersion than stearic acid (Figures 4.12 & 4.15 and Figs 4.13 & 4.16). The particle sizes were also examined using TEM. Figure 4.17 shows a plot of the average particle size vs. milling time obtained from TEM measurements on cobalt alloy systems. Particle sizes from both TEM and SEM were calculated assuming particles of spherical diameter. The plot shows that the smallest particle size obtained for Co-40h-78-20%C was 15nm as compared to 25–30nm for Co-40h-78-20%SA. The particle size of 6nm was achieved with 90hrs of milling but it at the same time produced lot of tungsten contamination due to attrition from the tungsten carbide (WC) crucible.

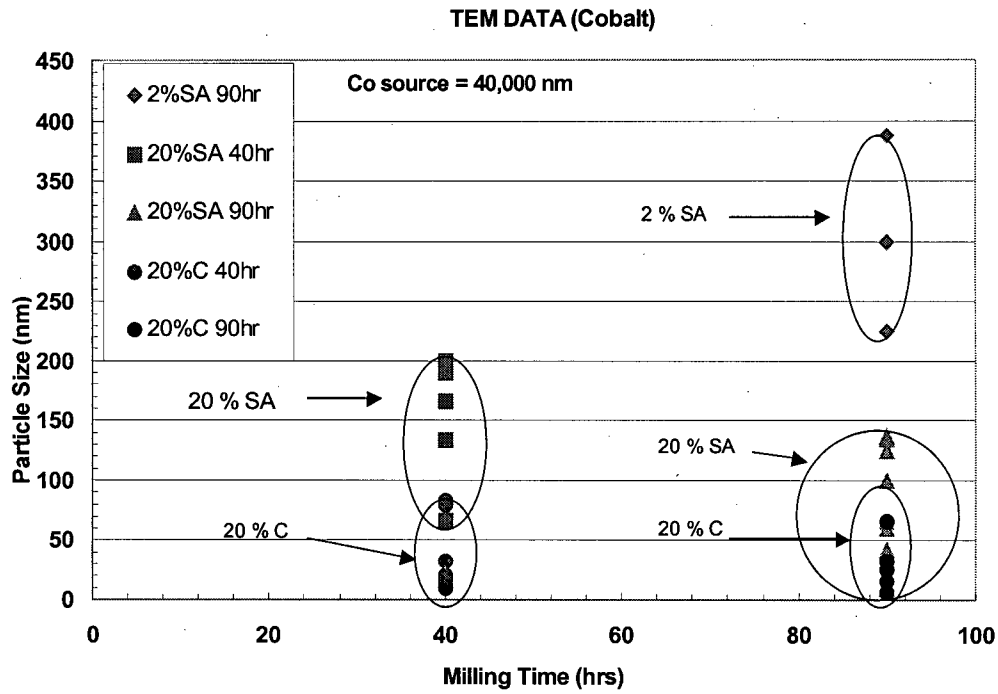

Figure 4.17 *TEM plot of particle size vs. milling time of Co-SA, Co-C systems*

From the above SEM figures and plot of TEM results, it was found that the maximum particle size refinement with minimum contamination for the Co alloy systems was obtained with a ball to powder ratio of 78:1 and 40 hours of milling with C as process control agent. Figure 4.18 shows diffraction pattern of Co-90h-78-20%SA and Figs. 4.19-4.20 show diffraction patterns of Co-90h-78-20%C. All the three samples show ring type patterns indicating the presence of very small size crystals. Diffraction patterns can only be obtained from specimens having thickness less than 50-100nm [Hunter,E.,E.,1993] and hence diffraction patterns could be obtained only from few samples.

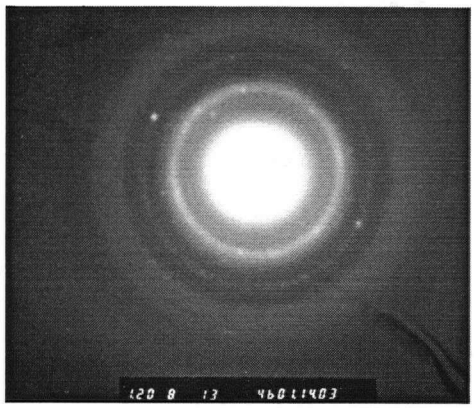

Figure 4.18 *Diffraction pattern of Co-90h-78-20%SA*

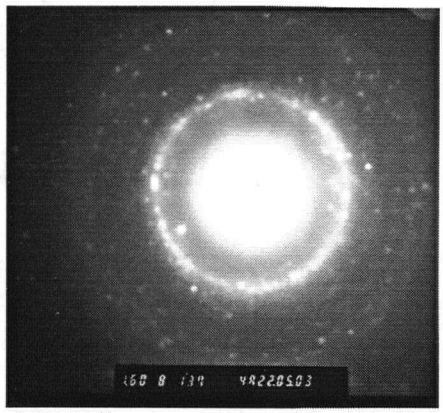

Figure 4.19 *Diffraction pattern of Co-90h-78-20%C*

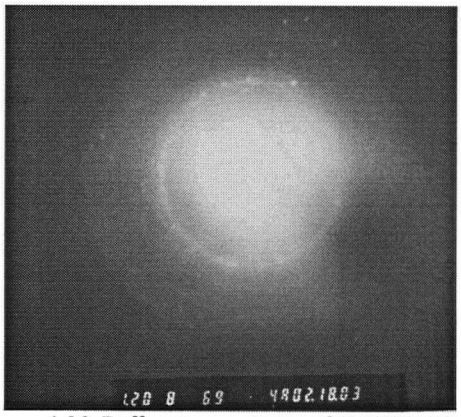

Figure 4.20 *Diffraction pattern of Co-90h-78-20%C*

4.2.1.2 Phase identification and solid-state reactions

This section gives the lattice parameters and various phases of the Co alloy systems obtained from X-ray diffractograms. Figure 4.21 shows x-ray diffractograms of Co-AR, Co-40h-78, Co-40h-78-20%SA, Co-40h-78-20%C

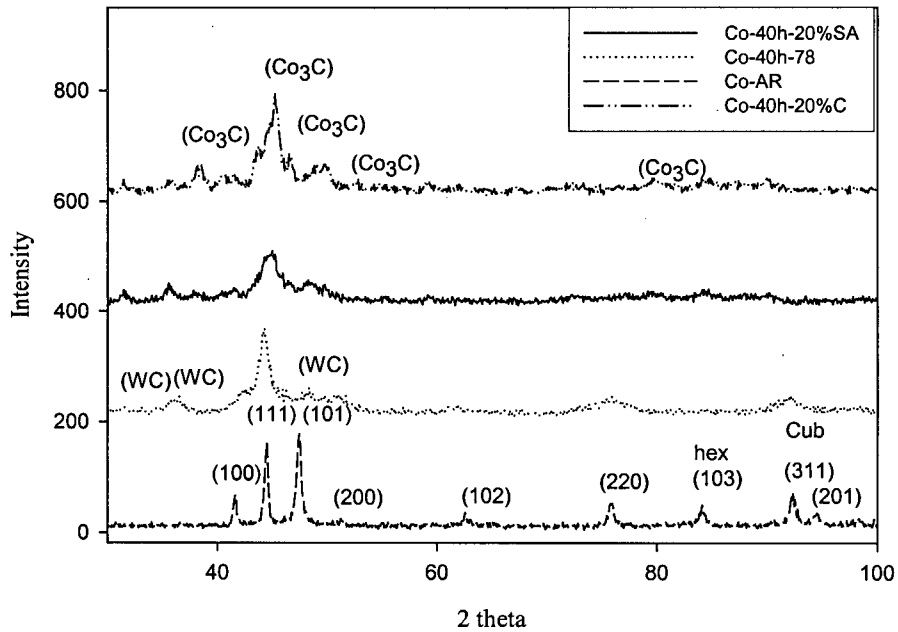

Figure 4.21 *XRD diffractogram of Co-AR, Co-40h-78, Co-40h-78-20%SA, Co-40h-78-20%C, each milled at the ball: powder ratio of 78:1.*

As explained in an earlier section (4.2), Co-AR shows the characteristic peaks of two cobalt structures, the cubic and the hexagonal packed structures. As the Co-AR is milled (40hrs), the cubic (111) peak broadens and shifts towards higher angles while the HCP (101) peak totally disappears leaving the face-centered as the only stable phase. This trend was noticed after half an hour of ball milling. Compared to Co-AR, Co-40h shows extensive line broadening due to microstrain and a decrease in particle size during the ball milling process. Though there was extensive broadening of the main FCC peak of Co with the increased milling time, the diffractogram also shows the presence of tungsten carbide. This tungsten carbide is due to the attrition of the tungsten carbide crucible. The following equation sums the reaction-taking place during ball milling for 40h:

$$\text{Co-AR} = \text{Co}_{\text{cub.}} + \text{Co}_{\text{hex.}} \xrightarrow{BM,\ 40hr} \text{Co}_{\text{cub.}} + \text{WC}_{\text{Wear}} \quad \ldots\ldots\ldots\ldots\ldots\ldots 4.1$$

In the diffractogram of Co-40h-78-20%SA, the strongest (111) Co peak further broadens and is shifted towards higher 2θ angles. It was also observed that the characteristic peaks of stearic acid located between 20° and 25° (2θ) vanish, suggesting the incorporation of stearic acid or its elemental components (C,H,O) into the Co lattice by formation of a solid solution (Co-SA(ss)). A small fraction of Co_3C was also detected indicating that a small fraction of cobalt reacts with carbon present in stearic acid to form cobalt carbide. The following equation sums up the reaction taking place between cobalt and stearic acid:

$$\text{Co-AR} + 20\%\ C_{18}H_{38}O_2 \xrightarrow{BM,\ 40hr} \text{Co-SA (ss)} + Co_3C + \downarrow WC_{Wear} \quad \ldots\ldots\ldots\ldots 4.2$$

The x-ray diffractogram for Co-40h-78-20%C showed a predominant formation of cobalt carbide (Co_3C) when Co-AR is mixed with 20 wt.% carbon and milled for 40hrs. No characteristic peaks of carbon were found. There was maximum broadening of the peaks with addition of carbon. This broadening of Co peaks together with shifting to higher 2θ angle is a clear indication that there is significant particle size refinement with carbon as a PCA. The characteristic peaks of FCC Co also partly overlapped with Co_3C suggesting that there is a minor formation of Co-C solid solution, Co-C(ss). Tungsten carbide peaks that were found in all Co systems after 40 hours of mechanical alloying are due to the attrition of tungsten carbide crucible and balls; however, as shown in the diffractograms of Co-40h-78-20%SA and Co-40h-78-20%C, the WC wear is reduced when a surface agent like stearic acid or carbon are added to the metal powder. The following reaction sums up the reaction taking place when mixture of cobalt and carbon is milled for 40h:

$$\text{Co-AR} + 20\%C \xrightarrow{BM,\ 40hr} Co_3C + \text{Co-C (ss)} + \downarrow WC_{Wear} \quad \ldots\ldots\ldots\ldots\ldots\ldots 4.3$$

4.2.1.3 Crystallite Size and Lattice Parameter Analysis

Table 4.1 presents lattice parameters, crystallite size and d-spacing of the Co alloy systems. There is a noticeable decrease in the crystallite size with surface agents. The smallest crystallites obtained are of 5 to 6nm. A ball to powder ratio of 78:1 showed better particle size refinement than a ratio of 39:1. Though, Co-AR shows both FCC and HCP structures, lattice parameters of HCP were more prominent. But interestingly, all the cobalt systems milled without surface agent and with stearic acid (Co/SA) show cubic structure. The lattice parameter of 3.545Å and d-spacing of 2.047Å of the milled Co alloy system show that cobalt has transformed into the β cobalt phase with FCC structure. These results are in good agreement with the literature [Kiros,Y.,1996a].

Table 4.1 *Table showing lattice parameter, d-spacing and crystallite size of Co alloy systems obtained from XRD*

Samples	Lattice Parameters (Å)	Angle	d- spacing (Å)	Structure	Crystallite Size (nm)
Co Source	2.503,2.503,4.061	47.57°	1.91	Hexagonal	45um
Co-10h-78	3.545,3.545,3.545	44.21°	2.047	Cubic	11.6nm
Co-40h-78	3.545,3.545,3.545	44.21°	2.047	Cubic	8.5nm
Co-40h-39	3.545,3.545,3.545	44.21°	2.047	Cubic	10.4nm
Co-40h-78-2%SA	3.545,3.545,3.545	44.21°	2.047	Cubic	7.3nm
C0-90h-78-2%SA	3.545,3.545,3.545	44.21°	2.047	Cubic	6.2nm
Co-40h-78-20%SA	3.545,3.545,3.545	44.21°	2.047	Cubic	5.2nm
C0-90h-78-20%SA	3.545,3.545,3.545	44.21°	2.047	Cubic	6.5nm
Co-10h-20%C	3.545,3.545,3.545 3.544.3.544,3.544	44.21° 45.38°	2.047 1.997	Cubic Orthorhombic	6.9nm
Co-40h-20%C	3.545,3.545,3.545 3.544.3.544,3.544	44.21° 45.38°	2.047 1.997	Cubic Orthorhomic	6.45nm
Co-90h-20%C	3.545,3.545,3.545 3.544.3.544,3.544	44.21° 45.38°	2.047 1.997	Cubic Orthorhomic	6nm

The lattice parameters of the Co/C alloy systems confirm formation of a large amount of cobalt carbide (Co_3C). This Co_3C shows an orthorhombic structure. The minor traces of unalloyed cobalt present show FCC structure with the standard lattice parameter and d-spacing.

As cobalt carbide peaks predominantly overlapped the cobalt peaks, the structure is assumed to be formed of crystals with lower lattice parameters. This shows that carbon decrease the interatomic distance of cobalt better than stearic acid.

4.2.1.4 Microstrain analysis

Figure 4.22 is a plot of microstrain vs. milling time for Co alloy systems. It was observed that microstrain increased with milling time and on adding surface agent. For example, the microstrain in cobalt increased to 0.0075 after 0.5 hr of milling and rises to 0.013 after 10 hrs of milling. Further milling does not increase microstrain values in the mechanically alloyed metal. Additionally, the results for microstrains that were induced in ball-milled cobalt with 2 wt.% and 20 wt.% SA for 40hrs and 90hrs are very similar too. A 10-fold higher amount of stearic acid does not lead to an increase of strain in the metal structure.

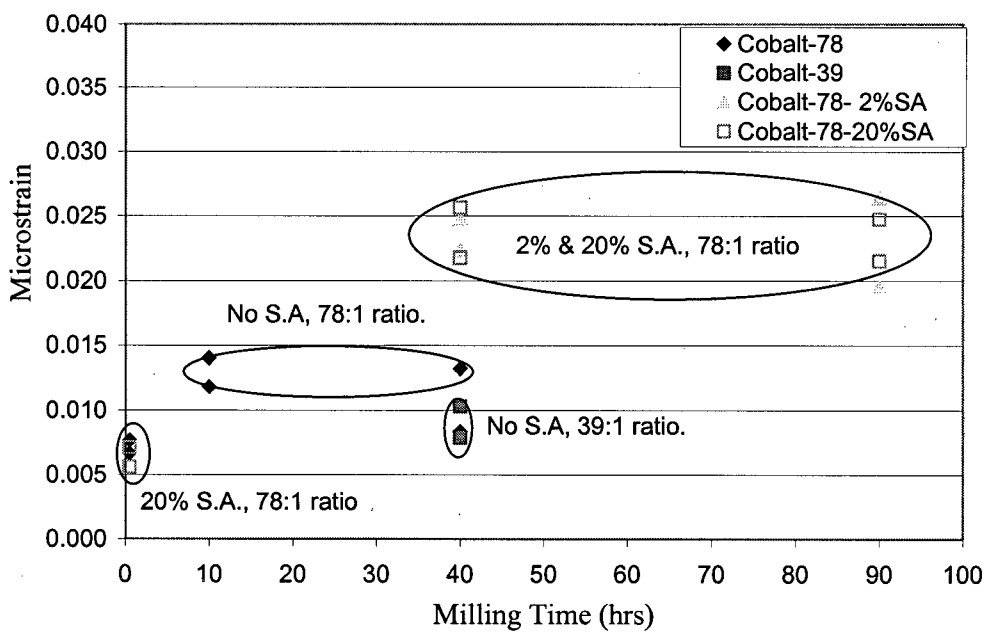

Figure 4.22 *Plot showing microstrain vs milling time obtained from XRD for Co alloy systems*

4.2.2 Pt/Pt-C Systems

Figures 4.23-4.24 are the SEM micrographs of Pt-AR, Pt-30min respectively. Figures 4.25- 4.26 are TEM micrographs of Pt-40h and Pt-40h-20%C respectively. All Pt, Pt/C systems were milled with ball to powder ratio of 78:1.

4.2.2.1 Particle Size Analysis

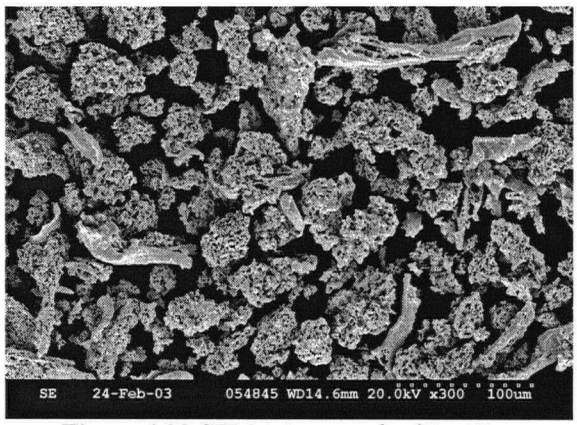

Figure 4.23 *SEM micrograph of Pt-AR*

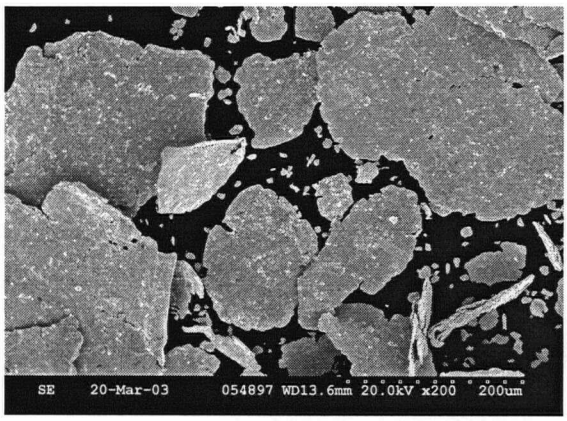

Figure 4.24 *SEM micrograph of Pt-30min*

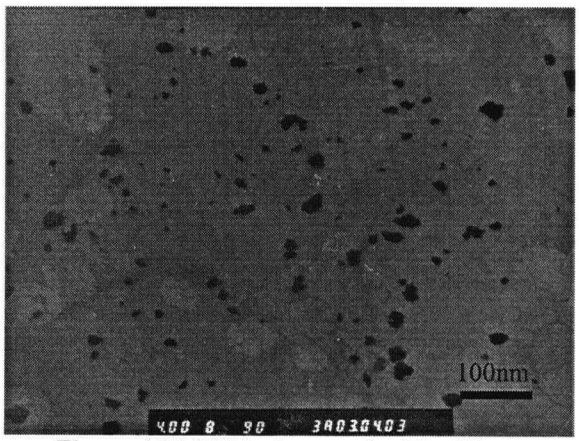

Figure 4.25 *TEM micrograph of Pt-40h*

Figure 4.26 *TEM micrograph of Pt-40h-20%C*

The micrographs show that particle size decreases as milling time increases. Fig 4.26 shows that particle size refinement is best with C as PCA.

Figures 4.27 and 4.28 show the TEM diffraction patterns of Pt-40h and Pt-40h-20%C respectively.

Figure 4.27 *Diffraction pattern of Pt-40h*

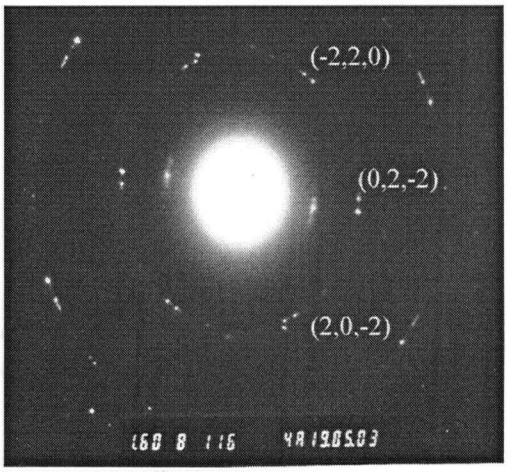

Figure 4.28 *Diffraction pattern of Pt-40h-20%C*

While Fig 4.27 show only faint diffraction rings, the diffraction pattern of Pt-40h-20%C (Fig. 4.28) shows both a ring type and dot type pattern. The dot patterns shows the presence FCC structure though planes did not match the standard elemental Pt planes.

4.2.2.2 Phase identification and Solid State Reactions

Figure 4.29 displays the XRD diffractograms of Pt-AR, Pt milled for 0.5h (Pt-30min) and Pt milled for 40hrs (Pt-40h). As explained in section 4.1, Pt-AR shows only FCC structure. However, after 40hrs of milling time, there is a visible WC peak arising from attrition of WC crucible and balls. The following reaction sums the reaction taking place when Pt is milled for 40hrs without carbon:

$$Pt \xrightarrow{BM,\ 40h} Pt + WC_{Wear} \qquad 4.4$$

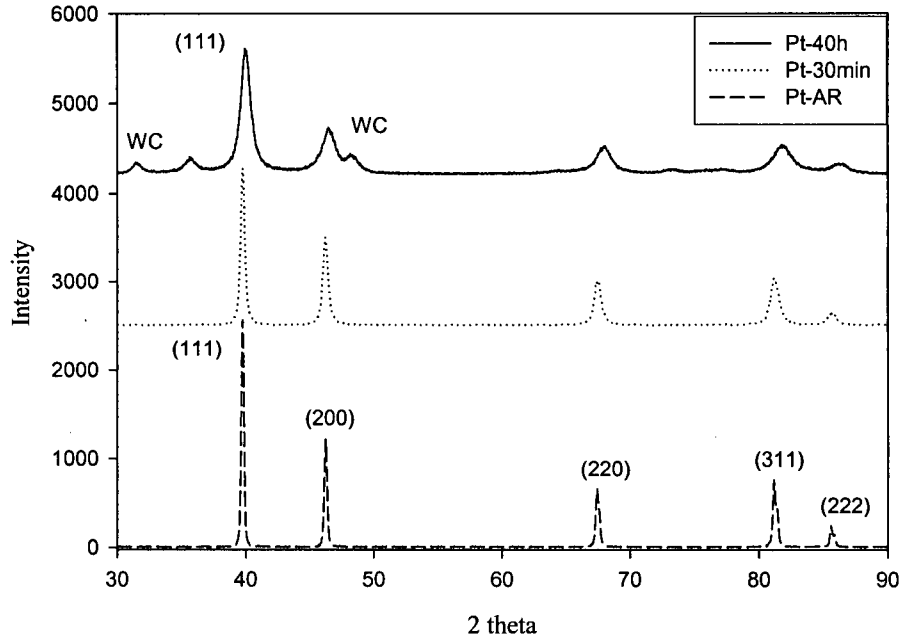

Figure 4.29 *XRD diffractograms of Pt-AR, Pt-30min, Pt-40h, each with BPR of 78:*1

Figure 4.30 shows the diffractograms of Pt-AR, Pt milled for 30minutes with 20%C (Pt-30min-20%C) and Pt milled for 40 hours with 20 wt% C (Pt-40h-20%C). Equation 4.5 gives the ball milling reaction:

$$\text{Pt} + 20\%\text{C} \xrightarrow{BM,0.5h,\ 40hr} \text{Pt-C(ss)} \quad \ldots\ldots 4.5$$

This diffractogram clearly indicated that there is more broadening i.e. better crystal size refinement when carbon is added.

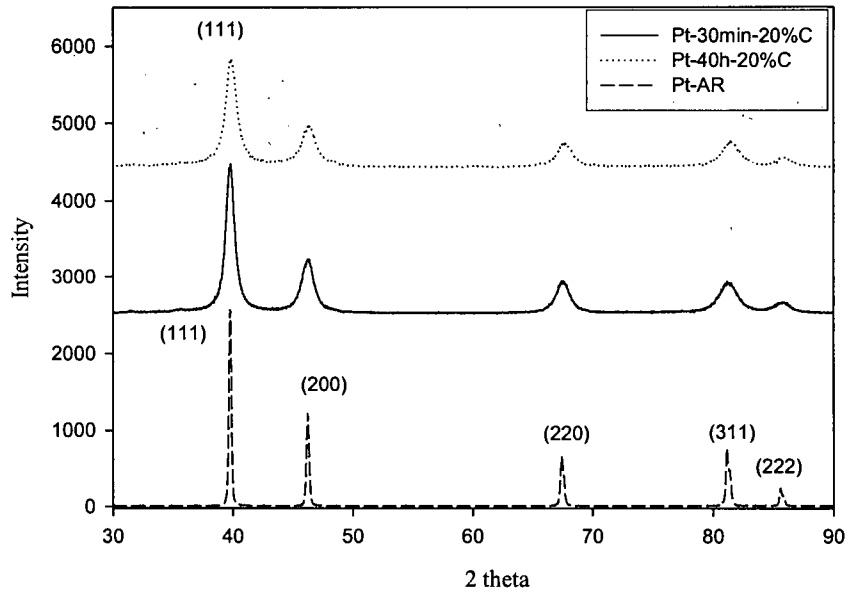

Figure 4.30 *XRD diffractograms of Pt-AR, Pt-30min-20%C,Pt-40h-20%C*

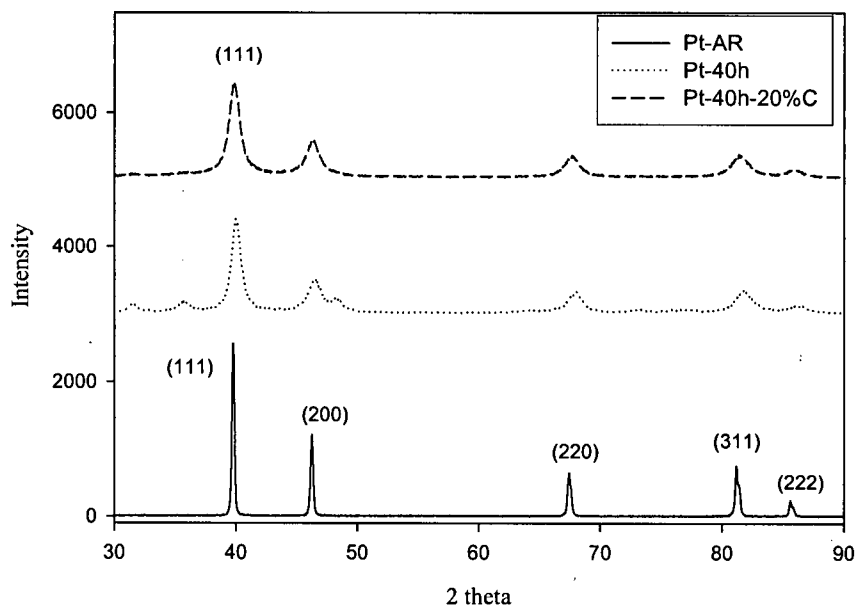

Figure 4.31 *XRD diffractograms of Pt-AR, Pt- 40h,Pt-40h-20%C*

Figure 4.31 shows the x-ray diffractogram of Pt-AR, Pt-40h and Pt-40h-20%C. From the above diffractogram patterns, it was observed that platinum, if ball milled for 40hrs without PCA, showed considerable WC attrition. However, Pt ball milled with carbon does not show any traces of tungsten carbide even after 40hrs milling suggesting that carbon not only reduces the agglomeration of the ball-milled powder but also acts as a good lubricant and suppresses tungsten carbide wear. Additionally, the lack of isolated carbon peaks in the x-ray diffractogram and the presence of broader FCC Pt peaks suggest that Pt and C form a solid solution Pt-C (ss) during their mechanical alloying.

4.2.2.3 Crystallite Size and Lattice Parameter Analysis

The change in crystallite size with the increase of ball-milling time was determined by analyzing the line broadening of the (111) Pt peak. As seen in Table 4.2 the average crystallite size of Pt powder reduces to 40nm after 30 min of ball milling and reaches the size of 10nm after 40hrs of milling. In comparison to ball-milled Pt-AR, the addition of C to Pt had an enormous effect on the crystallite size reduction. Only after 30min of milling time the average crystallite size drops to 10nm reaching the smallest value that has been achieved in the BM process for this short ball-milling time.

Table 4.2 *Table showing lattice parameter, d-spacing and crystallite size of Pt alloy systems obtained from XRD*

Samples	Lattice Parameters (Å)	Angle (Radians)	d- spacing (Å)	Structure	Crystallite Size (nm)
Pt source	3.878,3.878,3.878,	40.25	2.239	Cubic	45um
Pt-30min	3.9231,3.9231,3.9231	40.25	2.265	Cubic	40.3nm
Pt-30min-C20%	3.9231,3.9231,3.9231	40.25	2.265	Cubic	10.1nm
Pt-40-20%C	3.9231,3.9231,3.9231	40.25	2.265	Cubic	8.2 nm

Unlike the cobalt systems, lattice parameter and d spacing of Pt/C alloys increases on addition of carbon though the structure remains unchanged.

4.2.2.4. Microstrain analysis

Microstrains induced during BM for the Pt and Pt-C alloy systems are found to be lower than for the Co alloy system. The values of 0.005 and 0.01 were found for Pt-0.5h andPt-40h respectively. Microstrain values of ball-milled Pt-C system (0.012) were slightly higher than that of ball-milled Pt system (0.010). The mechanical impact on the crystal structure during BM and incorporation of carbon atoms into the Pt lattice structure are the most probable reasons.

4.2.3 Summary

From the above analysis of Co, Co/SA, Co/C, Pt, Pt/C alloy systems it was found that significant particle size refinement and dispersion were obtained with carbon as a surface agent, ball to powder ratio of 78:1 at milling time of 40hours. Microstrains values obtained were higher and better at the ball to powder ratio of 78:1 without addition of process control agents but particle refinement was inferior. Higher strain values result in more unstable crystals and higher activity. These optimized conditions were then used for the fabrication of PtCo and PtCo/C catalysts.

4.3 PtCo and PtCo/C alloy electrocatalysts

Using the above-mentioned ball milling conditions, various sets of catalysts were fabricated with different atomic percentages of platinum, cobalt and carbon.

4.3.1 Elemental Composition Analysis

Table 4.3 gives bulk atomic percentages of the catalysts detected by EDS. EDS has been used by several authors to find bulk atomic percentages of the material [Couturier, G.,1987]. Pt:Co atomic ratios of the fabricated catalyst 1 and 2 is 1:3 while that of catalyst 4 is 3:1.

Table 4.3 *Bulk Elemental analysis of the alloy electrocatalysts and commercial E-TEK catalysts by EDS*

SN	Sample/Compositions (at %)	Pt	Co	C	O	W	Cl
1	$Pt_{0.25}Co_{0.75}$-40h	0.78	2.32	83.08	10.32	0.26	-
2	$Pt_{0.25}Co_{0.75}$-40h-20%C-30min	1.05	3.10	83.17	0.07	0.37	-
3	PtCo-45h-1%C-5hrs	0.82	15.45	73.78	9.30	0.64	-
4	$Pt_{0.75}Co_{0.25}$-45h-1%C-5hr – Lixiviated	1.09	0.37	82.60	15.40	0.46	0.07
5	40%PtCo-ETek (1:1 a/o)	0.44	0.36	87.38	11.50	-	-
6	10%PtCo-ETek (1:1 a/o)	0.11	0.13	88.87	10.89	-	-

The percentages of carbon and oxygen are not very accurate as the catalyst samples were first fixed on carbon tape to provide a base for the EDS testing. The Pt:Co ratio of both commercial catalysts is 1:1 with noble/non-metal percentages 4 times higher in 40%PtCo-ETEK. Catalyst 3 (PtCo-45h-1%C-5h) has a much higher percentage of Co than Pt (Co:Pt~19:1); this was deliberately done because the same catalyst was then subjected to lixiviation, which dissolves large quantities of the cobalt. The visible traces of tungsten in fabricated catalysts are due to the attrition of tungsten carbide vial and balls. There is presence of trivial amount of Cl in the

lixiviated sample: it is from left over ions of HCl used for lixiviation of the catalyst. The quantitative results (Table 4.4) of the filtrate obtained by washing the lixiviated suspension showed that a significant amount of cobalt was leached and there was no trace of dissolution of platinum. The color of the filtrate was pink, which in itself is an indication of the dissolution of cobalt metal while lixiviation. The bulk Pt:Co atomic percentage of PtCo-45h-1%C-5hrs (Catalyst 3) before lixiviation is 0.053 which increases to 2.95 after lixiviation (Catalysts 4). This may be because metallic cobalt is easily converted into an oxide, and cobalt oxide species are readily soluble in the leaching solutions as the electronegativity of Co is very small (1.88eV). It is known that lower the electronegativity values the more readily the metal oxidizes. A similar effect is observed for Mo having electronegativity of 3.9eV by other authors [Gouerec,P.,2000]

Table 4.4 *Elemental composition of the filtrate obtained from lixiviation of electrocatalyst# 4 by IPL analysis*

Elements	**Co**	**W**	**Cl**
Composition (mg/l)	2372.53	4.7	10

4.3.2 Particle Size Analysis and Particle Dispersion

This section presents the particle size, particle dispersion and surface area measurements of the electrocatalysts.

Figures 4.32-4.37 show the particle size and dispersion of the catalysts analyzed by TEM. These figures reveal a far better dispersion of the lixiviated catalyst as compared to other fabricated alloys, however it is still not comparable with that of commercial catalysts.

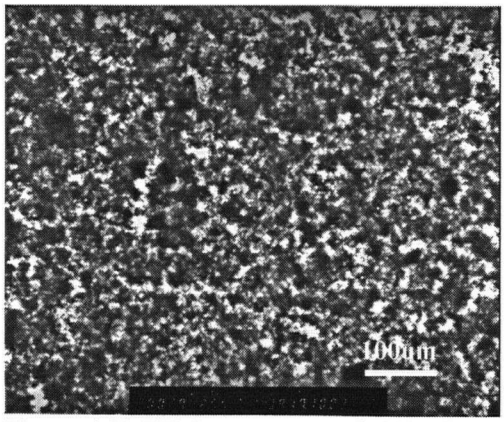

Figure 4.32 *TEM micrograms of 40%PtCo-ETEK*

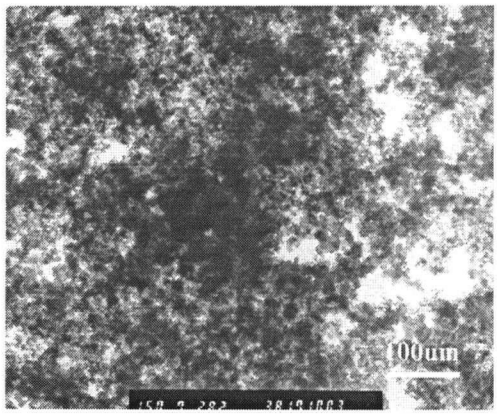

Figure 4.33 *TEM micrograms of 10%PtCo-ETEK*

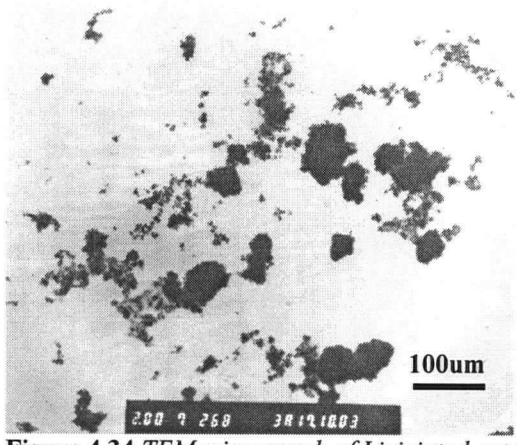

Figure 4.34 *TEM micrograph of Lixiviated catalysts*

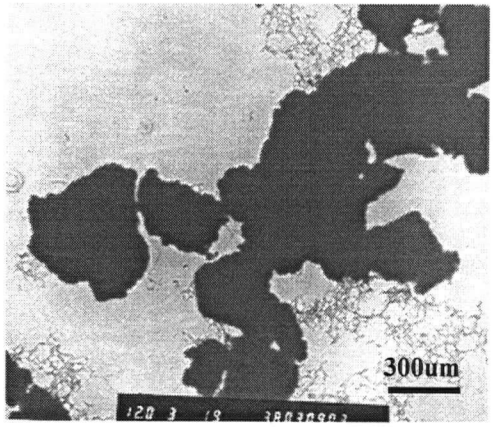

Figure 4.35 *TEM micrograph of PtCo-45-1%C-5hrs*

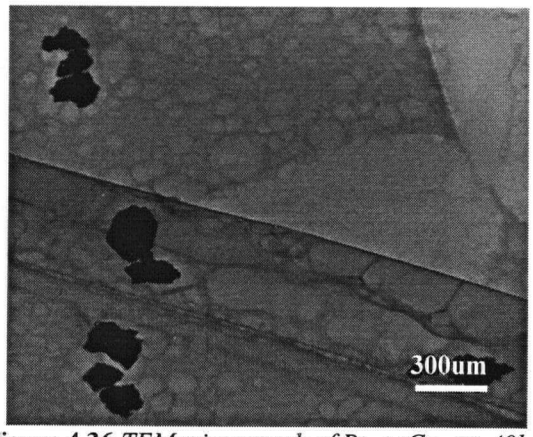

Figure 4.36 *TEM micrograph of* $Pt_{0.25}Co_{0.75}$*-40hr*

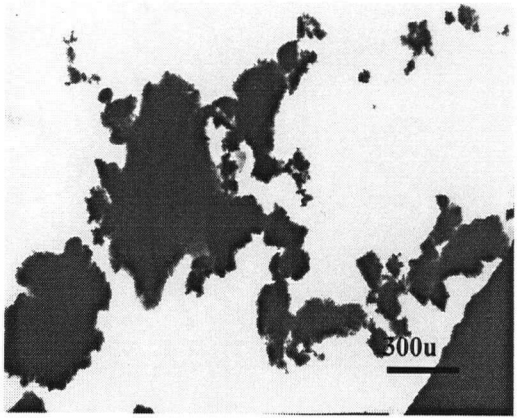

Figure 4.37 *TEM micrograph of* $Pt_{.25}Co_{.75}$*)-45hr-20%C-30min*

Table 4.5 presents the particle size of the catalysts obtained from TEM. The particle size of the lixiviated catalyst is one magnitude bigger than both commercial catalysts showing that ball milling followed by lixiviation has the potential of producing porous particles in the same range as produced by other fabrication method.

Table 4.5 *Particle sizes of PtCo electrocatalysts obtained by TEM*

S.No.	Sample	Particle Size (μm)
1	$Pt_{0.25}Co_{0.75}$-40hrs	300
2	$Pt_{0.25}Co_{0.75}$-40hrs-20%C-30min	100
3	PtCo-45hrs-1%C-5h	100
4	$Pt_{0.75}Co_{0.25}$-45hrs-1%C-5hrs– Lixiviated	33
5	40%PtCo-Etek (1:1 a/o)	0.33
6	10%PtCo-Etek (1:1 a/o)	0.33

Figures 4.38-4.41 give the diffraction patterns of $Pt_{0.25}Co_{0.75}$-40h-20%C-30min, 10%PtCo-ETEK, 40%PtCo-ETEK and lixiviated catalysts. All the catalysts are showing a ring type pattern that demonstrates that the catalysts are composed of nanocrystalline crystals.

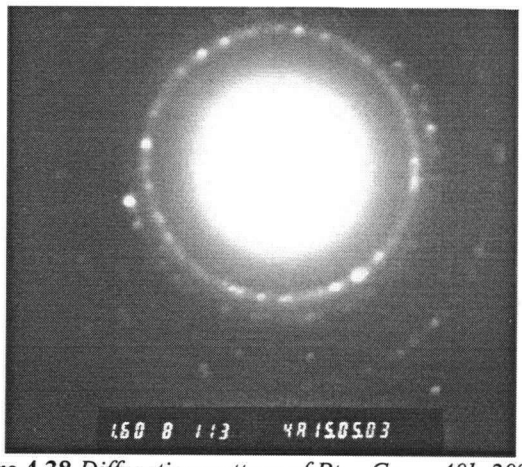

Figure 4.38 *Diffraction pattern of $Pt_{0.25}Co_{0.75}$-40h-20%C-30min*

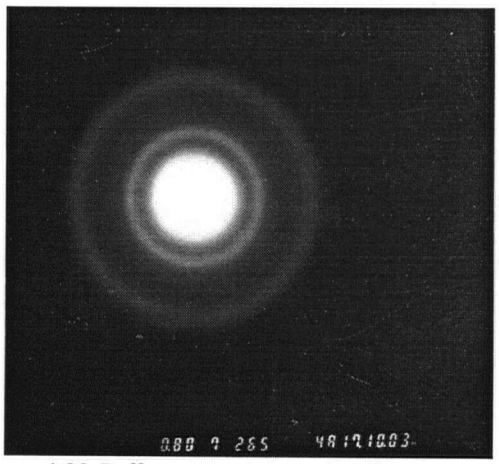

Figure 4.39 *Diffraction pattern of 10% PtCo-ETEK*

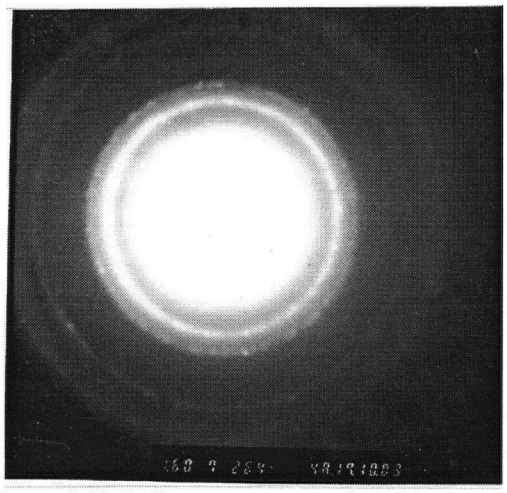

Figure 4.40 *Diffraction pattern of 40% PtCo-ETEK*

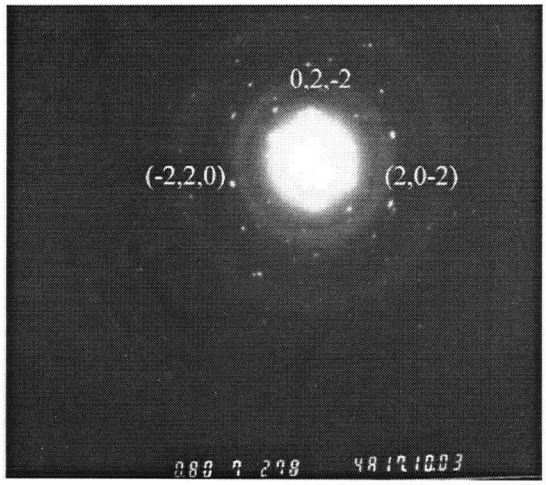

Figure 4.41 *Diffraction pattern of lixiviated catalyst*

Diffraction pattern obtained from nanocrystalline grains are generally ring type because diffraction pattern obtained by one grain overlaps another giving a continuous circle like pattern. Lixiviation catalyst also showed a dot pattern, it indicated the presence of FCC structure though the exact elemental identification could not be done.

4.3.3 Phase determination and Solid State reactions

The following reactions take place when platinum and cobalt powders are milled together for up to 40 hrs to obtain a Pt-Co alloy electrocatalysts.

$$Pt_{0.25} + Co_{0.75} \xrightarrow{BM,40hr} \text{Pt-Co(ss)} \quad \ldots\ldots 4.6$$

$$\text{Pt-Co}_{\text{BM 40hr}} + 20\%C \xrightarrow{BM,\ 5min,0.5hr} \text{Pt-Co-C(ss)} \quad \ldots\ldots 4.7$$

Figure 4.42 presents XRD diffractograms of $Pt_{0.25}Co_{0.75}$-40h, $Pt_{0.25}Co_{0.75}$-40h-20%C-5min, $Pt_{0.25}Co_{0.75}$-40h-20%C-30min. Diffractograms of all the catalysts do not show any characteristic diffraction peaks of pure Pt or Co metals. In $Pt_{0.25}Co_{0.75}$-40h, the main peaks are found at higher angles of $2\theta = 40.96^\circ$ and 47.8° respectively.

These shifted diffraction peaks of the new Pt-Co catalysts, which were found to be located between the characteristic angles of Pt and Co suggested that a Pt-Co phase was formed due to alloying. Low intensity peaks at $2\theta = 36^{\circ}$ and 61.7° after 40 hrs of milling could not be identified. Diffraction peaks originated from WC are not visible in the plots suggesting that attrition of the WC crucible and balls was minimal in this system.

In the diffractograms of $Pt_{0.25}Co_{0.75}$-40h-20%C-5min, $Pt_{0.25}Co_{0.75}$-40h-20%C-30min, the characteristic broad carbon peak found at 28° (2θ) disappeared soon after 5 minutes of milling. Furthermore, there was no significant difference between $Pt_{0.25}Co_{0.75}$-40h and $Pt_{0.25}Co_{0.75}$-40h-20%C-5min. However, after 30 minutes of mechanical alloying with carbon, the peaks not only become asymmetrical and much broader suggesting a decrease in size of the crystals but also they shift further to higher 2θ values indicating a decrease of cell parameters of the unit cell.

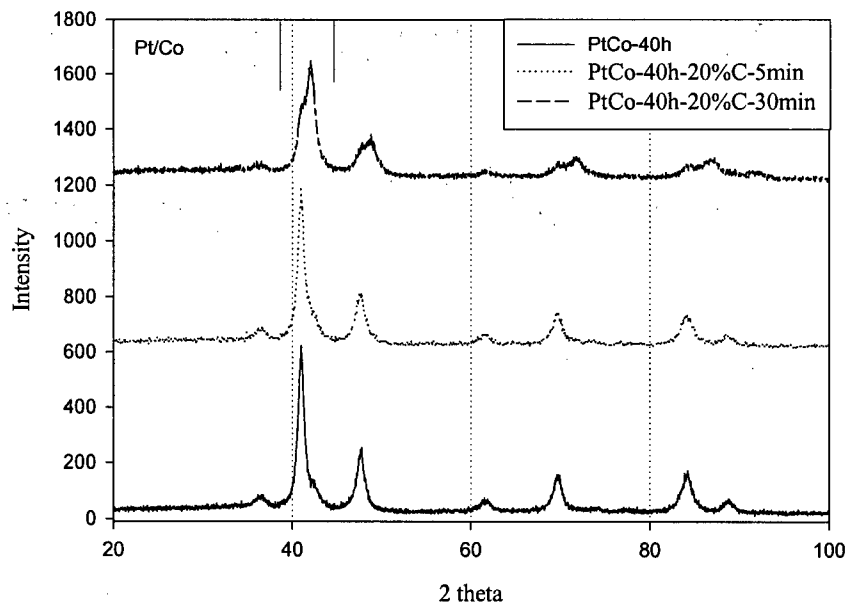

Figure 4.42 *XRD diffractograms of $Pt_{0.25}Co_{0.75}$-40h, $Pt_{0.25}Co_{0.75}$-40h-20%C-5min, $Pt_{0.25}Co_{0.75}$-40h-20%C-30min*

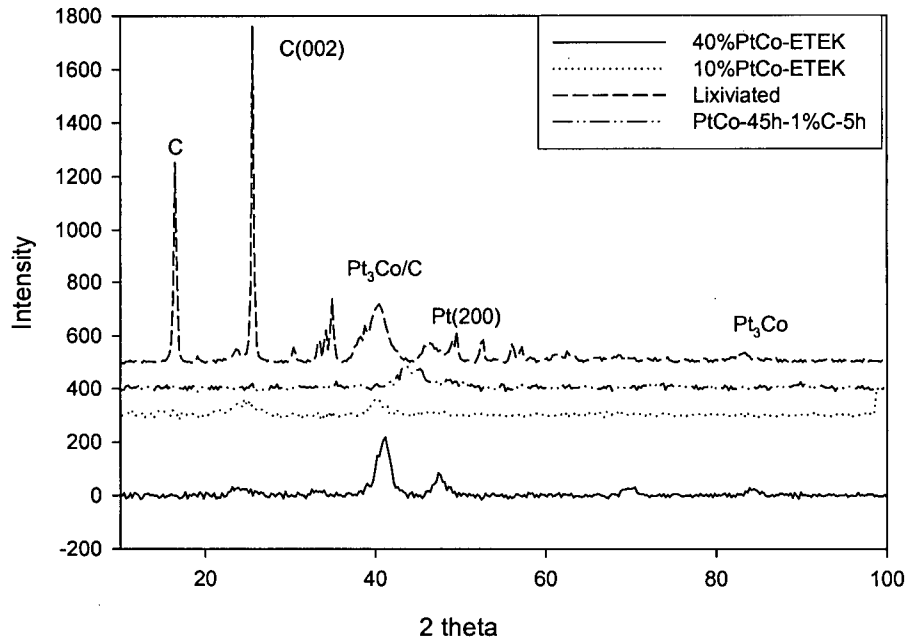

Figure 4.43 *XRD diffractogram of PtCo-45h-1%C-5h, lixiviated catalyst, 10%PtCo-ETEK, 40%PtCo-ETEK*

The peaks were found at $2\theta = 42.16^{\circ}$ and 49.08° respectively in $Pt_{0.25}Co_{0.75}$-40h-20%C-30min.There was no carbide formation in Pt-Co-C system. As mentioned earlier, cobalt has a strong tendency to form carbides, especially Co_3C, when carbon black or stearic acid has been added to the ball-milling process. Therefore carbide formation was controlled in the Pt-Co-C(ss) system.

Figure 4.43 shows diffractograms of PtCo-45h-1%C-5hrs, lixiviated catalysts and both the commercial catalysts. The following equations summarize the reaction-taking place in the formation of the three catalysts;

$$Pt + Co \xrightarrow{BM,40hr} PtCo(ss) \quad \ldots\ldots 4.8$$

$$PtCo + 1\%C \xrightarrow{BM,5hr} Pt\text{-}Co\text{-}C(ss) + Co \ldots \quad \ldots\ldots 4.9$$

$$Pt\text{-}Co\text{-}C \xrightarrow{lixiviated} Pt + Co + C + Pt_3Co(ss) \ldots\ldots 4.10$$

The diffractogram of PtCo-45h-1%C-5hrs shows no two individual peaks of PtCo alloy. The peaks also show a strong indication towards the presence of metallic cobalt with small amounts of PtCo alloy formation. This is most probably because the amount of cobalt in this alloy is ~19 times more than Pt and hence there were very few Pt sites are available for alloying. PtCo forms a ternary alloy, PtCo/C, on addition of carbon. The diffractogram of the lixiviated c atalyst i s totally different from the other fabricated electrocatalysts. It shows pure C peak, HCP (002) at 2θ=25°, having almost the same peak positions as characteristic XC-Vulcan carbon. Also, the Pt_3Co/C alloy peak is at higher angle of 40.9° indicating alloying. This peak is broader than any main peak of fabricated and commercial catalysts indicating a significant decrease in the size of the crystals. A slight bump in the same peak indicates the presence of metallic cobalt. This showed that some amount of metallic cobalt was present even after lixiviation. There is also presence of unalloyed Pt in the diffractogram. The presence of carbon (002) is found also in the commercial catalyst but it is highly broadened. This shift of Pt (111) to higher angles indicates a decrease in the unit cell dimension caused by the substitution of Pt atoms in the cobalt lattice. Such shift due to alloying has also been reported previously [Denis,M.,C.,1998]. Also, another peak associated with Pt (200) plane at 2θ = 47.6° is shifted to higher angles in all the catalysts. Both the Pt (111) and (200) peaks in all the fabricated catalysts are highly broadened suggesting that there is a considerable decrease in the particle size due to ball milling. As discussed above, microstrain in the samples very likely induced some broadening which is quite common in ball milling fabrication. This broadening due to microstrain is also desirable as it provides unstable and active surfaces prerequisite for improved electrolysis. There are some peaks of WC due to the attrition of tungsten vial and balls.

4.3.4. Crystallite Size and Lattice Parameter Analysis

Table 4.6 reports the crystallite size of the catalysts calculated from the main Pt (111) diffraction peak using the Scherer equation as explained in the experimental section. The crystallite size of lixiviated catalysts is smaller than that of 40%PtCo-ETEK and the same as 10%PtCo-ETEK. The higher crystallite size of 40%PtCo-ETEK shows that as the metal content increase the crystal and particle sizes increase.

Table 4.6 *The lattice parameter, d-spacing and crystallite size of PtCo alloy electrocatalysts obtained by XRD*

Samples	Lattice Parameters (Å)	Angle (Radians)	d- spacing (Å)	Structure	Crystallite Size (nm)
10%PtCo-ETEK	3.854,3854,3.854	40.53	2.224	Cubic	7
40%PtCo-ETEK	2.682,2.682,3.675	41.66	2.166	Tetragonal	9
$Pt_{0.25}Co_{0.75}$-40h	3.803,3.803,3.701	41.46	2.176	Tetragonal	36
$Pt_{0.25}Co_{0.75}$-40h-20%C-30min	3.803,3.803,3.701	41.46	2.176	Tetragonal	9.34
PtCo-45h-1%C-5h	3.803,3.803,3.701	41.46	2.176	Tetragonal	10
Lixiviated catalyst	3.854,3854,3.854	40.53	2.224	Cubic	7

It can be seen from the Table 4.6 that the lattice parameters of all the catalysts are smaller than that of Pt-AR (3.878 Å) and Pt-C system (3.923 Å). This shows that Pt-Pt nearest neighboring distance decreases on addition of cobalt. All the fabricated catalysts except lixiviated catalysts have tetragonal structure. This result fully matches with the phase diagram which shows that tetragonal structured CoPt phase is formed when Pt: Co is mixed is the ratio of 60-76: 24:40 at.%. The lixiviated catalyst has $CoPt_3$ phase which is cubic in nature. The cubic nature of the $CoPt_3$ phase is confirmed by the phase diagram but the Pt content at which this phase is reported to form in phase diagram is 75-90 at.% while lixiviated catalyst contains Pt content of only 25 at. %. This shows that ball milling is capable of alloying elements beyond solubility limit and thus overcomes limitations imposed by phase diagram.

A few catalysts were subjected to surface area analysis by BET. It was found that Pt-30min has a surface area of $0.01m^2/g$ and that of Pt-40h and Pt-40h-20%C have surface areas of $0.36m^2/g$ and $8.5m^2/g$ respectively. It should be noted that 1mg of each catalysts was used which is less than what is usually required for BET analysis. The surface areas of the rest of the electrocatalysts were calculated using the formula given below:

$$S=6/(\rho*d)$$

Where, S is the surface area, ρ is the density and d is the diameter of the 'crystals'. There is great ambiguity in the literature regarding the use of crystalline size and particle size. Many of the earlier literature using particle size to calculate the surface area have actually used 'crystallite size' for the so-called 'particle size' [Kiros,Y.,1996a]. By definition, a 'particle' is agglomerates of crystals whereas crystal is an individual smallest identity having specific unit cell. The above formula hold good only for crystallite size and not for particle size as the crystalline size is usually smaller than particle size by an order of 10^3m. The presence of other elements like tungsten has not been considered while calculating the surface area as it is a sheer impurity (refer Appendix B).

Table 4.7 *Surface area analysis by crystallite size*

Samples	Crystallite Size (nm)	Surface Area (m^2/g)
10%PtCo-ETEK	7	52.488
40%PtCo-ETEK	9	45.3
$Pt_{0.25}Co_{0.75}$-40h	36	10.75
$Pt_{0.25}Co_{0.75}$-40h-20%C-30min	18.6	20.28
PtCo-45h-1%C-5h	10	5.6
Lixiviated catalyst	7	42.847

Surface area analysis is highly advantageous in understanding the electrochemical behavior of catalysts. It will be dealt with in more detail in section 4.3.6.

4.3.5 Surface Oxide and Surface elemental determination

All catalysts were evaluated by XPS analysis to determine the elemental composition and oxide formed during ball milling. Figures 4.44-4.48 give the broad scans of Pt-AR, 40%PtCo-ETEK, $Pt_{0.25}Co_{0.75}$-40h, PtCo-45h-1%C-5h, $Pt_{0.75}Co_{0.25}$-45h-1%C-5h–lixiviated catalysts respectively.

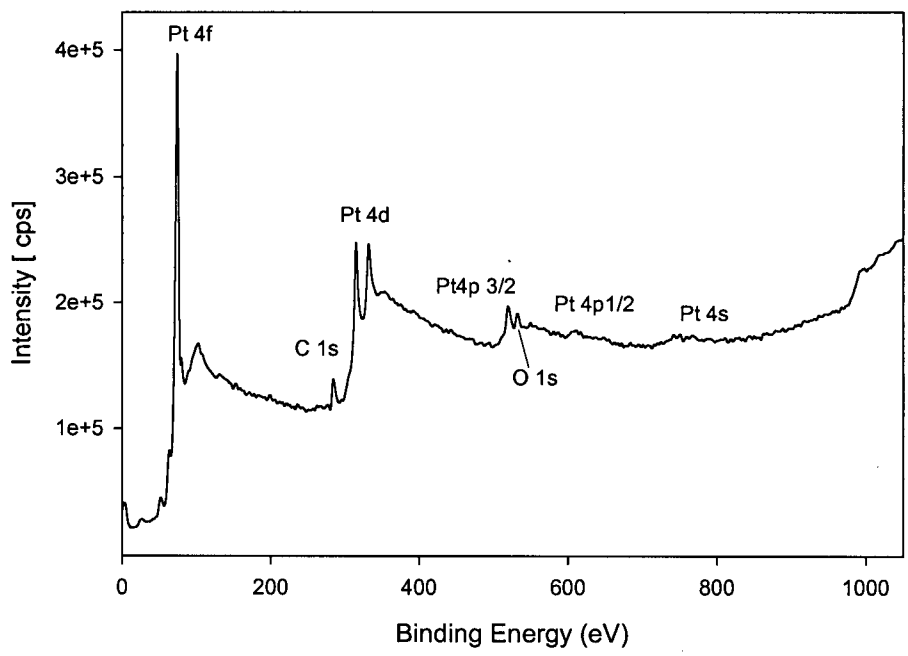

Figure 4.44 *Broad scan of Pt-AR obtained by XPS analysis*

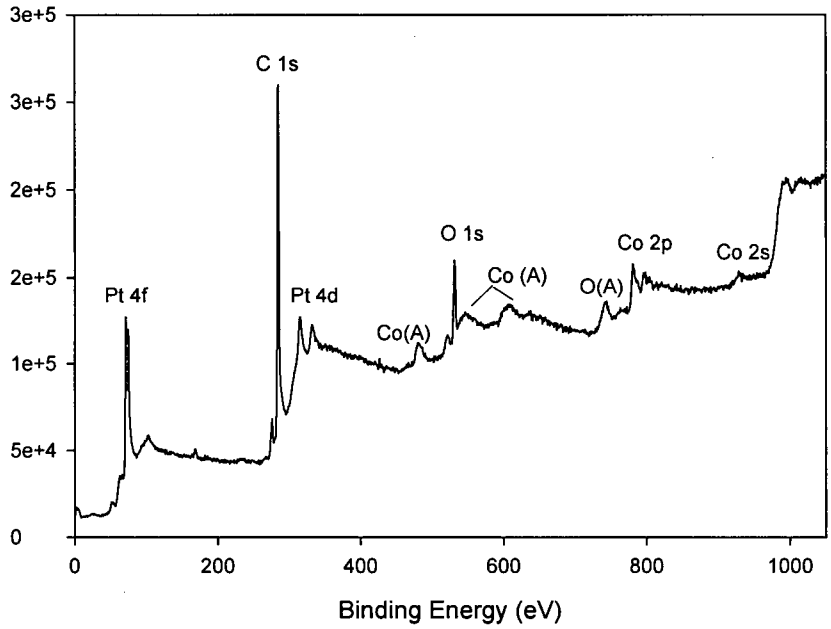

Figure 4.45 *Broad scan of 40%PtCo-ETEK obtained by XPS analysis*

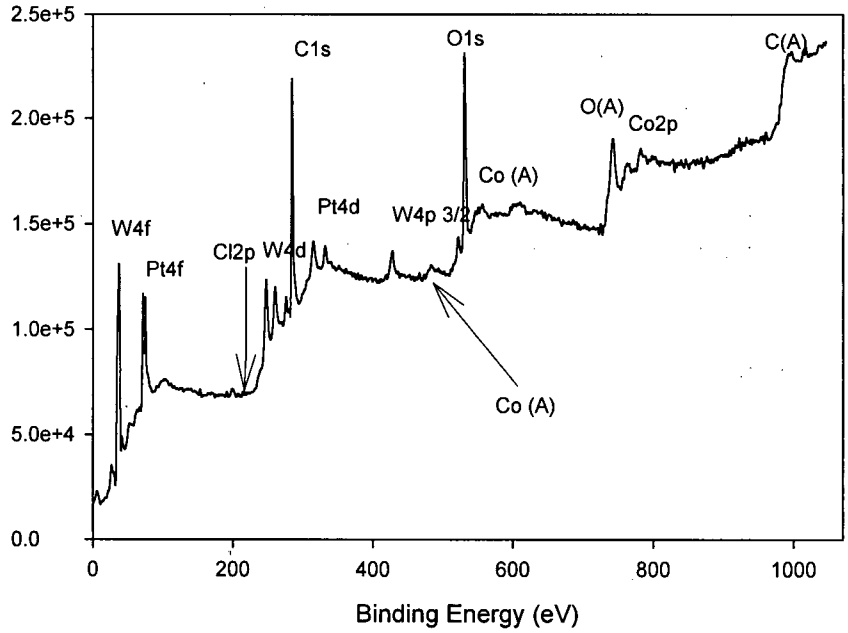

Figure 4.46 *Broad scan of lixiviated catalyst obtained by XPS analysis*

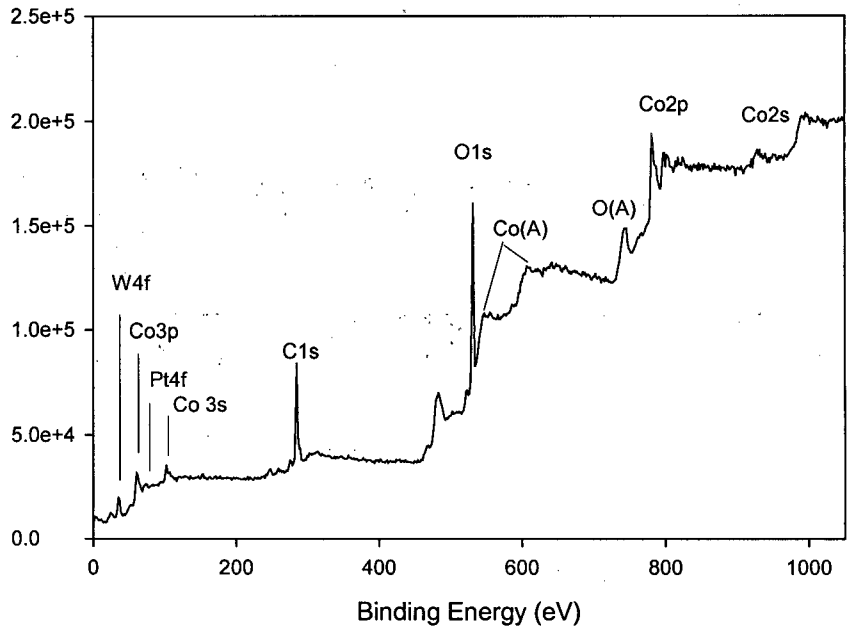

Figure 4.47 *Broad scan of $Pt_{0.25}Co_{0.75}$-40h obtained from XPS analysis*

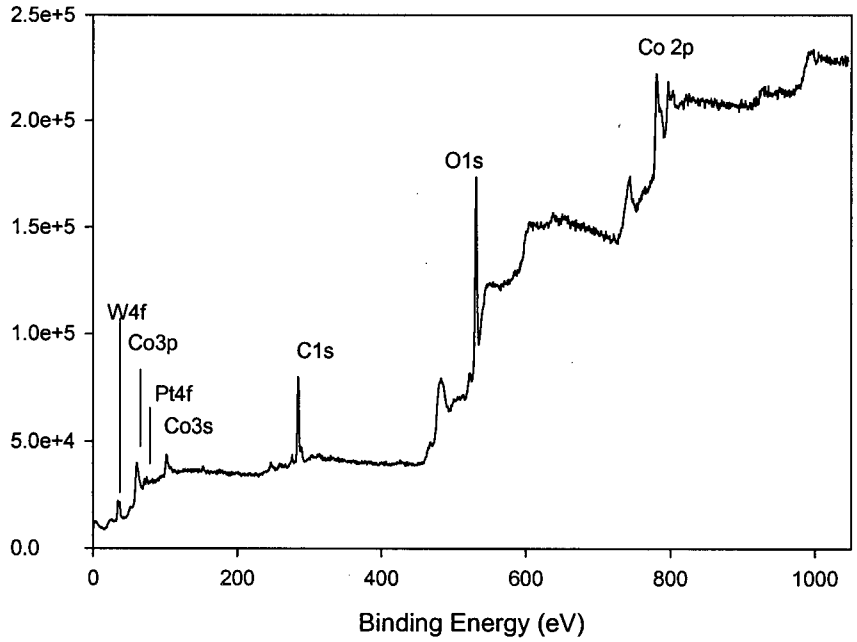

Figure 4.48 *Broad Scan of PtCo-45h-1%C-5h obtained from XPS analysis*

The surface elemental composition obtained by XPS is given in Tab 4.8.

Table 4.8 *Elemental composition of various catalysts obtained from XPS analysis*

Sample/Compositions (at %)	Pt	Co	C	O	W	Cl
Pt as received (Alfa Aesar)	36.5	-	54.1	9.4	-	-
$Pt_{0.25}Co_{0.75}$-40h	0.2	10	47	41.9	0.9	-
PtCo-45hrs-1%C-5h	0.3	8.5	53.6	36.9	0.8	-
$Pt_{0.75}Co_{0.25}$-45h-1%C-5h – Lixiviated	2.7	1.2	63.9	26.6	5.6	-
40%PtCo-ETEK	3.6	2.6	84.2	9.5	-	-

XPS analysis of lixiviated catalyst shows a small peak of Cl2p. The amount of Cl could not be quantified. This trivial amount would not be a reason for any increase or decrease in activity of the lixiviated catalyst.

Figures 4.49(a-b) represent the narrow scans of the Pt4f core levels peaks of the following catalyst powders: $Pt_{0.25}$:$Co_{0.75}$-40h, Pt:Co-45h-%C-5hr, $Pt_{0.75}Co_{0.25}$-45h-1%C-5h-lixiviated. For the sake of comparison, equivalent spectra's of Pt-AR and one of the commercial catalyst, 40%PtCo-ETEK, are also shown.

The Pt 4f XPS spectrum of Pt-AR is characteristic of the Pt element. The Pt 4f7/2 peaks and Pt 4f5/2 peaks are at 70.9 and 74.3eV respectively. There is a difference of 3.30eV gap between the Pt 4f5/2 and Pt 4f7/2 peaks that is very close to the standard gap of 3.35eV. This data matches perfectly with elemental Pt^{o} [Gouerec,P.,2000; Wagner,C.,D.,1979]. There is a marked difference in the binding energy of the Pt 4f5/2 and Pt 4f7/2 peaks of the Pt-AR and the alloy catalysts fabricated. A shift of 0.5eV is seen in the binding energies of both the Pt4f core level peaks of the 40%PtCo- ETEK catalyst. This is indeed confirmed by its XRD diffractogram where the Pt (111) peak is shifted towards higher 2θ values. This trend in the change in binding energy in

the 40%PtCo-ETEK and the lixiviated sample is very similar. The binding energy of the Pt 4f7/2 peak of 40%PtCo- ETEK is only 0.2eV higher than the lixiviated catalyst. This shift in the core 4f level is a result of the alloying of Pt and Co. A similar shift in higher binding energies has been reported in the literature when Pt is alloyed with Ru [Denis, M.,C.,2000]. This again confirms that there is some Pt and Co solid solution formation/alloying taking place.

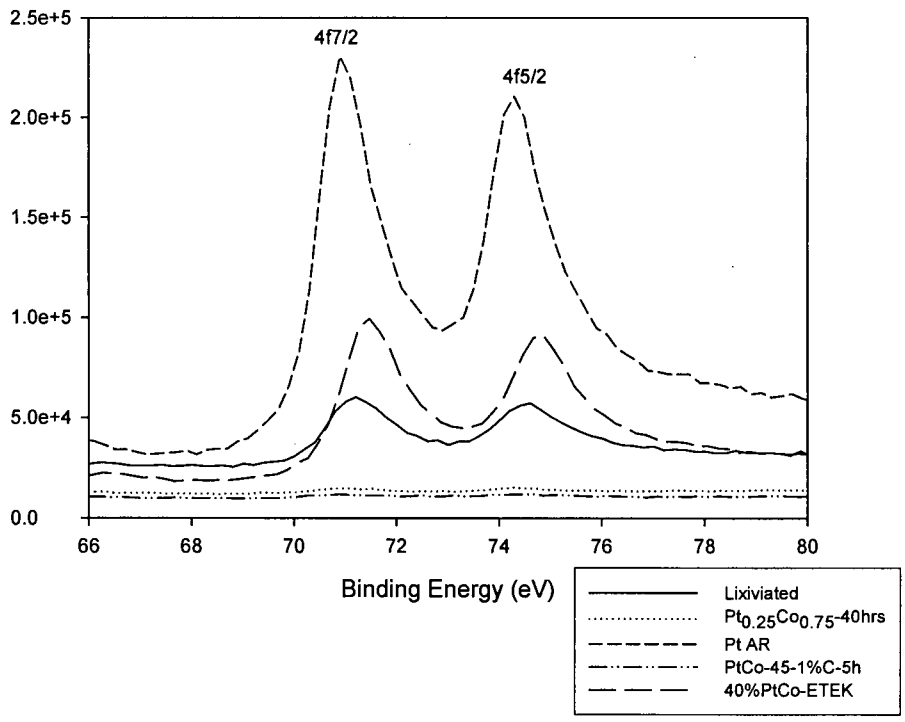

Figure 4.49(a) *Narrow scan of Pt 4f peaks of lixiviated catalyst, $Pt_{0.25}Co_{0.75}$-40h, Pt-AR PtCo-45h-1%C-5h, 40% PtCo-ETEK obtained by XPS analysis*

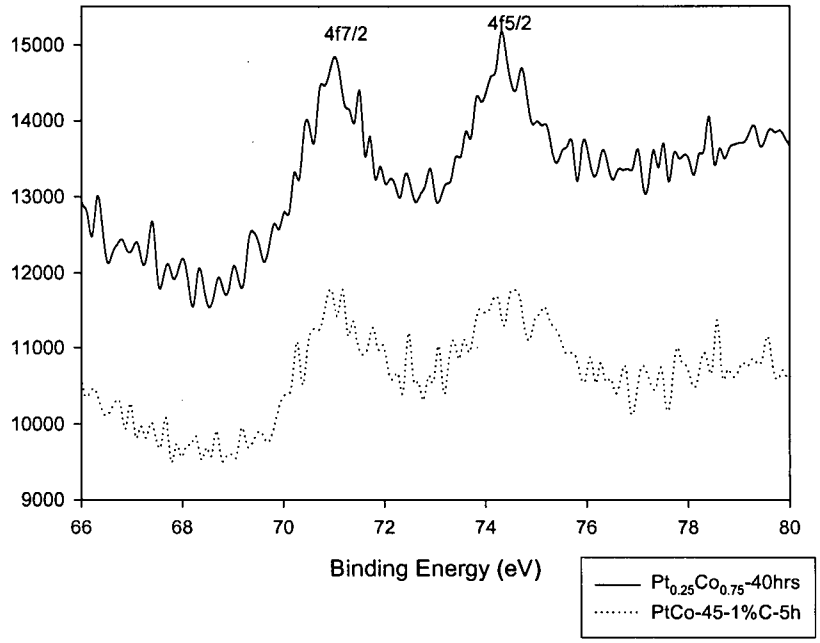

Figure 4.49(b) *Narrow scan of Pt 4f peaks of $Pt_{0.25}Co_{0.75}$-40h, PtCo-45h-1%C-5h obtained by XPS analysis*

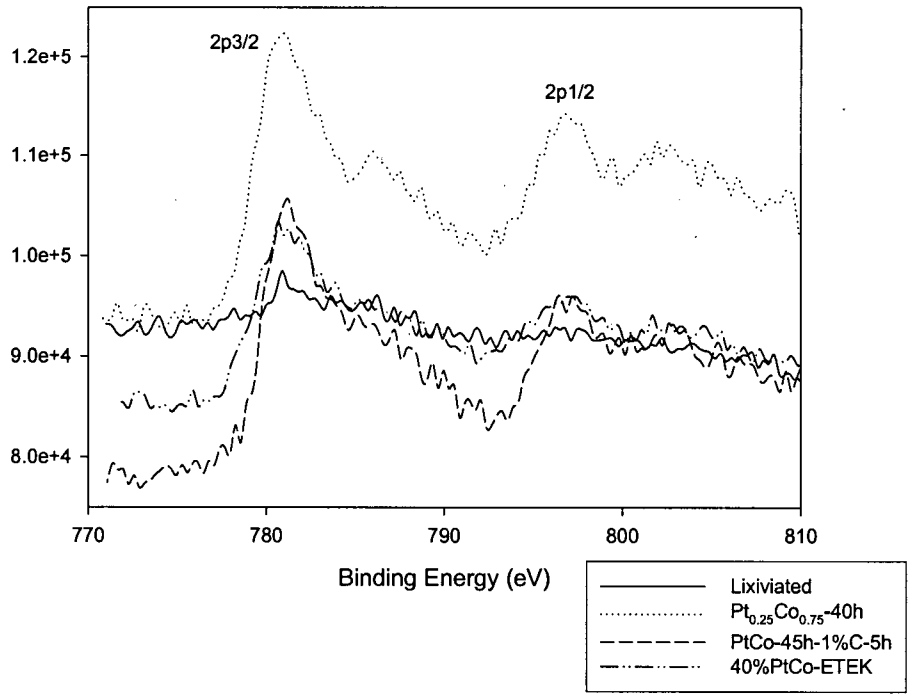

Figure 4.50 *Narrow scan of Co 2p peaks of lixiviated catalyst, $Pt_{0.25}Co_{0.75}$-40h, PtCo-45h-1%C-5h, 40% PtCo-ETEK obtained by XPS analysis*

Although Pt is not found to form any Pt-O and Pt-OH bond, the Co 2p peaks shown in Fig 4.50 are characteristics of cobalt oxide and not cobalt metal. The Co 2p3/2 and Co 2p1/2 peaks obtained from all fabricated catalysts are found at 780 and 796.5eV. The difference in the binding energy of 2p peaks is 16.5eV, which is very close to the standard data of CoO [Wagner,C.,D.,1979]. This shows that Co is in the +2 oxidation state. It has been reported in the literature that the presence of these oxidized components negatively affect the activity [Shukla,A.,K.,2001].

The surface atomic ratios of the catalysts were also evaluated by XPS. The result are given in the Tab. 4.9 which show that Pt/Co ratio for lixiviated catalyst like 40% PtCo-ETEK and unlike other fabricated catalysts, is much higher at the surface than the bulk. This shows that there is higher amount of elemental Pt at the surface than at the bulk, which could also be the reason for the better electrochemical performance of the lixiviated catalyst than other ball-milled catalysts. This will discussed at length in the next section.

Table 4.9 *Surface and bulk atomic ratios of Pt:Co catalysts obtained by XPS and EDS analysis respectively*

Sample/Compositions (at %)	Pt/Co, Surface analysis	Pt/Co, Bulk analysis
$Pt_{0.25}Co_{0.75}$-40h	0.02	0.33
PtCo-45h-1%C-5	0.0365	0.053
$Pt_{0.75}Co_{0.25}$-45h-1%C-5h- Lixiviated	2.25	1.09
40%PtCo-Etek	1.38	1.22

It is reported by Gouerec et al. that metal nanocrystallites easily get oxidized when catalysts come into contact with air for further experimentation or during leaching steps [Gouerec,P., 2000]. This can be fully supported because nanocrystallites obtained from ball milling are in a highly activated state and thus are highly liable to oxidize.

4.3.6 Electrochemical Behaviour

This section details the electrochemical behaviour of the electrocatalysts in acidic and alkaline media. Electrochemical parameters such as exchange current density (i_0) and Tafel slopes (β) are the main kinetic parameters determining the relative performance of the catalysts. Higher i_0 and lower β values are indications of good performance. The electrochemical behaviour of the electrocatalysts is then explained on the basis of the microstructural features shown by these catalysts.

The oxygen reduction reaction in acidic medium is given by,

$$O_2 + 4H^+ + 4e^- = 2H_2O, \qquad E^o = 1.229V \quad \text{.....4.11}$$

Where, E^o is the voltage at pH=0 under standard condition (P = 1atm and T=22°C) [Jones, D., A.,1996].

Figures 4.51(a-b) show potentiodynamic scans of the catalysts in 0.5M H_2SO_4 at room temperature (22 $\pm$ 2°C).

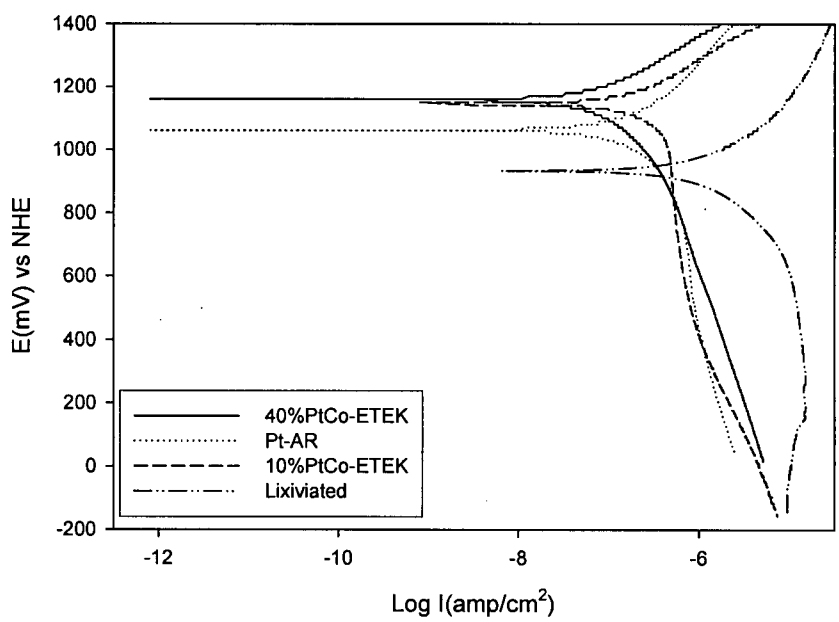

Figure 4.51(a) *Potentiodynamic scans of Pt-AR, 40% PtCo-ETEK, 10% PtCo-ETEK, lixiviated catalyst in 0.5MH_2SO_4 at 22°C*

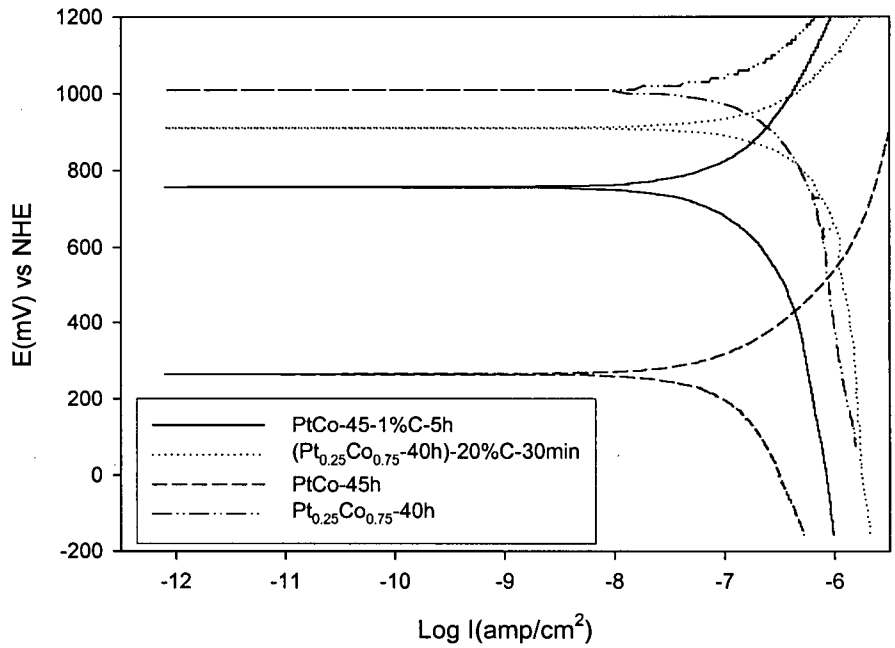

Figure 4.51(b) *Potentiodynamic scans of $Pt_{0.25}Co_{0.75}$-40h-20%C -30min, $Pt_{0.25}Co_{0.75}$-40h, PtCo-45-1%C-5h in 0.5MH_2SO_4 at 22 ℃*

Figure 4.51(a) shows that 40%PtCo-ETEK catalyst shows the best performance/oxygen reduction activity, followed by 10%PtCo-ETEK, Pt-AR and lixiviated catalyst is the decreasing order. The results are satisfactory and as expected. The 40%PtCo-ETEK shows better performance than 10%PtCo-ETEK due to larger platinum content. These two commercial catalysts, as shown in earlier sections, have the highest surface areas and smallest crystalline and particle size. Also, it is suspected that ETEK catalysts are subjected to heat treatment. The commercial Pt-AR showed lower performance than both the commercial catalysts due to it large particle size and poor dispersion. The comparable performance of the lixiviated catalyst can be attributed to its similar crystallite size and almost comparable surface area as the two commercial catalysts. Also, it has been shown in the literature that catalysts subjected to heat treatment show higher electrocatalytic activity [Kiros,Y.,1996a] and lixiviated catalyst during its fabrication process was subjected to a higher temperature of

110°C. Despite having all the microstructural characteristics similar to commercial catalysts, the lower performance of the lixiviated catalyst can be attributed to the presence of impurities such as tungsten and tungsten carbide. As presented in Fig. 4.51b, $Pt_{0.25}Co_{0.75}$-40h shows the best performance followed by $Pt_{0.25}Co_{0.75}$-40h-20%C-30min, PtCo-45h-1%C-5h and PtCo-45h. The low activity of the $Pt_{0.25}Co_{0.75}$-40h can be explained in terms of lower platinum content; secondly, it suffers from very low surface area (Table 4.8) as there is no surface agent. Other than this, Neto et al. have shown that cobalt is almost inactive in the acidic medium and the rate of reaction decreases more readily as the Co content in the alloy increases [Neto,A.,O.,1999]. Potentiodynamic polarization scans of PtCo-45h-1%C-5h and PtCo-45h in Fig. 4.51(b) show that activity of PtCo-45h-1%C-5hrs is superior than PtCo-45h. This fully confirms that the presence of carbon greatly improves the performance of the catalysts. The same trend is slightly mismatched in $Pt_{0.25}Co_{0.75}$-40h and $Pt_{0.25}Co_{0.75}$-40h-20%C-30min. It can be speculated that probably carbon did not fully alloy due to lesser milling time but merely formed a covering on platinum and Pt/Co alloy blocking the sites for the ORR. Also, the lower overpotential of all the catalysts except PtCo-45h indicates that the oxygen reduction reaction is taking place by direct-four electron mechanism, which has been discussed in detail in Chapter 2 while there is large amount of hydrogen peroxide formation by PtCo-45h catalysts.

Figures 4.52(a-b) show potentiodynamic polarization scans of the electrocatalysts in 0.25M NaOH (pH= 13) at room temperature (22±2°C). The oxygen reduction reaction in alkaline medium is given by,

$$O_2 + 2H_2O + 4e^- = OH^-, \; E^o = 0.401V \ldots\ldots\ldots\ldots\ldots\ldots\ldots\ldots 4.12$$

Where, E^o is the voltage at pH=13 under standard condition (P = 1atm and T=22°C) [Jones, D.,A.,1996]

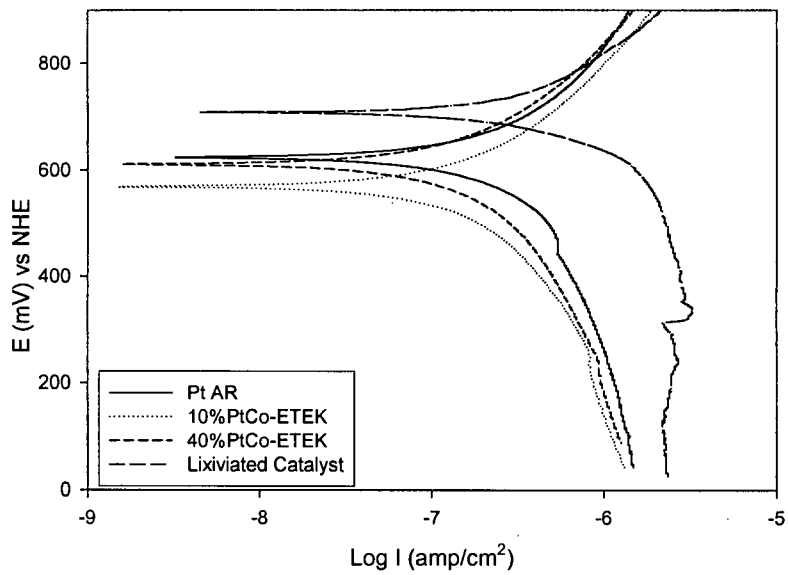

Figure 4.52(a) Potentiodynamic *scans of Pt-AR, 40% PtCo-ETEK, 10% PtCo-ETEK, lixiviated catalyst in 0.25M NaOH at 22 °C*

Figure 4.52(a) shows that 40%PtCo-ETEK gives the best performance in alkaline medium also. As described in the earlier section, smaller crystal size and higher surface area of this catalyst explains its behavior. Pt-AR, lixiviated catalysts and 10%PtCo-ETEK catalysts show the next best performance in decreasing order. The surprise superior performance of the lixiviated catalyst can be related to the fact that unalloyed/metallic cobalt, unlike acidic medium, contributed to the activity due to drying at higher temperatures [Kiros,Y.,1996a; Neto,A.,O.,1999].

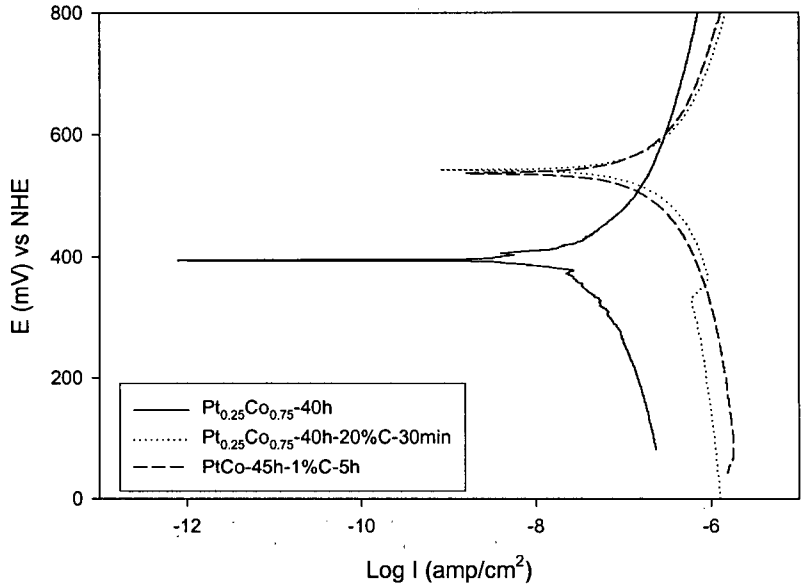

Figure 4.52(b) *Potentiodynamic scans of $Pt_{0.25}Co_{0.75}$-40h-20%C-30min, $Pt_{0.25}Co_{0.75}$-40h PtCo-45-1%C-5h in 0.25M NaOH at 22 °C*

Figure 4.52(b) shows that after lixiviated catalysts, $Pt_{0.25}Co_{0.75}$-40h-20%C-30min and PtCo-45-1%C-5h show comparable performance followed by $Pt_{0.25}Co_{0.75}$-40h. This proves that unalloyed cobalt does show some activity in alkaline medium. A closer look at the equilibrium potential o f t hese g raphs show that almost all the catalysts are performing peroxide reduction rather than oxygen reduction. A detailed study is required to find out the actual reason for this behavior.

Figures 4.53(a-b) show potentiodynamic polarization scans of the catalysts in 0.5M H_2SO_4 at high temperature (50 ± 2°C).

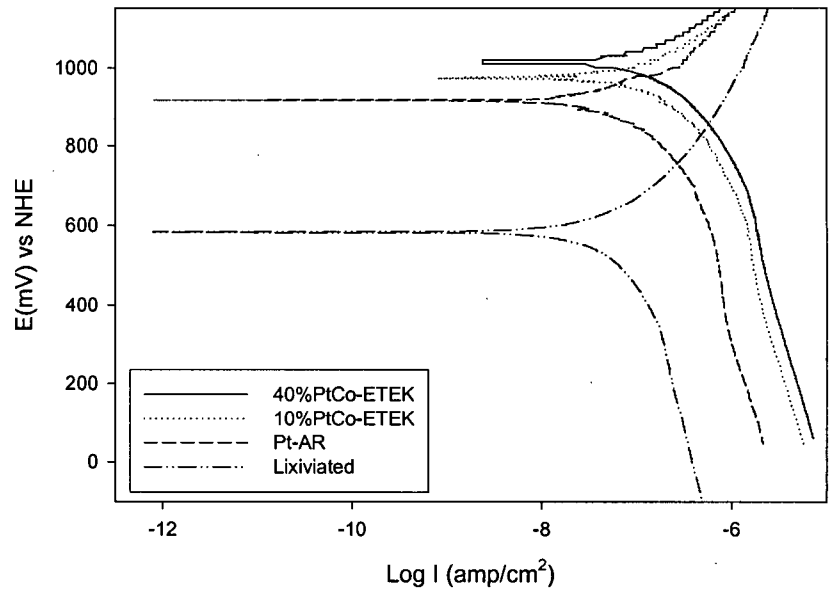

Figure 4.53(a) *Potentiodynamic test of Pt-AR, 40%PtCo-ETEK, 10%PtCo-ETEK, lixiviated catalyst in 0.5MH_2SO_4 at 50 °C*

Figure 4.53(a) shows the same trend in the performance of the electrocatalysts as at 22°C but all the catalysts showed higher overpotential than those obtained at room temperature. This behaviour is unexpected because it is known that higher working temperature decreases ohmic resistance of an operating cell. This can be explained by Figure 2.2 in chapter 2, which shows a steep decline in the voltage of fuel cells at higher temperature. But as these catalysts were not tested in a real fuel cell, this reason may not be justifiable here. The relatively poorer performance of these catalysts than at room temperature can be related to the higher dissolution/instability of these catalysts. It has been shown in the literature that transition metals in unalloyed form dissolve in the large quantity and degrade the performance of the catalysts

[Courturier,G.,1987] and XPS analysis has shown that lixiviated catalyst has a considerable proportions of unalloyed Pt and Co.

Figure 4.53(b) shows potentiodynamic scans of $Pt_{0.25}Co_{0.75}$-40h, $Pt_{0.25}Co_{0.75}$-40h-20%C-30min, PtCo-45-1%C-5h in 0.5M H_2SO_4 at 50°C. The fabricated catalysts show similar trend as at room temperature. $Pt_{0.25}Co_{0.75}$-40h showed the best performance followed $Pt_{0.25}Co_{0.75}$-40h-20%C-30min and finally PtCo-45h-1%C-5h.

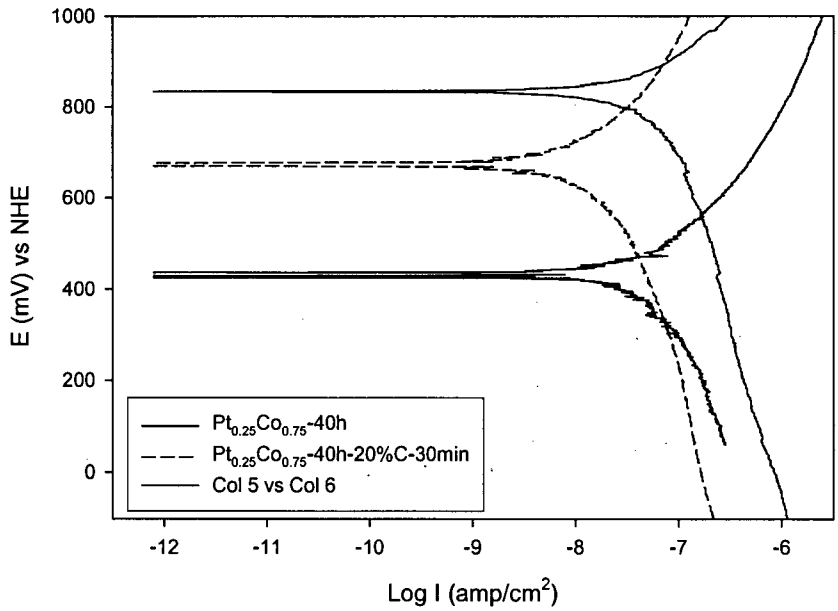

Figure 4.53(b) *Potentiodynamic scans of $Pt_{0.25}Co_{0.75}$-40h-20%C-30min, $Pt_{0.25}Co_{0.75}$-40, PtCo-45-1%C-5h in 0.5MH_2SO_4 at 50°C*

Figures 4.54(a-b) show potentiodynamic scans of the catalysts in 0.25M NaOH at high temperature (50±2°C). Figure 4.54(a) shows potentiodynamic scans of Pt-AR, 40%PtCo-ETEK, 10%PtCo-ETEK, lixiviated catalyst in 0.25M NaOH at 50°C. The figure shows that lixiviated catalyst demonstrate the best performance, followed by 40%PtCo-ETEK while Pt-AR and 10%PtCo-ETEK show almost a comparable behavior.

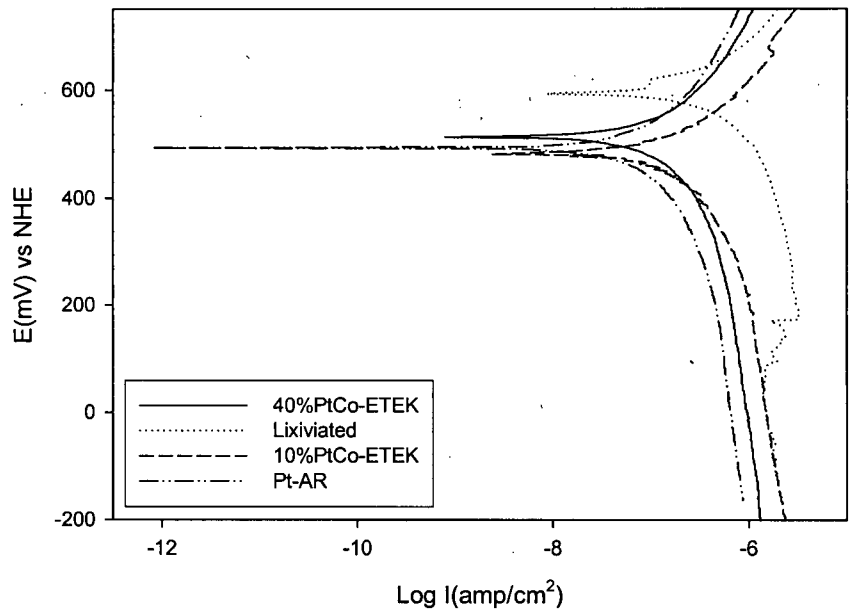

Figure 4.54(a) *Potentiodynamic tests of Pt-AR, 40% PtCo-ETEK, 10% PtCo-ETEK, lixiviated catalyst in 0.25M NaOH at 50°C*

Figure 4.54(b) shows potentiodynamic scans of $Pt_{0.25}Co_{0.75}$-40h-20%C-30min, $Pt_{0.25}Co_{0.75}$-40h, PtCo-45-1%C-5h in 0.25M NaOH at 50°C. In alkaline medium also, all fabricated catalysts show the same trend in equilibrium potential as at room temperature. The open circuit of the catalysts in alkaline medium gives an indication that there are some parallel reactions at the catalysts surface. This confirms the fact that the formation of peroxide, either as an intermediate or in a parallel reaction is more of a problem in alkaline electrolytes than acid ones [Courturier,G.,1987].

The kinetic parameters showing the Tafel slope and exchange current density of these catalysts at room temperature and higher temperature is given in Tab. 4.10. It is seen that the values of exchange current density are satisfactory and as expected. The values of Tafel slopes range from 150-300mV/d.

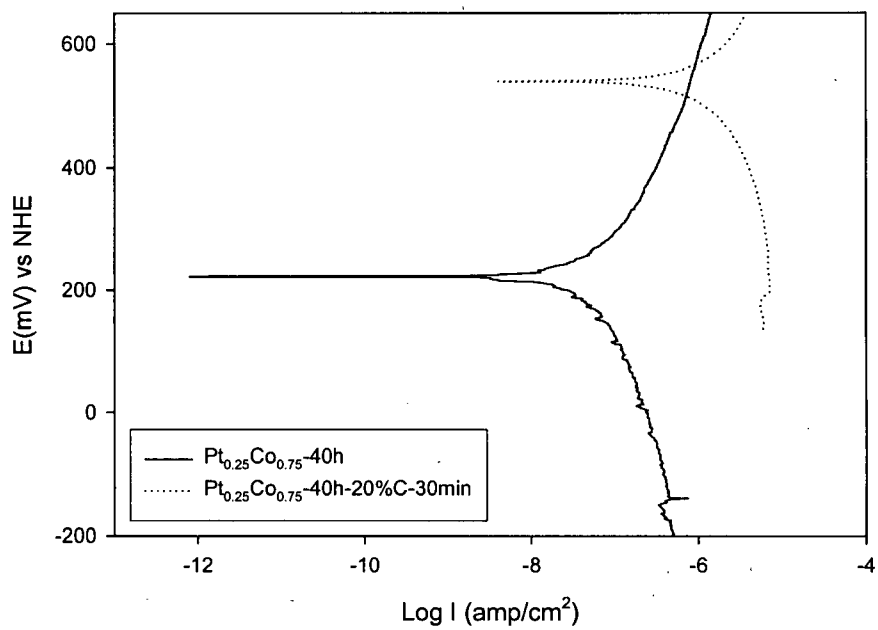

Figure 4.54(b) *Potentiodynamic scans of $Pt_{0.25}Co_{0.75}$-40h-20%C- 30min, $Pt_{0.25}Co_{0.75}$-40h in 0.25M NaOH at 50 ℃*

These are higher than expected but such high values for powder catalysts are not unusual. Couturier,G. et al. [Couturier,G.,1987] have reported such higher Tafel values for the Pt-Ta, Pt-Cr, Pt-Cr-Ta fabricated by sputtering method (see Table 2.2). Although, all catalyst show lower exchange current density at higher temperature in acidic medium, the Tafel slopes are better at higher temperature. The same tread in exchange current density and Tafel plots are found in alkaline medium at higher temperature.

Table 4.10 *Kinetic parameters, exchange current density and Tafel slopes for the catalysts at room temperature (22±2°C) and higher temperature (50±2°C) in both acidic (0.5M H_2SO_4) and alkaline medium (0.25M NaOH)*

Catalysts/Kinetic parameters	**io(amp/cm^2)**	**β(mV/d)**	**io(amp/cm^2)**	**β(mV/d)**
Acidic Medium (0.5M H_2SO_4)	Room Temperature (22±2°C)		High Temperature (50±2°C)	
Pt-AR	$4.93*10^{-07}$	282.14	$4.40*10^{-7}$	122.52
10%PtCo-ETEK	$2.84*10^{-07}$	166.95	$1.00*10^{-7}$	153.73
40%PtCo-ETEK	$6.56*10^{-07}$	146.69	$1.29*10^{-7}$	159.93
$Pt_{0.25}Co_{0.75}$-40h	$2.18*10^{-07}$	317.61	$1.16*10^{-8}$	155.76
$Pt_{0.25}Co_{0.75}$-40h-20%C-30min	$1.60*10^{-07}$	179.00	$3.0*10^{-8}$	160.00
PtCo-45h-1%C-5h	$9.17*10^{-08}$	284.47	$4.49*10^{-9}$	157.95
PtCo-45h-1%C-5h- lixiviated	$3.39*10^{-07}$	167.2	$3.00*10^{-7}$	125.69
PtCo-45h	$1.18*10^{-8}$	238.85	-	-
Alkaline medium (0.25M NaOH)	Room Temperature (22±2°C)		High Temperature (50±2°C)	
Pt-AR	$2.74*10^{-7}$	292.57	$1.74*10^{-7}$	162.86
10%PtCo-ETEK	$1.37*10^{-7}$	212.42	$6.18*10^{-8}$	220.52
40%PtCo-ETEK	$1.94*10^{-7}$	261.37	$3.15*10^{-8}$	206.93
$Pt_{0.25}Co_{0.75}$-40h	$1.00*10^{-8}$	256.36	$2.51*10^{-8}$	138.68
$Pt_{0.25}Co_{0.75}$-40h-20%C-30min	$3.16*10^{-7}$	265.32	$3.50*10^{-8}$	182.11
PtCo-45h-1%C-5h	$2.02*10^{-7}$	236.57	-	-
PtCo-45h-1%C-5h- lixiviated	$3.74*10^{-7}$	234.73	$1.53*10^{-7}$	244.14

The redox behaviour and the relative current density of the catalysts were determined using cyclic voltammetry.

Figures 4.55(a-b) show the cyclic voltammograms of the catalysts at room temperature in acidic medium. Figure 4.55(a) shows that lixiviated catalyst shows the best current density, followed by 10%PtCo-ETEK, 40%PtCo-ETEK, and finally Pt-AR. The lixiviated catalyst showed hydrogen adsorption/desorption peaks at 0.18 V and 0.3V whereas 10%PtCo-ETEK shows an oxygen reduction peak at 0.85V. All potentials are measured with respect to NHE. It has been reported that Pt catalysts produce currents at low potentials (0-0.3V vs. NHE) due to Pt-H interactions (hydride adsorption/desorption) and at high potentials, currents are found corresponding to Pt-O interactions (oxide formation/ reduction) [Hooger, G.2003]. It is seen in Figure 4.55(a) that lixiviated catalyst produce more current in the low potential region. It shows a quick oxygen reduction behavior between 0.4 to 0.95V and current is mainly produced due to oxide formation. This shows that lixiviated catalyst is under going anodic polarization. All the commercial catalysts are showing long oxygen reduction region from 0.4V to 1.2V. The current produced in these catalysts is mainly due to oxygen reduction and not due to hydrogen adsorption. The voltammograms of these catalyst show that there is less amount of oxide formation in the commercial catalysts.

Figure 4.55(b) shows cyclic voltammogram of $Pt_{0.25}Co_{0.75}$-40h, $Pt_{0.25}Co_{0.75}$-40h-20%C-30min, PtCo-45h-1%C-5h in 0.5MH_2SO_4 at 22°C. The graphs are almost featureless. This is because the surface area of these ball-milled catalysts is smaller than the lixiviated catalysts and commercial catalysts. Figure 2.10b is an evidence that ball milled material without surface agent shows no response at all, and shows little response with surface agent (Fig. 2.10c)

[Lalande,G.,1997]. Also, a look at Fig 4.55b shows that these catalysts are producing current only in the low potential region, which is mainly due to hydrogen adsorption.

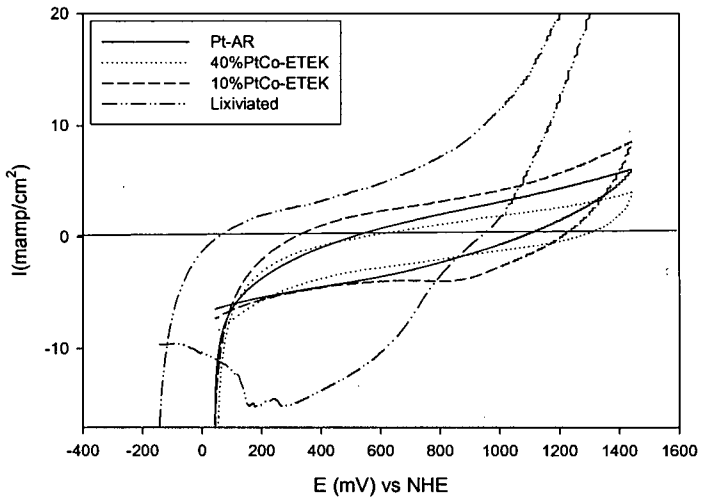

Figure 4.55(a) *Cyclic Voltammograms of Pt-AR, 40% PtCo-ETEK, 10% PtCo-ETEK, lixiviated catalyst in 0.5MH_2SO_4 at 22 °C*

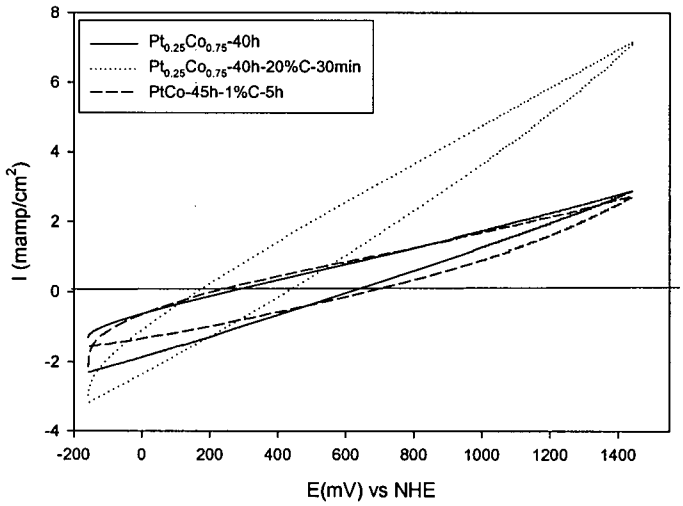

Figure 4.55(b) *Cyclic Voltammograms of $Pt_{0.25}Co_{0.75}$-40h $Pt_{0.25}Co_{0.75}$-40h-20%C-30min, PtCo-45-1%C-5h in 0.5MH_2SO_4 at 22 °C*

These catalysts are not showing oxygen reduction behavior. At higher potentials, these catalysts are undergoing anodic polarization. The presence of cobalt oxide film is indeed detected by XPS.

Figures 4.56(a-b) gives cyclic voltammograms of the catalysts in alkaline medium at 22°C. In alkaline medium, ORR reaction produces voltage of 0.401V. It can be seen in Fig 4.56a

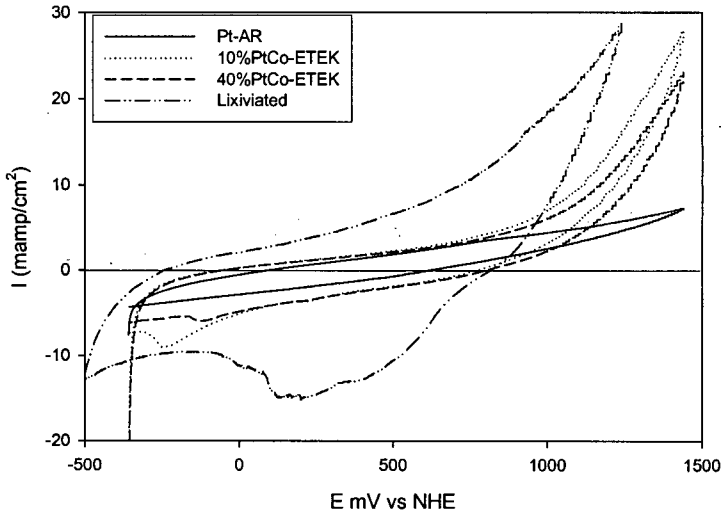

Figure 4.56(a) *Cyclic Voltammograms of Pt-AR, 40% PtCo-ETEK, 10% PtCo-ETEK, lixiviated catalyst in 0.25M NaOH at 22 °C*

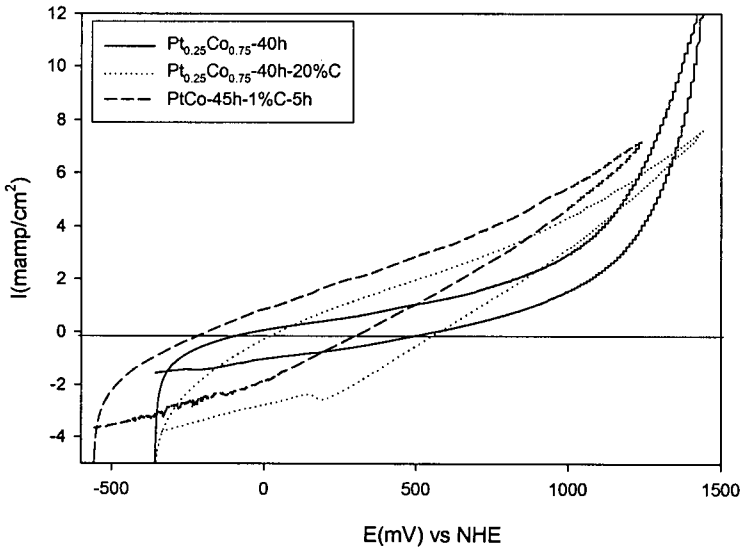

Figure 4.56(b) *Cyclic Voltammograms of $Pt_{0.25}Co_{0.75}$-40h, $Pt_{0.25}Co_{0.75}$-40h-20%C-30min, PtCo-45-1%C-5h in 0.25M NaOH at 22 °C*

that lixiviated catalyst is showing large oxygen reduction behaviour. It shows a OR peak at 0.3 V. But though lixiviated catalyst and all the commercial catalysts are showing larger oxygen reduction region, the catalysts are also undergoing anodic polarization. All the other fabricated catalysts are also showing appropriate OR potential but are also undergoing oxidation (Fig 4.56b).

Cyclic voltammograms of the catalysts at high temperatures (50±2°C) in acidic medium are shown in Fig 4.57(a-b). Figure 4.57(a) shows that at high temperature, performance of the lixiviated catalyst is drastically reduced whereas all the three commercial catalysts, 40%PtCo-ETEK, 10%PtCo-ETEK and Pt-AR show better performance. The instability of the lixiviated catalysts in acidic medium can be a reason for the low performance of this catalyst. Figure 4.57(b) shows cyclic voltammograms of $Pt_{0.25}Co_{0.75}$-40h-20%C-30min, $Pt_{0.25}Co_{0.75}$-40h, PtCo-45-1%C-5h. All the three catalysts are showing lower current density and large oxide formation.

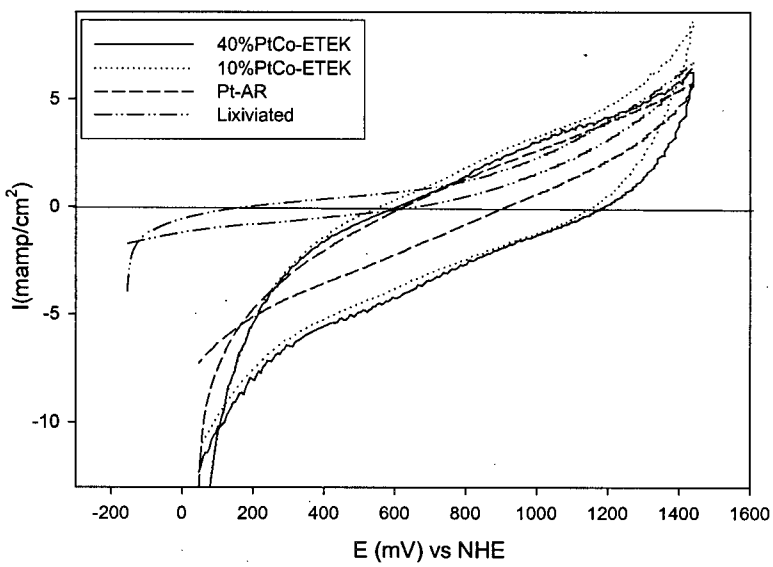

Figure 4.57(a) *Cyclic Voltammograms of Pt-AR, 40% PtCo-ETEK, 10% PtCo-ETEK, lixiviated catalyst in 0.5MH_2SO_4 at 50 °C*

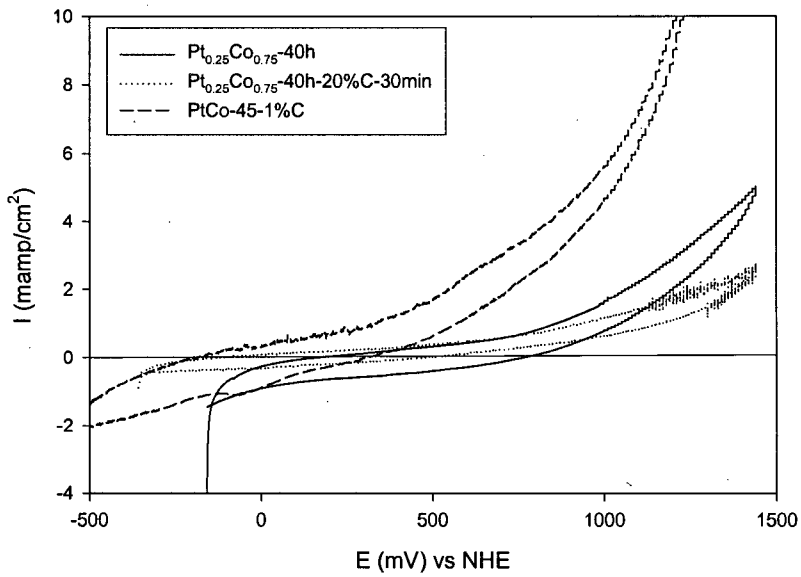

Figure 4.57(b) *Cyclic Voltammograms of $Pt_{0.25}Co_{0.75}$-40h-20%C-30min, $Pt_{0.25}Co_{0.75}$-40h, PtCo-45-1%C-5h in 0.5MH_2SO_4 at 50 °C*

Cyclic voltammograms of the catalysts at high temperatures in alkaline media are shown in Figs 4.58(a-b).

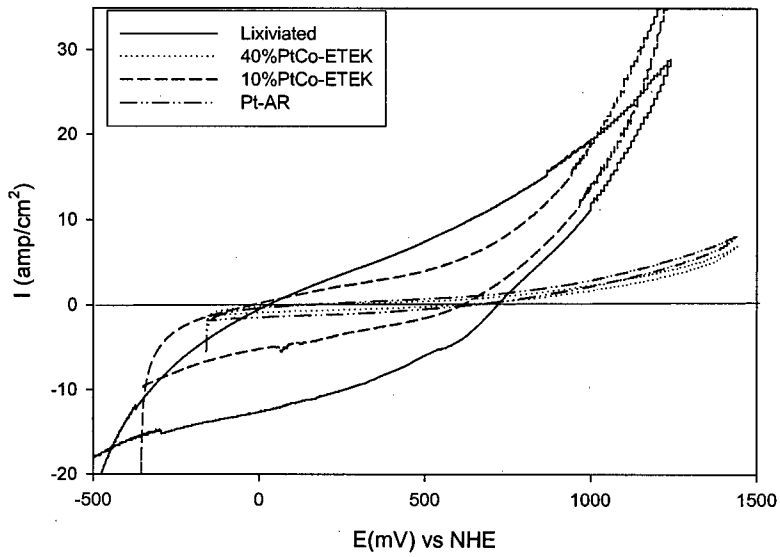

Figure 4.58(a) *Cyclic Voltammograms of Pt-AR, 40% PtCo-ETEK, 10% PtCo-ETEK, lixiviated catalyst in 0.25M NaOH at 50 °C*

In alkaline medium, the lixiviated catalyst showed the best current density even at high temperature (Fig.4.58a). The next best performance is shown by 10% PtCo-ETEK. This suggests that though unalloyed cobalt degrades the performance by dissolution in acidic medium, it significantly contributes to the performance in alkaline medium. The performance of the Pt-AR and 40%PtCo-ETEK is surprisingly quite low. No appropriate reason can be suggested for this behavior. Figure 4.58b shows the cyclic voltammograms of $Pt_{0.25}Co_{0.75}$-40h

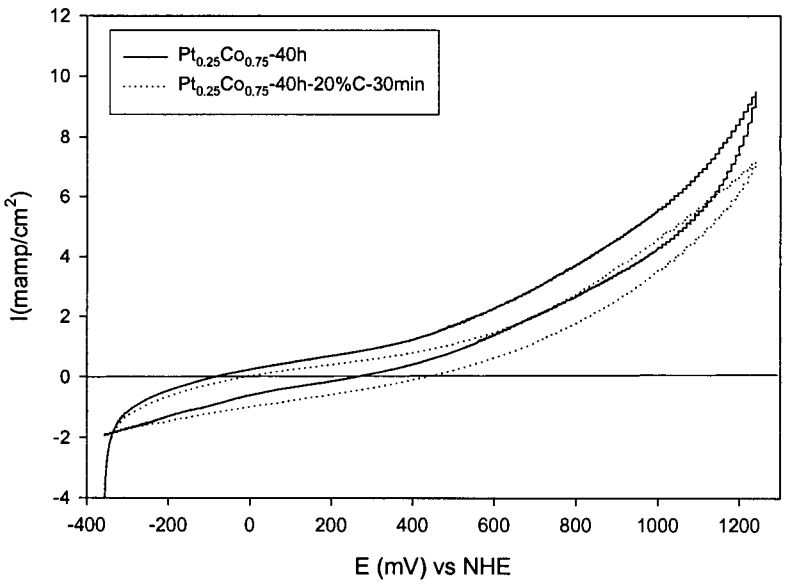

Figure 4.58(b) *Cyclic Voltammograms of $Pt_{0.25}Co_{0.75}$-40h-20%C-30min, $Pt_{0.25}Co_{0.75}$-40h in 0.25M NaOH at 50 °C*

and $Pt_{0.25}Co_{0.75}$-40h-20%C-30min. These fabricated catalysts show almost the same trend in activity as shown at room temperature in alkaline medium.

The performance of all the catalyst in both the media is lower at high temperature as compared to room temperature. Apart from the explaination given in the potentiodynamic measurements, lower performance of the catalyst at higher temperature can be attributed to other factors such as the changes in the properties of nafion and the morphology of catalyst surface at

high temperatures. It is known that adsorption is fast at high temperatures and thus the main reason for the low activity at the higher temperature can be attributed to the adsorption of oxygen on the platinum surface, which occupies all platinum sites and thus prevents their use for further catalysis. In cyclic voltammetry, most of the catalysts did not show a prominent oxidation-reductions peak. The catalysts are mainly showing capacitive currents. This is because tests were done in unstirred/non-rotating conditions. It was assumed that sparging of the cell with O_2 would over come the mass transport limitation. This factor might have influenced the cyclic voltammogram results of this thesis. Literature shows that testing in unstirred conditions results in capacitive currents [Lalande,G.,1997; Tamizhmani,G.;1994].

Chapter 5

Conclusion and Recommendations

This thesis involved two major tasks: (i) fabrication of the catalysts and (ii) testing of these catalysts to detect the activity.

Fabrication Process:

The optimization of the ball milling parameters is very important to produce particles of required size without much contamination of the powder. The materials of the ball milling media i.e. vial and balls should be appropriately chosen to minimize the contamination of the powder. The milling/cooling cycles should be carefully adjusted to avoid sintering of the powder. The milling atmosphere also plays an important role in avoiding oxidation of the powder. It was proved that the higher the ball to powder ratio, the better the particle size refinement.

With the results of this thesis, it can be concluded that ball milling is capable of producing porous agglomerates of about 30 microns size made up of nano-crystallites of less than 10 nm. But though nanoparticles could be obtained, ball milling does have the limitation that particles tend to cold weld. And, hence, PCAs plays an important factor in obtaining better dispersion and homogenization of powder.

PCAs were carbon and stearic acid. Stearic acid has a strong tendency to decompose into carbon, hydrogen and oxygen. These elements get interspersed in the lattice of the elements. Among both the PCAs, carbon was a better process control agent as it gave better particle size refinement, increased surface area, reduced wear, and didn't contaminate the system, as it was always part of catalyst layer. Carbon also provides more catalytic sites and is thus a better surface agent than stearic acid. But, carbon also has a strong tendency to form carbides and

hence, careful manipulation of milling variables is very important to control carbide formation. This was successfully achieved in this work.

Further enhancement of the surface area was done by lixiviation of the catalyst. Lixiviation improves the surface area of the catalyst by eating away the non-noble metal and regenerates the bare Pt sites that are otherwise covered by the cobalt or carbon powders.

Ball milling was able to form non-equilibrium Pt-Co binary alloys and extended tertiary solid solutions of Pt-Co-C, which are highly desirable.

Catalysts Performance:

The exchange current density and Tafel slopes obtained from the electrochemical tests revealed that the lixiviated catalyst (PtCo-45h-1%C-5h-Lixiviated) is the best catalyst among all the fabricated catalyst. The particle size of this catalyst was comparable to the commercial catalysts procured from E-TEK. It produced equivalent exchange current density as the commercial catalysts and infact, the activity was more than 10%PtCo- ETEK commercial catalyst in acidic medium at the room temperature. The porous structure with high surface area, characteristic of the lixiviated catalyst, is the main reason for the comparable performance of the lixiviated catalyst with commercial E-TEK catalysts. Lixiviated catalysts showed a prominent oxygen reduction peaks which are almost not traced in the other fabricated catalysts. Apart from a porous structure, drying of the lixiviated catalysts at higher temperature may have been another factor for its superior performance. This makes it clear that ball-milled samples should be subjected to lixiviation and high temperature heating. As explained earlier, lixiviation greatly improves the porosity and surface area of the catalysts and heat treatment increases alloying and thus produces optimum nearest neighboring distance, which enhances the activity significantly.

The performance of the non-lixiviated fabricated catalysts was lower than the lixiviated catalyst but in no way discouraging.

At high temperature, exchange current density and Tafel slope of all the catalyst was lower than that at room temperature. This could be due to the stability of the catalyst at higher temperature. Also, it is showed that there was higher metal dissolution at higher temperature.

The fabricated catalysts showed superior performance in alkaline medium than acidic medium. This might be because cobalt is almost inactive in acidic medium [Neto,A.,O.,2002].

Although this work shows an activity of the order of $10^{-7}A/cm^2$ for Pt-Co/C alloys for the ORR, the incorporation of a noble metal is still a pre-requisite for a catalyst. XPS analysis showed that catalysts having higher Pt atomic percent at the surface showed better activity. Experimental results from XRD also made evident that the activity of the catalyst depends not only on the composition of the catalyst but also on the surface morphology of the catalyst, particle size and surface area.

It is also to state that most of the electrocatalysts were checked for reproducibility except few as the amount of electrocatalysts that could be fabricated was limited due to the high cost of platinum metal.

Recommendations:

Ball milling is one of the prominent techniques to produce nanosized particles, but it produces contaminations in the powder due to attrition of the vials and balls. This attrition was controlled to a great extent by addition of process control agent but a very small amount of tungsten carbide was still found in the samples. This can be avoided by using a jet milling technique.

Figure 5.1 shows the flow diagram of Mircon-Master® jet pulverizer from the Jet Pulverizer company. In jet milling, the material is driven at near sonic velocity around the perimeter of the chamber by multiple jets of air or steam. Milling involves no grinding media and the size reduction is the result of the high-velocity collisions between particles of the process material itself. The chamber of a jet mill is designed such that it allows recirculation of over-sized particles, enhancing the incidence and the effect of these collisions.

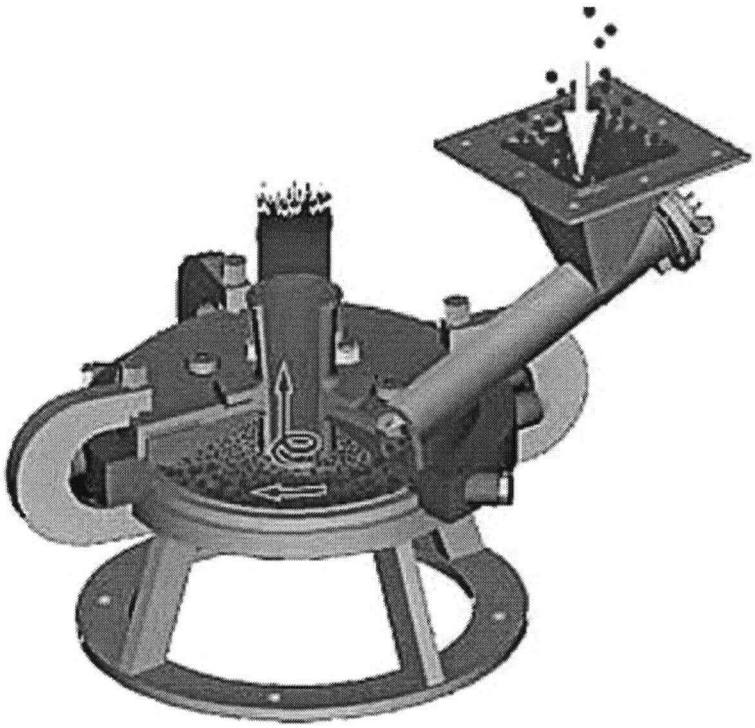

Figure 5.1 *Flow diagram of Mircon-Master ® Jet Pulverizer from the Jet Pulverizer Company [http://www.jetpul.com/mequip/milloper.htm]*

This process involves no moving parts or screens and therefore, is suitable for virtually any friable or crystalline materials, even materials that are very abrasive. And, since contamination can be avoided and no excess heat is produced, jet milling is highly suitable for materials that must remain ultra-pure and those that are heat sensitive [http://www.jetpul.com/mequip/milloper.htm]

Also, in view of promising results of lixiviated catalysts, heat treatment of the PtCo/C electrocatalysts is highly recommended.

When testing the catalysts, the O_2 sparging pressure greatly affects mass transport characteristics and hence performance, therefore it is recommended that O_2 gas flow be controlled by a flow meter.

Chapter 6

Future Work

Further experimentation is required to detect the type of gas released at the electrodes during electrochemical test. This would require testing of catalysts by a Rotating Ring Disc Electrode (RRDE). RRDE involves an addition of a concentric-ring electrode surrounding the disc separated by an insulating gap. RRDE has proved to be an extremely useful technique for elucidating various electrode mechanisms through generation and detection of reactions at the disk and ring respectively [Wang,J.,1994]. Further study is required to find a reason for the instability of the catalyst at high temperature in both media.

As these catalysts showed promising results, the future work would involve the study of these catalysts in the complete fuel cell set up. It would involve the fabrication of membrane electrode assembly (MEA). The figures 6.1 and 6.2 show a membrane electrode assembly made up of Pt-Co /C catalyst from ETEK.

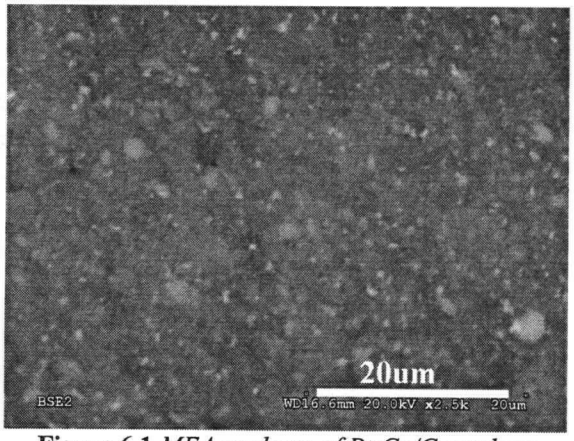

Figure 6.1 *MEA made up of Pt:Co/C catalysts*

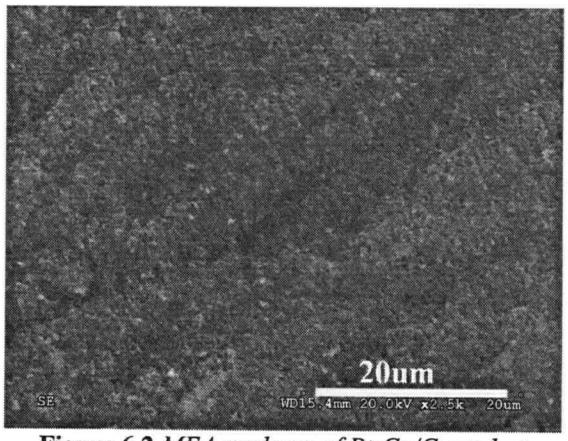

Figure 6.2 *MEA made up of Pt:Co/C catalysts*

References

- ASM Handbook, *"Alloy phase diagrams,"* Vol. 3, ed. Baker,H., Section 2, pp 146.

- Appleby,A.,J., *"Corrosion in Low and High Temperature Fuel cells- An overview,"* Corrosion, 1987, 43(7), pp 398-408.

- Beard,B.,C., Ross, P.,N., *"The structure and activity of Pt-Co alloys as oxygen reduction electrocatalysts,"* J. Electrochem. Soc., 1990, Vol. 137 (11), pp 3368-3374.

- Bockris,J.,O.,M., Srinivasan,S., *"Fuel Cells: Their Electrochemistry,"* 1969, McGraw-Hill Book Company.

- Carrette,L.,Friedrich,K.,A.,Stiming,U., *"Fuel Cells: Principles, types, fuel and applications,"* ChemPhysChem, 2000, Vol. 1, pp 162-193.

- Costamagma,P., Srinivasan,S., *"Quantum jumps in the PEMFC science and technology from the 1960s to the year 2000.Part I. Fundamental scientific aspect,"* J. Power sources, 2001, Vol.102, pp 242-252.

- Cote,R., Lalande,G., Guay,D., Dodelet,J.,P., Denis,M.,C., *"Iridium and ruthenium based electrocatalysts for oxygen reduction in polymer electrolyte fuel cells,"* Proc. of the second international symposium on New material for fuel cell and Modern battery systems II, 1997, pp 743-55.

- Couturier,G., Kirk,D.,W., Hyde,P.,J., Srinivasan,S., *"Electrocatalysis of the hydrogen oxidation and of the oxygen reduction reactions on Pt and some alloys in alkaline medium,"* Electrochimica Acta, 1987, Vol. 32 (7), pp 995-1005.

- Denis,M.,C., Lalande,G., Guay, D., Dodelet, J.,P., Schulz, R., *"High Energy ball-milled Pt and Pt-Ru catalysts for polymer electrolyte fuel cells and their tolerance to CO,"* J. App. Electrochem., 1999, Vol. 29, pp 951-960.

- Denis,M,C.,Gouerec,P.,Guay,D.,Dodelet,J,P.,Lalande,G.,Schulz,R., *"Improvement of the high energy ball-milling preparation procedure of CO tolerant Pt and Ru containing catalyst for polymer electrolyte fuel cells,"* J. Appl. ElectroChem, 2000, Vol. 30, pp 1243-1253.

- Hunter,E.,E., *"Practical electron microscopy: a beginners illustrated guide,"* 1993, Cambridge university press, Cambridge, New York.

- Farhat,Z.,N., *"Contribution of crystallographic texturing to the sliding friction behaviour of fcc and hcp metals,"* Wear, 2001, Vol. 250, pp 401-408.

- Faubert,G., Guay,D., Dodelet, J.,P., *"Pt inclusion compounds as oxygen reduction catalysts in polymer–electrolyte fuel cells,"* J. Electrochem. Soc., 1998, Vol.145 (9), pp 2985-2992.

- Friedrich, K.,A., Geyzers, K., P., Dickinson, A.,J., Stimming, U., *"Fundamental aspects in electrocatalysis: from the reactivity of single-crystals to fuel cell electrocatalysts,"* J. Electroanaly. Electrochem., 2002, Vol. 524-525, pp 261-272.

- Galeotti, M., Atrei,A., Bardi,U., Cortigiani,B.,Rovida,G.,Torrini,M., *"Structural study of alloy formation at the Co-Pt (111) interface,"*Surface Review and Letters, 1996, Vol.3 (5 & 6), pp 1691-1700.

- Gamburzev,S., Velev,O.,A., Srinivasan, S., Appleby, A.,J., *"Carbon Supported Ternary platinum alloys as oxygen reduction catalysts for proton exchange membrane fuel cells,"* Proc. Electrochem. Soc., Vol. 97 (13), pp 78-85.

- Glass,J.,T.,Cahen,G.,L.,Stoner,G.,E.,Taylor,E.,J., *"The effect of metallurgical variables on the electrocatalytic properties of PtCr alloys,"* J.electrochem. Soc., 1987,Vol 134, pp 58-65.

- Gottesfeld,S.,Zawodzinski,T.,A, *"Polymer Electrolyte Fuel Cell,"* Electrochemical Science and Engg, 1998,Vol.5, ed. Alkaire, R,C., New York, Wiley-VCH, pp 197-301.

- Gouerec,P.,Denis,M.,C.,Guay,D.,Dodelet,J.,P.,Lalande,G.,Schulz,R.,*"High energy ball-milled Pt-Mo catalysts for polymer electrolyte fuel cell and their tolerance to Co,"* J.Appl. Electrochem., 2000, Vol.147(11), pp 3989-3996.

- Greef,R., Peat, R., Peter,L., M., Pletcher,D., Robinson,J., *"Instrumental Methods in Electrochemistry,"* 1985, Ellis Horwood Ltd and John Wiley & sons, N.Y., USA.

- Hooger,G., *"Fuel Cell Technology Handbook,"* 2003, CRC Press, US.

- Ivanov,E.,Makhlouf,S.,A.,Sumiyama,K.,Yamauchi,H.,Suzuki,K.,Golubkuva,G.,*"Structural and magnetic properties of non-equilibrium bcc nickel prepared by leaching of mechanically alloyed $Ni_{35}Al_{65}$,"* J. Alloys and Compounds, 1992,185, pp 25.

- Jalan.,V., Taylor.,E.,J., *" Importance of interatomic spacing in catalytic reduction of oxygen in phosphoric acid,"* J. Electrochem. Soc., 1983, Vol. 130 (11), pp 2229-2302.

- Jones,D.,A., *"Principles and Prevention of Corrosion. Second Edition,"* 1996, Prentice Hall, Upper Saddle River, NJ.

- Kordesch, K., Simader, G., *" Fuel Cells and their applications,"* 1996,VCH, Germany.

- Kinoshita,K.,*"Electrochemical Oxygen technology,"* 1992, J.Wiley & Sons Inc., USA.

- Kiros,Y., *"Electrocatalytic properties of Co, Pt, and Pt-Co on carbon for the reduction of oxygen in alkaline fuel cells,"* J. Electrochem. Soc, 1996a,Vol. 43 (7), pp 2152-2157.

- Kiros,Y., Sampathrajan,A., Ramanathan,M., *"Performance of Pt-Co alloys and CoTPP catalysts for the reduction of oxygen in AFC,"* Fuel cell seminar. Program and Abstract, 1996b, pp 698-701.

- Klug,H.,P., Alexander,L.,E.,*"X-Ray Diffraction Procedures for polycrystalline and Amorphous Material,"*1954, Wiley-interscience Publication, USA.

- Kuhrt,C.,Schropf,H.,Schultz,L.,Arzt,E., "Mechanical alloying for structural applications," ASM International, 1999, ed, de Barbadillo,J.,J., pp 189-195.

- Kumar,G,S., Raja, M., Parthasarathy,S.,*"High performance electrodes with very low platinum loading for polymer electrolyte fuel cells,"* J. Electrochimica, 1995, Vol 40 (3), pp 285-290.

- Kyong,T.,K., Hwang,J.,T., Kim,G.,Y.,Chung,J.,S., *"Surface and catalytic properties of iron-platinum/carbon electrocatalysts for cathodic oxygen reduction in PAFC,"* J.ElectroChem. Soc.,1993, Vol.140 (1), pp 31-36.

- Lai,E.,K.,W., Beattie,P.,D., Holdcroft,S.,*"Electrocatalytic reduction of oxygen by Platinum microparticles deposited on polyaniline films,"* Synthetic Metals, 1997, Vol. 84, pp 87-88.

- Lalande,G., Denis,M.,C., Gouerec,P., Guay,D., Dodelet,J.,P., Schulz,R., *"Pt-based nano-composites produced by high energy ball milling as electrocatalyst in polymer electrolyte fuel cells,"* J. New Mat. for Electrochem. Sys., 2000, Vol.3, pp. 185-192.

- Lalande, G., Denis, M.,C., Guay, D., Dodelet, J., P., Huot, J., Schulz, R., *"Utilization of the ball milling technique in the synthesis of electrocatalysts for H_2 oxidation in polymer electrolyte fuel cells,"* Proc. Second International Symposium on new materials for fuel cells and modern battery systems II, 1997, Savadogo, O et al., Ecole Polytech., Montreal, pp 720-731.

- Lalande,G., Cote,R., Guay,D., Dodelet,J.,P., *"Chromium-based electrocatalysts for oxygen reduction polymer electrolyte fuel cells,"* Proceedings of the second international symposium on New material for fuel cell and Modern battery systems II, 1997, pp 768-77.

- Lalande,G., Cote,R., Tamizhmani,G., Guay,D., Dodelet,J.,P., *"Physical, chemical and electrochemical characterization of heat treated tetracarboxylic cobalt phthalocyanine adsorbed on carbon black as electrocatalyst for oxygen reduction in polymer electrolyte fuel cells,"* Electrochiminca Acta, 1995,Vol.40 (16), pp 2635-2646.

- Lalande,G., Denis, M,C., Guay, D., Dodelet, J., P., Schulz, R.,*"Structural and surface characterization of nanocrystalline Pt-Ru alloys prepared by high-energy ball-milling,"* J. Alloys and Compounds, 1999, Vol. 292, pp 301-310.

- Larminie, J., Dicks,A., *"Fuel Cell Systems Explained,"* 2002, John Wiley & Sons Ltd.

- Lin,J.,C., Kunz,H.,R., Fenton,J.,M., Fenton,S.,S., *"The fuel Cell,"* 2004, A short Course, Department of Chemical Engineering, University of Connecticut, USA, pp 38-47.

- Luczak,F.,J., Lansman,D.,A., *"Ternary fuel cell catalysts containing platinum, cobalt and chromium,"* 1984, US Patent No. 4447506,

- Luczak, F., Douglas,A., *" A ordered ternary fuel cell catalysts containing platinum and cobalt,"* 1987, US Patent No. 4711829.

- Mizuhata,M., Yasuda,K., Oguro,K., Takenaka,H., *"Preparation of gas diffusion electrode with highly active catalyst for PEMFCs,"* Electrochem. Soc. Proceedings, Vol. 95-23, pp 24-32.

- Mukerjee,S., Srinivasan,S., Soriaga,M.,P., McBreen, J., *"Role of Structural and electronic properties of Pt and Pt alloys on electrocatalysis of oxygen reduction. An InSitu XANES and EXAFS investigation,"* 1995a, J. Electrochem. Soc. Vol. 142, (5), pp 1409-1422.

- Mukerjee,S., Srinivasan,S., Soriaga,M.P., McBreen,,J., *"Effect of preparation conditions of Pt alloys on their electronic, structural and electrocatalytic activities for oxygen reduction-XRD, XAS, and electrochemical studies,"* J. Phys. Chem, 1995b, Vol 99, pp 4577-4589.

- Min,.M.,K., Cho,J.,Cho,K., Kim,H., *"Particle size and alloying effects of Pt-based alloy catalysts for fuel cell applications,"* Electrochimica Atca, 2001, Vol. 45, pp 4211-4217.

- Neergat,M., Shukla,A.,K., Gandhi,K.,S., *"Platinum-based alloys as oxygen-reduction catalyst for solid-polymer-electrolyte direct methanol fuel cells,"* J. Appl. Electrochem., 2001,Vol .31, pp 373-378.

- Neto,A.,O., Giz, M.,J., Pervez,J., Ticianeeli, E.,A., Gonzalez,E.,R., *"The electro-oxidation of ethanol on Pt-Ru and Pt-Mo particles supported on high –surface –area carbon,"* J. Electrochem. Soc., 2002, Vol.149 (3), pp A272-A279.

- Neto,A.,O., Perez,J., Gonzalez,E.,R., Ticianelli,E.,A., *"Platinum/Co electrocatalyst dispersed on high surface area carbon. Study of the oxygen reduction reaction,"* J. New Mat. Electrochem. Sys., 1999, Vol.2, pp 189-195.

- Paganin,V,A., Ticianelli,E.A., Gonzalez,E,R., *"Fabrication and evaluation of electrodes for polymer electrolyte fuel cell,"* Electrochem. Soc. Proceedings, Vol. 95-23, pp 102-114.

- Paulus,U.,A.,Wokaun,A.,Schere,G.,G.,Schmidt,T.,J.,Stamenkovi,V.,Radmilovic,V.,Markovic, N.,M., Ross,P.N., *"Oxygen Reduction on carbon- supported Pt-Ni and Pt-Co alloy catalysts,"* J.Phys.ChemB, 2002, Vol.106, pp 4181-4191.

- Perez,J.,Gonzalez,E.,R.,Ticianelli,E.,A., *"Oxygen electrocatalysis on thin porous coating rotating platinum electrodes,"* Electrochimica Acta, 1998, Vol. 44, pp 1329-1339.

- Pharkya,P., Farhat,Z.,N., Czech,E., Hawthrone,H., Alfantazi,A.,*"Fabrication and characerisation of nanostructured Mechanically alloyed Pt-Co catalyst for oxygen gas-diffusion-electrode,"*, 2003, Proc. Hydrogen and fuel cell, Vancouver, Canada, pp. 205-214.

- Pharkya,P., Farhat,Z.,N., Alfantazi,A., *"Fabrication using high energy ball milling technique and characterisation of Pt-Co electrocatalysts for oxygen reduction in polymer electrolyte fuel cells,"* 2004, First International conference on Fuel cell Development and Deployment,Connecticut, USA, in publication.

- Rhun,V,L., Garnier, E., Pronier,S., Vante, N.A.,*"Electrocatalysis on nanoscale ruthenium-based material manufactured by carbonyl decomposition,"* Electrochemistry communications, 2002, Vol.2, pp 475-479.

- Schulz, R., Lalande, G., Huot J., Boily, S., *"Porous nanocrystalline alloys prepared by high-energy ball milling,"* Materials Science Forum,1998, Vol. 269-272, pp 1055-1060.

- Schulz,R., Huot,J., Liang,G., Boily,S., Lalande,G., Denis,M.,C., Dodelet,J.,P., *"Recent developments in the application of nanocrystalline materials to hydrogen technologies,"* Materials science and Engineering, 1999, Vol 267, pp 240-245.

- Shukla,A.,K., Neergat, M., Bera,P., Jayaram,V., Hedge,M.,S., *"An XPS study on binary and ternary alloys of transition metals with Platinized carbon and its bearing upon oxygen electroreduction in direct methanol fuel cells,"* J. Eelctroanal. Chem., 2001, Vol. 504, pp 111-119.

- Steele,B.,C.,H., *"Material Science and engineering: The enabling technology for the commercialization of fuel cell systems,"* J. of Mat. Science, 2001, Vol. 36, pp 1053-1068.

- Sun,L.,Liu,H., Dou, S., *"The effect of ball milling and rapid quenching on the catalytic activity of the Cu30Al70 alloy,"* Mat. Letters, 1997, Vol.33, pp 79-83.

- Suryanarayana,C., *"Mechanical alloying and Milling,"* Progress in Materials Science, 2001, Vol. 46 (1-2), pp. 1-184.

- Tamizhmani,G.,Dodelet,J.,P.,Guay,D.,Lalande,G.,Capuano,G.,A.,*"Electrocatalytic activity of Nafion-impregnated pyrolyzed cobalt Pththalcyanine,"* J. Electrochem.Soc.,1994,Vol 141 (1), pp 41-45.

- Toda, T., Igarashi,H., Uchida,H., Watanabe,M.,J., *"Enhancement of he electroreduction of oxygen on Pt alloys with Fe, Ni, and Co,"* J. Electrochem. Soc., 1999, Vol. 146 (10), pp 3750-3756.

- Vante,N.,A.,Malakhov.,I.,V.,Nikitenko,S.,G.,Savinova,E.,R.,Kochubey,D.,I., *"In situ probing active centre of Ru chalcogenide electrocatalysts during oxygen reduction using EXAFS spectroscopy,"* J. Physics, 1997, pp C2-887.

- Vlomen,L.,J.,M.,J.,Mugerwa, M., N., *"Fuel Cell Systems,"* 1993, Plenum Press, NY.
- Wang. J., *"Analytical Electrochemistry,"* 1994, VCH Publisher, Inc., NY, USA.
- Wang,W., *"Modeling and simulation of the dynamic process in high energy ball milling of metal powders,"* PhD.,2000, Dept. of Materials and Process Engg., The university of Waikato, New Zealand.
- Watanabe,M., Tsurumi,K., Mizukami,T., Nakamura,T., Stonehart,P., *"Activity and Stability of ordered and disordered Co-Pt alloys for phosphoric acid fuel cells,"* J. Electrochem. Soc., 1994, Vol. 141 (10), pp 2659-2668.
- Wagner,C.,D., *"Handbook of X-ray photoelectron spectroscopy,"* 1979, Perkin-Elmer Coporation, Minnesota.
- Wilson,M.,S., Gottesfeld,S., *"Thin-film catalyst layers for polymer electrolyte fuel cell electrodes,"* J. Appl. Electrochem., 1992, Vol. 22, pp 1-7.
- Wronski,Z.,S., *"Materials for rechargeable batteries and clean hydrogen energy sources,"* International materials Review, 2001, Vol.46 (1), pp 1-49.
- http://scifun.chem.wisc.edu/chemweek/Chelates/Chelates.html
- http://www.jetpul.com/mequip/milloper.htm
- www.aerospaceguide.net
- www.batteryuniversity.com
- www.epsilon-web.net
- www.e-sources.com
- www.fuelcellstore.com
- www.scescape.net/~woods/elements

Appendix A – Cost Analysis

The cost of a single stack dismantable fuel cell is approximately US$132.50 [www.fuelcellstore.com]. This cost may be as high as $300/KW for a more efficient and robust fuel cell, which could potentially find application in buses and other transportation vehicles. While an internal combustion engine requires an investment of $30 to produce one kilowatt (KW) of power, the equivalent cost in a fuel cell is a whopping $3,000 for portable power [www.batteryuniversity.com]. Part of that cost is due to experimental production since the fuel cell is not yet mass-produced. The cost of a Ballard fuel cell bus comes to US$1.4million [www.e-sources.com]. The cost of Apollo space program was $25.4 billion while the cost of Gemini Space program was $1.3 billion [www.aerospaceguide.net]. Table A.1 shows the properties and cost of Pt and C, which are the main, constituents of electrocatalysts layers. The cost and properties of cobalt are also given for the sake of comparison.

Table A.1 *Table showing properties of Pt, Co and C*

Properties/Elements	**Platinum***	**Cobalt***	**Carbon***
Symbol	Pt	Co	C
Colour	Silvery White	Bluish white	Black
Atomic Number	78	27	6
Atomic Weight	195.09	58.9332	12.011
Density @ 293K (g/cm3)	21.45	8.90	~2.62
Melting Point (K)	2045.2K	1768.2	~3823.2
Boiling Point (K)	4443	3373	4470~5070
Electronegativity	2.28	1.88	2.55
Electronic Configuration	[Xe]4f14 5d9 6s1	[Ar] 3d7 4s2	[He]2s2 2p2
Structure	FCC	HCP	Hexagonal layers
Electrical Conductivity (mohm-cm)	94.341	160.256/	0.7272
Cost (US$/100g)	4700	21	2.4

* http://www.scescape.net/~woods/elements

Vulcan XC-72® is different than common carbon because it has better chemical stability in acidic and oxidizing environments even at 150°C. It has high corrosion resistance, electrical conductance, high surface area (250m^2/g) and has low density and low cost [Hooger,G.,2003]

Appendix B - Surface area calculation

Surface areas of the catalysts were calculated using the crystallite size obtained from XRD.

The following formula was used for the surface area calculations [Min, K.,M.,2001];

$$S = 6/\rho_{metal} * d \quad \text{.....B.1}$$

Where, S is the surface area of the particles, ρ_{metal} is the density of metal and d is the diameter of the particle.

Density of the alloy catalyst was calculated using the relative density of the Pt and Co.

All the metals other than Pt and Co, like tungsten, which constituted impurities, were not taken into consideration for the calculation of the relative density.

Density of Pt = 21.45 gm/cm^3 [http://www.scescape.net/~woods/elements]
Density of Co = 8.9 gm/cm^3 [http://www.scescape.net/~woods/elements]

$$\text{Relative density of Alloy (gm/cm}^3\text{)} = \frac{\text{Wt \% Pt} * \rho_{pt} + \text{Wt \% Co} * \rho_{Co}}{\text{Wt\% Pt + Wt\% Co}} \quad \text{.....B.2}$$

Table B.1 *Table showing relative density, crystallite sizes and surface area of the electrocatalysts*

Catalysts	Wt.% Pt	Wt .% Co	Relative Density (gm/cm^3)	Crystallite Size (nm)	Surface area (m^2/gm)
$Pt_{0.25}Co_{0.75}$-40h	22.445	20.295	15.49	36	10.75
$Pt_{0.25}Co_{0.75}$-40-20%C-30min	27.82	25.56	15.44	18.6	20.28
40%PtCo-E-TEK	10.45	12.1	14.71	9	45.3
10%PtCo-E-TEK	0.77	0.53	16.33	7	52.49
PtCo-45-1%C-5h	8.21	48.86	10.70	10	5.6
Lixiviated	15.555	2.025	20.00	7	42.85